Max-Planck-Institut
für Meteorologie

MAX-PLANCK-GESELLSCHAFT

International Max Planck Research School
on Earth System Modelling

The AMOC and its sensitivity to different climate forcings in the range of glacial to modern conditions

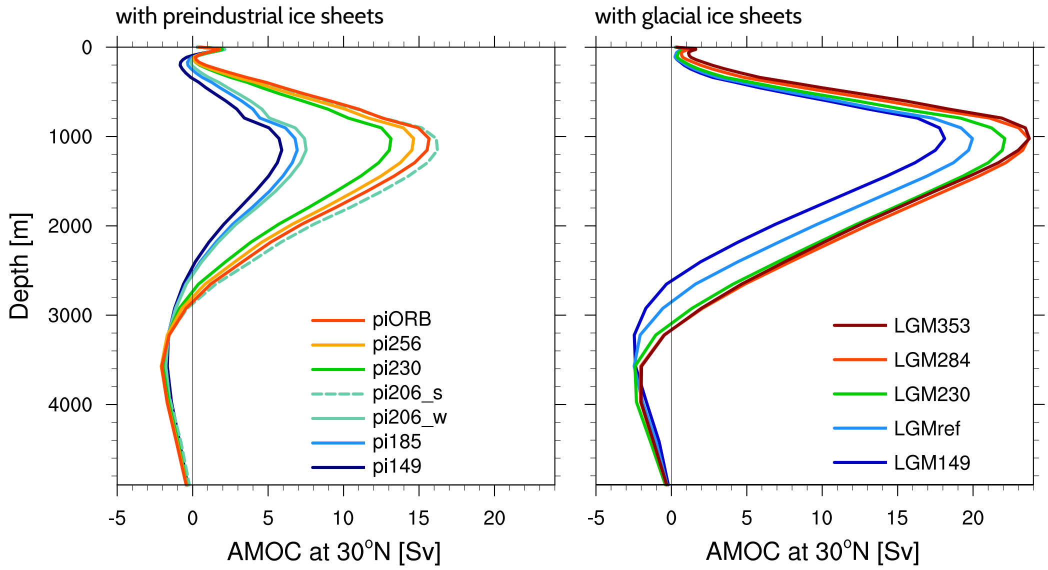

Marlene Klockmann

Hamburg 2017

Berichte zur Erdsystemforschung
Reports on Earth System Science

194
2017

Hinweis

Die Berichte zur Erdsystemforschung werden vom Max-Planck-Institut für Meteorologie in Hamburg in unregelmäßiger Abfolge herausgegeben.

Sie enthalten wissenschaftliche und technische Beiträge, inklusive Dissertationen.

Die Beiträge geben nicht notwendigerweise die Auffassung des Instituts wieder.

Die "Berichte zur Erdsystemforschung" führen die vorherigen Reihen "Reports" und "Examensarbeiten" weiter.

Anschrift / Address

Max-Planck-Institut für Meteorologie
Bundesstrasse 53
20146 Hamburg
Deutschland

Tel./Phone: +49 (0)40 4 11 73 - 0
Fax: +49 (0)40 4 11 73 - 298

name.surname@mpimet.mpg.de
www.mpimet.mpg.de

Notice

The Reports on Earth System Science are published by the Max Planck Institute for Meteorology in Hamburg. They appear in irregular intervals.

They contain scientific and technical contributions, including Ph. D. theses.

The Reports do not necessarily reflect the opinion of the Institute.

The "Reports on Earth System Science" continue the former "Reports" and "Examensarbeiten" of the Max Planck Institute.

Layout

Bettina Diallo and Norbert P. Noreiks
Communication

Copyright

Photos below: ©MPI-M
Photos on the back from left to right:
Christian Klepp, Jochem Marotzke,
Christian Klepp, Clotilde Dubois,
Christian Klepp, Katsumasa Tanaka

The AMOC and its sensitivity to different climate forcings in the range of glacial to modern conditions

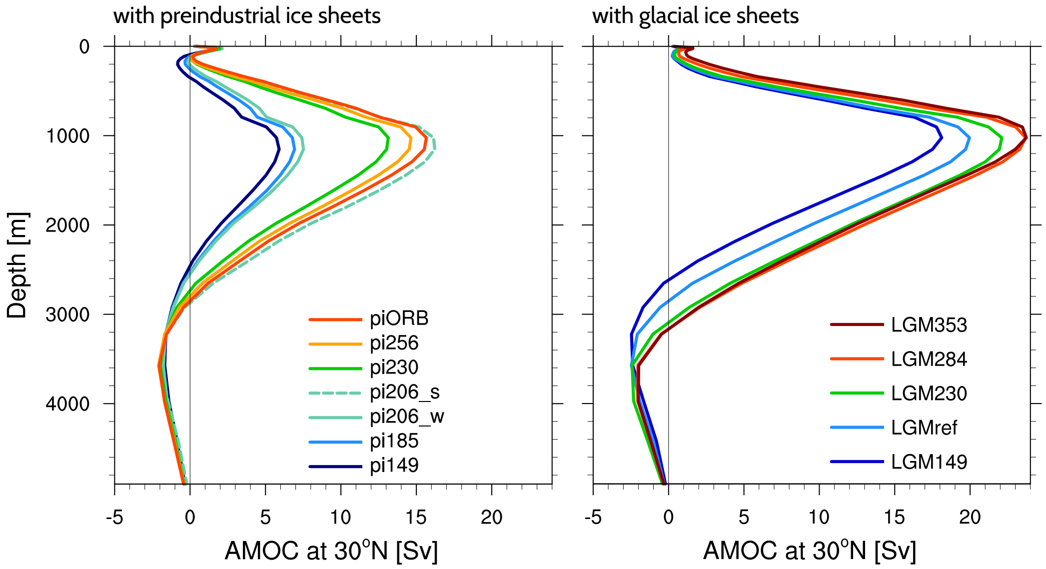

Dissertation with the aim of achieving a doctoral degree
at the Faculty of Mathematics, Informatics and Natural Sciences
Department of Earth Sciences of Universität Hamburg

submitted by

Marlene Klockmann

Hamburg 2017

Marlene Klockmann

Max-Planck-Institut für Meteorologie
Bundesstrasse 53
20146 Hamburg

Tag der Disputation: 12.07.2017

Folgende Gutachter empfehlen die Annahme der Dissertation:

Dr. Uwe Mikolajewicz
Prof. Dr. Johanna Baehr

Berichte zur Erdsystemforschung / Max-Planck-Institut für Meteorologie 194
Reports on Earth System Science / Max Planck Institute for Meteorology 2017

ISSN 1614-1199

Abstract

State-of-the-art coupled climate models produce very different states of the Atlantic Meridional Overturning Circulation (AMOC) in simulations of the Last Glacial Maximum (LGM). In particular, many of them fail to capture the shoaling of the North Atlantic Deep Water (NADW) cell, which is indicated by paleo records. The cause for these differences is not yet well understood. Simulations with the Max Planck Earth System Model (MPI-ESM) are used to improve this understanding by studying the sensitivity of the AMOC and the deep Atlantic water masses to different sets of forcings.

Analysing the individual contributions of the glacial forcings reveals that the glacial ice sheets cause an increase in the overturning strength and a deepening of the NADW cell, while the low greenhouse gas (GHG) concentrations cause a decrease in overturning strength and a shoaling of the NADW cell. The effect of the orbital configuration is negligible. The effects of the ice sheets and the GHG reduction balance each other in the deep ocean so that no shoaling of the NADW cell occurs in the full glacial state.

The mechanism behind the shoaling of the NADW cell is analysed by simulating the AMOC response to different GHG concentrations with linearly decreasing radiative forcing. In order to capture a possible non-linear response, the different GHG concentrations are applied to a setup with glacial ice sheets and to a setup with preindustrial ice sheets. In the simulations with glacial ice sheets, the AMOC decreases linearly with the radiative forcing once the atmospheric pCO_2 is below 284 ppm. To simulate a shoaling relative to the preindustrial AMOC state, GHG concentrations below the glacial level are necessary. Antarctic Bottom Water (AABW) needs to become more saline than NADW to achieve the necessary shoaling. Brine release and shelf convection in the Southern Ocean are key processes for the salinity increase of AABW.

In the simulations with preindustrial ice sheets, the AMOC strength responds non-linearly to the decreasing radiative forcing. There are two distinct AMOC modes: A strong and deep mode at high GHG concentrations, and a weak and shallow mode at low GHG concentrations. The strong AMOC mode becomes unstable at a pCO_2 between 230 ppm and 206 ppm. The weak AMOC mode becomes stable at a pCO_2 between 206 ppm and 185 ppm. In the weak AMOC mode, AABW is as salty as or saltier than NADW, and the Nordic Seas do not contribute to the formation of NADW. In a simulation with 206 ppm, both AMOC modes are unstable and the AMOC oscillates between the two unstable states. These self-sustained oscillations are caused by salinity changes in the tropical and subpolar Atlantic in combination with interactions between the subpolar gyre and deep convection in the Nordic Seas. The AMOC does not switch into the weak mode in the simulations with glacial ice sheets, because the glacial ice sheets increase the AMOC strength by enhancing the density gain in the North Atlantic.

Zusammenfassung

Der Zustand der meridionalen Umwälzzirkulation im Atlantik (englisch: AMOC) während des letzten glazialen Maximums (LGM) wird von verschiedenen gekoppelten Klimamodellen sehr unterschiedlich dargestellt. Rekonstruktionen zufolge war die obere Strömungszelle der AMOC während des LGMs flacher als im heutigen Ozean. Viele Modelle sind nicht in der Lage, dieses Abflachen zu simulieren. Die Gründe für die Widersprüche zwischen Simulationen und Rekonstruktionen sind noch nicht vollständig verstanden. Diese Arbeit untersucht daher wie empfindlich die AMOC im Max-Planck-Institut Erdsystem-Modell auf Antriebs-Änderungen in Form von Treibhausgasen (THG) und Eisschild-Konfigurationen reagiert.

Zunächst wird der glaziale AMOC Zustand in die jeweiligen Beiträge des glazialen Orbits, der kontinentalen Eisschilde und der glazialen THG-Konzentrationen aufgeteilt. Der Beitrag des glazialen Orbits ist vernachlässigbar klein. Die Eisschilde verursachen eine Verstärkung und Vertiefung der oberen AMOC Zelle. Die niedrigen THG-Konzentrationen hingegen verursachen eine Schwächung und Abflachung der oberen Zelle. Die beiden Effekte heben sich teilweise auf, sodass die Tiefe der oberen AMOC Zelle im glazialen Zustand unverändert gegenüber dem heutigen Zustand bleibt.

Simulationen mit verschiedenen THG-Konzentrationen geben Aufschluss über die Prozesse, die ein Abflachen der oberen Zelle bewirken. Um mögliche nicht lineare Effekte zu berücksichtigen, werden zwei Simulationsreihen durchgeführt: eine mit vorgeschriebenen LGM-Eisschilden sowie eine mit prä-industriellen (PI) Eisschilden. Zwischen den einzelnen Simulationen nimmt der Strahlungsantrieb der THG-Konzentrationen in etwa linear ab. In der Simulationsreihe mit LGM-Eisschilden beginnt die AMOC ab einer CO_2-Konzentration von 284 ppm linear mit dem Strahlungsantrieb schwächer zu werden. Um ein Abflachen der oberen Zelle zu simulieren, muss das Antarktische Bodenwasser (AABW) ausreichend schwer und salzig sein, um das Nordatlantische Tiefenwasser (NATW) aus dem tiefen Nordatlantik zu verdrängen. Die Salzanreicherung im AABW wird durch die Freisetzung von Salzlösung während der Meereisbildung im Südlichen Ozean angetrieben. Um ein Abflachen der oberen AMOC Zelle gegenüber des heutigen Zustandes zu simulieren ist eine CO_2-Konzentration von 149 ppm notwendig. Nur dann wird genügend Meereis gebildet um das AABW salzig genug werden zu lassen.

In der Simulationsreihe mit PI-Eisschilden verläuft die Abschwächung der AMOC nicht linear. Es existieren zwei verschiedene AMOC Zustände. Bei hohen CO_2-Konzentrationen ist die obere Zelle stark und tief. Bei niedrigen CO_2-Konzentrationen ist die obere Zelle schwach und flach. Der Übergang zwischen den zwei Zuständen erfolgt abrupt. Der schwache AMOC Zustand tritt auf, wenn AABW salziger wird als NATW und wenn keine Tiefenwasserbildung im europäischen Nordmeer stattfindet. In einer Simulation mit 206 ppm sind beide Zustände instabil und die AMOC springt zwischen den zwei instabilen Zuständen hin und her. Auslöser für diese abrupten Übergänge sind der Salzaustausch zwischen dem tropischen und subpolaren Atlantik sowie die Wechselwirkung zwischen dem subpolaren Wirbel und der Tiefenwasserbildung im europäischen Nordmeer. In den Simulationen mit LGM-Eisschilden wechselt die AMOC nicht in den schwachen Zustand, da die LGM-Eisschilde die AMOC verstärken indem sie den Dichtegewinn im Nordatlantik erhöhen, und die AMOC somit weniger von der Tiefenwasserbildung im europäischen Nordmeer abhängig ist.

Contents

1 | Introduction

The study of past climates can increase the understanding of the climate system, and simulations of past climates additionally give the opportunity to assess the behaviour of numerical models for boundary conditions and forcings which are quite different from present day (e.g., *Hargreaves et al.*, 2013; *Harrison et al.*, 2015). The Last Glacial Maximum (LGM, 21 ky before present) provides a good test case for these kinds of simulations because it represents the most recent time period in which the climate has been very different from today. Therefore, both the proxy availability and the signal-to-noise ratio are relatively high. The climate during the LGM was shaped by a slightly different orbital configuration, very low greenhouse gas (GHG) concentrations and vast continental ice sheets. The Laurentide ice sheet covered Canada and the Canadian Archipelago, and the Fennoscandian ice sheet covered northern Europe and the Barent Shelf. In addition, the glacial forcings - orbit, GHG concentrations and ice sheets - were relatively stable over a few millennia, which makes it possible to study the LGM in equilibrium simulations instead of transient simulations.

The Atlantic Meridional Overturning Circulation (AMOC) plays an important role in the climate system and is a fundamental component of the ocean circulation. The AMOC consists of two overturning cells, which are tightly connected to the two water masses which dominate the Atlantic below 1000 m. The upper overturning cell is associated with North Atlantic Deep Water (NADW); the lower overturning cell is associated with Antarctic Bottom Water (AABW, see also Fig. 1.1 a). The AMOC contributes significantly to the heat transport from the South Atlantic to the North Atlantic and thus influences the climate of the northern hemisphere. At present, the peak northward heat transport at 26°N is approximately 1.25 PW (*McCarthy et al.*, 2015). Future climate projections indicate that a weakening or even a collapse of the AMOC might occur as a consequence of global warming (e.g., *Weaver et al.*, 2012; *Bakker et al.*, 2016). This could lead to large temperature and precipitation changes on the northern hemisphere (e.g., *Vellinga and Wood*, 2002). To understand

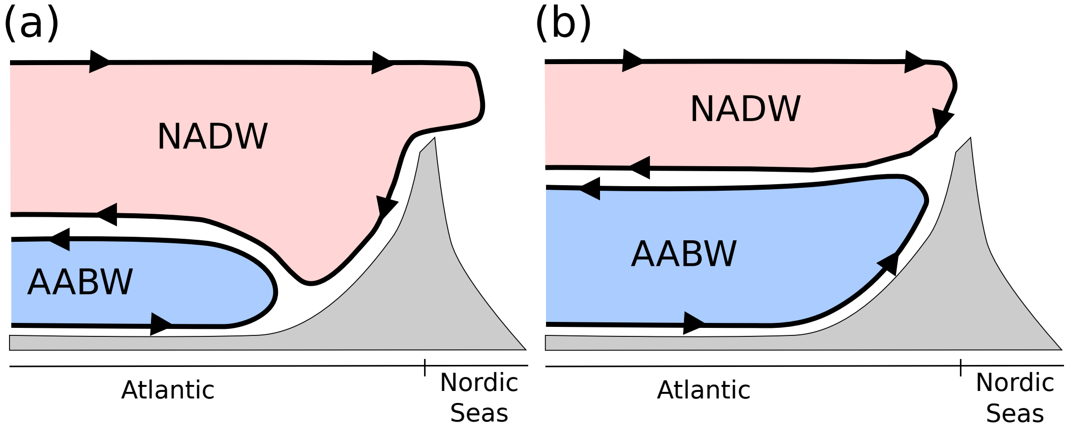

Figure 1.1: Schematic of the AMOC state for **(a)** present day and **(b)** the LGM, redrawn after *Böhm et al.* (2015). The glacial AMOC state corresponds to the cold AMOC mode described by *Böhm et al.* (2015) and *Lippold et al.* (2016). The glacial NADW cell maintained an active export of NADW and it was shallower than its present-day equivalent. The glacial AABW cell reached further into the North Atlantic.

the processes and mechanisms which determine the AMOC response to different boundary conditions and forcings is therefore of particular interest.

Coupled climate models simulate the mean glacial surface climate in reasonable agreement with reconstructions (e.g., *Braconnot et al.*, 2007; *Braconnot and Kageyama*, 2015). However, there is large disagreement between climate models and reconstructions and also between different climate models regarding the state of the glacial AMOC and the state of the glacial deep-ocean water masses. The reason for this disagreement is not yet well understood. The overarching objective of this thesis is therefore to identify and analyse the sensitivity of the AMOC to a broad range of forcings which cover the parameter space between the LGM and the modern climate in a coupled climate model.

1.1 Reconstructions of the glacial AMOC

The water-mass distribution in the Atlantic basin can be reconstructed by measuring the distribution of the ratio of the carbon isotopes ^{13}C and ^{12}C (δ^{13}C). NADW and AABW have distinct δ^{13}C signatures. Water originating in the Southern Ocean typically has very low δ^{13}C values, while North Atlantic water typically has very high values (*Duplessy et al.*, 1988). Reconstructions based on δ^{13}C suggested that the interface between NADW and AABW moved upwards during the LGM in both the eastern (*Duplessy et al.*, 1988) and the western (*Curry and Oppo*, 2005) Atlantic basin; i.e., NADW occupied a shallower layer than today and AABW reached much further into the North Atlantic. Similar inferences can be made from the ratio of cadmium and calcium isotopes (Cd/Ca) or oxygen isotopes (δ^{18}O). A combination of δ^{13}C, Cd/Ca and δ^{18}O measurements in combination with a tracer transport model confirmed that the core of NADW was shifted upwards during the LGM (*Gebbie*, 2014).

The shoaling of the interface between the NADW and AABW inferred from the δ^{13}C measurements was initially interpreted as a weakening and shoaling of the upper overturning cell associated with NADW. This was based on the results of a carbon-cycle model coupled to an ocean model, which could best reproduce the δ^{13}C distribution over most of the Atlantic with a weaker and shallower AMOC (*Winguth et al.*, 1999). Nowadays, there is general agreement that δ^{13}C is a good indicator for the geometry of the overturning but not for strength of the NADW cell (e.g. *Lynch-Stieglitz et al.*, 2007; *Lippold et al.*, 2012). The shallower NADW cell is therefore a well constrained feature of the glacial AMOC, while its strength is more difficult to constrain.

The overturning strength can be reconstructed by the ratio of the radioisotopes protactinium and thorium (^{231}Pa/^{230}Th, hereafter Pa/Th). Protactinium and thorium are radioactive decay products of uranium with very different residence times in the water column. Thorium is removed from the water column within decades, while protactinium can remain dissolved for centuries. An active export of deep water also exports a part of the protactinium from the North Atlantic into the Southern Ocean. As a result the Pa/Th in the sediment of the North Atlantic will be lower than the ratio at which the radioisotopes are produced (*Yu et al.*, 1996). A weak deep-water export would result in a Pa/Th closer to the production ratio. First estimates of the Pa/Th distribution in the Atlantic basin revealed a similar Pa/Th during the Holocene and the LGM, indicating that the glacial export rates of NADW were similar to or slightly higher than today (*Yu et al.*, 1996). Measurements from a high-resolution core at the Bermuda Rise, on the other hand, indicated that the glacial export rates have been 30 to 40 % weaker than today (*McManus et al.*, 2004). The contradictory results can be explained by the uncertainties in the sedimentary Pa/Th record. Apart from the deep-water export rates, the sedimentary Pa/Th depends also e.g., on variations in particle fluxes or scavenging. A variety of possible circulation states could be made consistent with Pa/Th distributions, depending on the assumptions made about particle fluxes and scavenging rates (*Burke et al.*, 2011). Pa/Th measurements in combination with a two-dimensional scavenging model indicated that the glacial export of NADW was at least as strong as today (*Lippold et al.*, 2012).

Combining the Pa/Th with the ratio of neodymium isotopes (^{143}Nd/^{144}Nd, hereafter εNd) can produce a more robust reconstruction of the glacial overturning state. εNd traces the water-mass origin in a sediment core and can therefore identify whether the Pa/Th signature at a given location belongs to water originating from the North Atlantic or the Southern Ocean. The combined measurements revealed that the slightly higher glacial Pa/Th at the Bermuda Rise did not record a weaker export of NADW but rather recorded the sluggish transport of AABW into the North Atlantic (*Böhm et al.*, 2015). Several sediment cores throughout the Atlantic basin confirmed this view of the so-called *glacial cold mode* with a strong and shallow NADW cell and increased AABW presence in the North Atlantic (*Lippold et al.*, 2016, , see also Fig. 1.1 b for a schematic view). Recently, an LGM simulation in a coupled climate model with a data-assimilation scheme confirmed that the glacial cold mode was in best agreement with the available proxy data (*Kurahashi-Nakamura et al.*, 2017). This shallow and active NADW cell is the reference state against which I will compare the glacial AMOC state in simulations with the Max Planck Earth System Model (MPI-ESM).

1.2 Simulations of the glacial AMOC

The climate of the LGM has been extensively studied in the framework of the Paleoclimate Modelling Intercomparison Project (PMIP, e.g., *Crucifix et al.* (2005); *Braconnot et al.* (2011)). The participating coupled climate models produced very different estimates for the glacial AMOC state in the PMIP phases 2 and 3 . In PMIP2, five out of nine models simulated a shallower and weaker NADW cell, while four models simulated a deeper and stronger NADW cell (*Weber et al.*, 2007). This intermodel spread was reduced in PMIP3. Most models simulated a stronger and deeper NADW cell, only one model succeeded in simulating a shallower NADW cell (*Muglia and Schmittner*, 2015). The large inter-model spread in PMIP2 and the incapability of most models to simulate the shoaling of the NADW cell in PMIP3 strongly suggest that there is still a lack of understanding of the mechanisms which determine the glacial AMOC state.

Until today, no controlling factor has been found which could explain the AMOC response in all PMIP2 models. The change in the density difference between NADW and AABW could explain the AMOC response in five out of nine models (*Weber et al.*, 2007). The salinity difference between NADW and AABW was also found to a play a major role. *Otto-Bliesner et al.* (2007) analysed four PMIP2 models, and found that only the models which simulated AABW which was saltier than NADW also simulated a shallower NADW cell. The accuracy of the simulated preindustrial AMOC state was proposed as another possible controlling factor. Models in which the preindustrial NADW cell was too shallow with respect to observations did not simulate further shoaling in the LGM simulations (*Weber et al.*, 2007). *Muglia and Schmittner* (2015) suggested that the wind-stress changes induced by the PMIP3 ice sheets caused the stronger and deeper AMOC in the PMIP3 simulations.

Understanding the individual effects of the glacial orbit, ice sheets and GHG concentrations can help to identify the processes which determine the full glacial AMOC response. Many studies have addressed the effects of the individual glacial forcings on the atmosphere and the *surface* ocean, using either an atmospheric general circulation model coupled to a mixed-layer ocean model (e.g., *Broccoli and Manabe*, 1987; *Hewitt and Mitchell*, 1997; *Felzer et al.*, 1998) or a fully coupled atmosphere-ocean model (e.g., *Shin et al.*, 2003; *Justino et al.*, 2005; *Pausata et al.*, 2011). Addressing the effects of the individual glacial forcings on the AMOC and the *deep* ocean in a coupled model requires computationally expensive simulations because the deep ocean needs a long time to reach an equilibrium state. Therefore only very few studies have analysed the effects of the individual glacial forcings on the AMOC in a coupled model framework. *Kim* (2004) decomposed the glacial forcing into the GHG effect and the combined effect of orbit, ice sheets and possible non-linearities. *Brady et al.* (2013) estimated the GHG effect. Neither of them analysed the effect of all three glacial forcings or addressed the effects on the properties and distribution of NADW and AABW. To identify the processes which determine the full glacial response, however, the effects of all three glacial forcings need to be considered as well as the changes in NADW and AABW. I will therefore identify and analyse the individual effects of the glacial orbit, ice sheets and GHG concentrations on the AMOC and the deep Atlantic water masses in simulations with MPI-ESM in Chapter 3.

Outside the glacial forcing range, the equilibrium response of the AMOC to different GHG concentrations has been studied in more detail. These studies have mostly focused on increasing GHG concentrations with simulations in which the atmospheric CO_2 concentration (pCO_2) was doubled or quadrupled (e.g., *Manabe and*

Stouffer, 1994; *Voss and Mikolajewicz*, 2001b; *Stouffer and Manabe*, 2003; *Li et al.*, 2013; *Rugenstein et al.*, 2016). In all cases the AMOC strength weakened considerably during the first century. In the pCO_2-doubling experiments, the AMOC increased again after the initial weakening. At the end of the simulations, the AMOC strength was either slightly weaker than in the control simulation (*Voss and Mikolajewicz*, 2001b), of similar strength (*Manabe and Stouffer*, 1994) or slightly stronger (*Stouffer and Manabe*, 2003). In the pCO_2-quadrupling experiments, the initial AMOC reduction was larger than in the pCO_2-doubling experiments. In the simulations which were sufficiently long, the AMOC recovered completely (*Stouffer and Manabe*, 2003) or at least partially (*Li et al.*, 2013; *Rugenstein et al.*, 2016) after two to three thousand years. A few studies have also addressed the AMOC response to reduced GHG concentrations. The AMOC strength increased slightly in response to a pCO_2 reduction from 345 ppm to 280 ppm (*Voss and Mikolajewicz*, 2001a), but it almost shut down in response to a pCO_2 reduction from 300 ppm to 150 ppm (*Stouffer and Manabe*, 2003). These different responses suggest that the AMOC response to reduced GHG concentrations is quite non-linear. A similar AMOC response to global cooling was found in a series of simulations with an Earth system Model of Intermediate Complexity (EMIC, (*Wang et al.*, 2002)). In these simulations the cooling was caused by increasing the planetary emissivity instead of reducing the pCO_2. A weak cooling caused an AMOC strengthening, medium cooling caused an AMOC weakening, and strong cooling caused an AMOC shut down. The AMOC response to a GHG reduction at the low pCO_2 end of the parameter space needs to be studied in more detail in order to characterise the non-linear AMOC-pCO_2 relationship in a coupled model. I will therefore analyse the sensitivity of the AMOC to a wide range of GHG concentrations from higher than preindustrial to lower than glacial values in Chapter 4 and Chapter 5.

The previously published studies with changed GHG concentrations mostly used a model setup with modern topography and ice sheets. However, the simulated AMOC response to GHG changes may depend on the prescribed topography and ice sheets. *Zhu et al.* (2015) compared the AMOC response to an abrupt pCO_2-doubling in simulations with modern and glacial ice sheets. In the simulation with modern ice sheets, the AMOC weakened during the first 200 years and remained in a weak state for the remaining 1300 years of the simulation. In the simulation with glacial ice sheets, the AMOC weakened slightly during the first 100 years and then strengthened again over the next 500 years. In the new equilibrium, the AMOC was stronger than in the glacial reference simulation. It is, however, difficult to separate whether the different AMOC response was because of the different ice-sheet configurations or because of the different absolute GHG concentrations in the two simulations. In the simulation with modern ice sheets, the pCO_2 was doubled from 355 ppm to 710 ppm. In the simulation with glacial ice sheets, the pCO_2 was doubled from 185 ppm to 370 ppm. To analyse the effect of the ice sheets on the AMOC sensitivity to different GHG concentrations, I will analyse the AMOC-pCO_2 relationship in a setup with glacial ice sheets (Ch. 4) and in a setup with preindustrial ice sheets (Ch. 5).

Oka et al. (2012) studied the effects of the individual glacial surface fluxes of heat, freshwater and momentum on the state of the glacial AMOC in a stand-alone ocean model. They assessed the response of the AMOC to global cooling by forcing an ocean model with linear combinations of the preindustrial and the glacial heat-flux fields obtained from the PMIP2 simulations with the coupled model MIROC. The cooling was increased step wise by increasing the relative percentage of the glacial heat flux in the forcing field. When a certain threshold in global cooling was crossed, the AMOC switched from a strong state into a weak state. The freshwater forcing only had a minor effect on the location of the cooling threshold. But when the model was forced with glacial wind-stress fields, a much stronger-than-glacial cooling was necessary to cross the cooling threshold than when the model was forced with preindustrial wind-stress fields. *Oka et al.* (2012) suggested that such a cooling threshold could explain the very different glacial AMOC responses in the PMIP ensemble. However, the AMOC in stand-alone ocean models is known to be overly sensitive to forcing changes because of the mixed boundary conditions (*Mikolajewicz and Maier-Reimer*, 1994), and it is unclear if a similar cooling threshold would be found in a coupled climate model (*Marotzke*, 2012). By analysing the AMOC-pCO_2 relationship and comparing it between the two ice-sheet setups in Chapter 4 and Chapter 5, I will also test whether a similar threshold controls the AMOC state in MPI-ESM.

1.3 Multiple AMOC states

The existence of a threshold as described by *Oka et al.* (2012) is closely linked to the existence of multiple AMOC states and their stability. Multiple AMOC states are also an important concept for the understanding of past abrupt climate change which has been documented in the paleo records. Greenland ice-core records revealed large temperature fluctuations during the last two glacial cycles (e.g., *Dans-*

gaard et al., 1984; *Grootes et al.*, 1993). Prominent features were the so-called Dansgaard-Oeschger (DO) events and the Younger Dryas. DO-events describe an abrupt warming over Greenland followed by a gradual cooling period which occurred during the more moderate glacial periods of the last glacial cycles. The Younger Dryas was an abrupt cooling event during the last deglaciation, which lasted for about 800 years. Another important feature of the glacial period are Heinrich events - abrupt cooling events associated with large ice-berg discharge from the Laurentide ice sheet (*Heinrich*, 1988). It is a widely accepted hypothesis that these abrupt temperature changes were linked to abrupt state transitions of the AMOC and variations in deep-water formation in the North Atlantic (e.g., *Broecker et al.*, 1985). Pa/Th records of the last glacial cycle indeed indicated that the AMOC was strong during DO warm periods, weak during the Younger Dryas and weakened or even collapsed during some Heinrich events (*McManus et al.*, 2004; *Böhm et al.*, 2015).

The concept of multiple AMOC states goes back to *Stommel* (1961) who found two stable modes and one unstable mode of the overturning circulation in a two-box model. The different modes arose from the competition of the thermal and the haline forcing (prescribed temperatures vs freshwater fluxes). The first stable mode was dominated by thermal forcing and corresponded to a strong positive flow with sinking in the polar box and rising in the low-latitude box. The second stable mode was dominated by the haline forcing and corresponded to a weaker negative flow. Both modes were stable and coexisted for a certain range of surface freshwater forcing. Similar circulation modes have since then been documented in models of different complexity, ranging from box models (e.g., *Welander*, 1986; *Colin de Verdière*, 2007) and EMICs (e.g., *Ganopolski and Rahmstorf*, 2001) to coupled atmosphere-ocean models (*Manabe and Stouffer*, 1988). Often the reverse haline mode was replaced by an off-mode or a very weak positive circulation mode.

To explain abrupt AMOC-driven climate change, spontaneous transitions or even oscillations between the two AMOC modes need to occur. With constant forcing and in the absence of noise, no oscillations would occur in a box model or an EMIC. Depending on the initial conditions, the system would always equilibrate in either of the two stable states. By adding noise to the forcing, spontaneous transitions or even quasi-periodic oscillations between two *stable* states could be simulated (e.g., *Cessi*, 1994; *Ganopolski and Rahmstorf*, 2002). But, in certain parameter ranges, oscillations could also arise between two *unstable* states without changes in the external forcing (e.g., *Welander*, 1986). *Colin de Verdière* (2007) added convection to a four-box Stommel-type model and found a strong convective overturning branch in addition to the thermal and haline branches from the original Stommel model. In a narrow parameter window, the convective and the thermal branch coexisted in unstable form. In another somewhat broader window, the convective and the haline branch coexisted in unstable form. In these windows, self-sustained oscillations between the two unstable states could occur, which provided an alternative explanation for abrupt AMOC changes on decadal to millennial timescales.

Paleo records suggested that the climate of the Holocene was much more stable than during most of the last two glacial cycles (e.g., *Grootes et al.*, 1993). This raised the question whether the AMOC has shifted from a bistable regime into a monostable regime during the last deglaciation. *Ganopolski and Rahmstorf* (2001) found that the modern climate was insensitive to a periodic weak freshwater forcing, while the same forcing triggered abrupt AMOC transitions under glacial conditions. The stability of the AMOC may, however, be quite model dependent. In a comparison of different EMICs, the present-day AMOC was located in the monostable regime in four of the models and in the bistable regime in the other seven models (*Rahmstorf et al.*, 2005). A similar spread was found among the coupled climate models in the 5th phase of the Coupled Model Intercomparison Project (CMIP5, (*Weaver et al.*, 2012)). The analysis of the AMOC-pCO_2 relationship in Chapter 4 and Chapter 5 also enables me to study, whether multiple AMOC states can exist under certain forcings. I will show that AMOC transitions between two unstable AMOC states can occur under a certain combination of forcings and analyse the underlying mechanism in Chapter 6.

1.4 Thesis objectives

The ultimate goal of this thesis is to analyse the sensitivity of the AMOC to a broad range of forcings which cover the parameter space between the LGM and the modern climate in a coupled climate model and to identify the mechanisms which determine the response of the glacial AMOC. To this end, I present a set of simulations which will allow me to answer the following questions:

1. How do the individual glacial forcings affect the AMOC and the deep Atlantic water masses (Ch. 3)?

2. How does the AMOC respond to different GHG concentrations in the presence of glacial ice sheets and in the presence of preindustrial ice sheets, and which mechanisms drive the response (Ch. 4 and Ch. 5)?

3. Does a similar cooling threshold as described by *Oka et al.* (2012) control the AMOC state in MPI-ESM (Ch. 4 and Ch. 5)?
4. Which processes drive abrupt AMOC transitions in MPI-ESM (Ch. 6)?

The results of the individual chapters are discussed as they are presented in the respective chapters. I discuss the major findings and implications in Ch. 7 and present the overall conclusions in Ch. 8.[1]

---

[1] The chapters 3 and 4 have been published in *Klockmann et al.* (2016) and are reproduced here with minor modifications.

2 | Methods

2.1 Model

I use the physical part of MPI-ESM in the coarse-resolution setup. The model consists of the atmospheric component ECHAM6.1, the land-surface component JSBACH and the ocean component MPIOM. The model version is very similar to the CMIP5 version (*Giorgetta et al.*, 2013). The coarse-resolution setup used here provides the best compromise between computational cost and model accuracy.

ECHAM is an atmospheric general-circulation model with a spectral core. The spectral resolution of the coarse-resolution setup is T31, which corresponds to a horizontal resolution of approximately 3.75° x 3.75° in grid space (see *Stevens et al.*, 2013, for details). There are 31 vertical σ-hybrid layers. JSBACH is embedded into ECHAM. It is run with natural dynamic vegetation (*Reick et al.*, 2013). The accumulation of snow is limited to a maximum snow depth of 10 m water equivalent to prevent excessive snow accumulation at grid points in the vicinity of the prescribed ice sheets. The sum of precipitation and evaporation over the ice sheets is redirected into the surface runoff and reaches the ocean. The river routing is identical for modern and glacial topography. In the glacial case, the rivers have been extended to the nearest coastal grid point of the glacial land-sea mask.

MPIOM is a free-surface primitive-equation ocean model on z-coordinates and a curvilinear grid (*Marsland et al.*, 2003; *Jungclaus et al.*, 2006). In the coarse-resolution setup, the nominal resolution is 3° x 3°. The grid poles are located over Greenland and Antarctica. This configuration produces a minimum grid spacing of 31 km around Greenland and 86 km around Antarctica. The maximum grid spacing is 285 km in the tropical Atlantic and 390 km in the tropical Pacific. There are 40 unevenly spaced vertical levels. The uppermost layer has a thickness of 15 m in order to avoid problems with thick sea ice in the glacial Arctic Ocean. Below the first level, the level thickness increases monotonously from 10 m close to the surface to about

550 m in the deep ocean. The upper 100 m of the water column is represented by nine levels. Partial grid cells fully resolve the bottom topography. The representation of shelf convection and flow over sills is improved by a slope-convection scheme described in *Marsland et al.* (2003). Sea-ice thermodynamics and dynamics are calculated by a Hibler-type sea-ice model with viscous-plastic rheology (see *Marsland et al.*, 2003; *Notz et al.*, 2013, for details)

ECHAM and MPIOM are coupled using the Ocean Atmosphere Sea Ice Soil (OASIS3-MCT, *Valcke* (2013)) coupler. OASIS3-MCT passes sea surface temperature (SST), sea-ice concentration and thickness, snow thickness over sea ice and the surface-ocean currents from MPIOM to ECHAM. Long-wave and short-wave radiation, fluxes of heat and freshwater, surface wind-stress and 10 m-wind speed are passed from ECHAM to MPIOM. The coupling takes place every 24 hours.

The model configuration applied here is the coarse-resolution equivalent of MPI-ESM-P with dynamical vegetation. MPI-ESM-P can be found in the CMIP5 database and participated also in PMIP3. The characteristics of the MPIOM version used in CMIP5/PMIP3 were described by *Jungclaus et al.* (2013) in greater detail.

2.2 Experiments

I perform two reference simulations, a preindustrial control run (hereafter referred to as piCTL) with preindustrial GHG concentrations, modern orbit, land-sea mask, topography and ice sheets and a PMIP3-like LGM run (hereafter referred to as LGM-ref) with glacial GHG concentrations as well as glacial orbit, land-sea mask, topography and ice sheets (see Table 2.2).

The glacial ocean bathymetry and land-sea mask are obtained by adding the anomalies from the ICE-5G reconstructions (0 ka-21 ka, *Peltier* (2004)) to the modern bathymetry. This results in a global mean sea-level drop of approximately 124 m. The continental ice sheets correspond to the PMIP3 boundary conditions (Fig. 2.1, *Abe-Ouchi et al.* (2015)). They are a blended product of the three ice-sheet reconstructions ICE-6G (*Peltier et al.*, 2015; *Argus et al.*, 2014), MOCA (*Tarasov et al.*, 2012) and ANU (*Lambeck et al.*, 2010).

I perform a third reference simulation which has the same configuration as piCTL but with the orbital parameters set to glacial values (see Table 2.1). This simulation will be referred to as piORB. The difference between piORB and piCTL yields the response to the orbital forcing. I will use piCTL as a reference to estimate the total effect of all glacial forcings and piORB whenever I want to ensure that the orbital

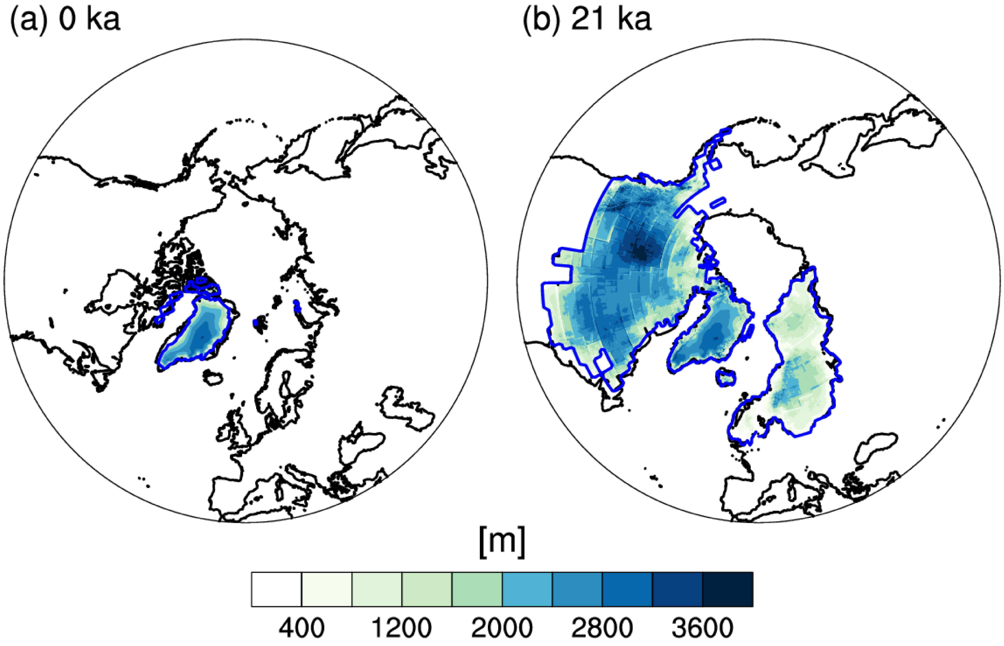

Figure 2.1: High-resolution PMIP3 ice-sheet elevation and coast lines on the northern hemisphere for **(a)** the preindustrial setup at 0 ka and **(b)** the glacial setup at 21 ka. Coast lines are indicated in black, the extent of the ice sheets is indicated in blue.

Table 2.1: Orbital parameters for present day (0 ka) and LGM (21 ka).

Orbit	Eccentricity	Perihelion	Obliquity
0 ka	0.0167724	282.04	23.446
21 ka	0.018994	294.42	22.949

effect is excluded.

To analyse the individual effect of the ice sheets and GHG concentrations, I perform an experiment with glacial orbit and ice sheets but with preindustrial GHG concentrations (LGM284). Comparing LGM284 with piORB gives the response to the combination of the glacial ice sheets, glacial topography and the glacial land-sea mask. In the following, I will simply refer to this combined response as the ice-sheet effect. In contrast to *Kim* (2004) and *Brady et al.* (2013), I estimate the effect of the GHG reduction in the presence of the glacial ice sheets. The GHG effect is given by the difference between LGMref and LGM284.

To analyse the sensitivity of the AMOC to decreasing GHG concentrations, I force MPI-ESM with different GHG concentrations. To assess how the ice-sheet configuration affects the AMOC sensitivity to different GHG concentrations, I perform one set of simulations with prescribed glacial ice sheets and one set with preindustrial ice sheets. Both sets have the glacial orbital configuration to exclude any orbital effects. The GHG concentrations are chosen such that they cover a wide range of the parameter space. The difference in GHG concentrations between the respective simulations is based on the radiative forcing difference (calculated according to *Myhre et al.* (1998)). The difference in radiative forcing between the preindustrial and glacial GHG concentrations is approximately 2.9 $\mathrm{Wm^{-2}}$. The radiative forcing difference between the respective experiments is defined as ΔRF=$\frac{1}{2}(RF_{piCTL}$-$RF_{LGM})$ $\approx$1.45 $\mathrm{Wm^{-2}}$. I change the concentrations of CO_2, N_2O and CH_4 but will in the following refer only to pCO_2 for simplicity.

The simulations with glacial ice sheets are named LGM*xxx*, in analogy to LGM284. The suffix *xxx* stands for the CO_2 concentration in parts per million (ppm). Including LGM284 and LGMref, the LGM*xxx* series consists of five simulations with pCO_2 ranging from 353 ppm to 149 ppm (see lower part of Table 2.2). The simulations with preindustrial ice sheets are named pi*xxx*. Including piORB, the pi*xxx* series consists of six simulations with pCO_2 ranging from 284 ppm to 149 ppm (see upper part of Table 2.2). The pCO_2 range in the pi*xxx* series is smaller than in the LGM*xxx* series because the pi*xxx* series focuses on a non-linear AMOC transition which occurs at low pCO_2. To narrow down the pCO_2 range in which the transition takes place, the radiative forcing difference between the simulations is reduced to $\frac{1}{2}\Delta RF$ $\approx$0.73 $\mathrm{Wm^{-2}}$ in the range of 284 ppm to 185 ppm.

A total of six additional sensitivity experiments are performed to study the importance of brine release in the Southern Ocean, the effect of density fluctuations in the Southern Ocean and the effect of the LGM glacier mask. These experiments are

Table 2.2: List of experiments and the respective forcing configurations. pCO_2 is given in ppm, pN_2O and pCH_4 in ppb. The length of the simulations is given in years.

Experiment	Orbit	Ice sheets	$pCO_2/pN_2O/pCH_4$	Length
piCTL	0 ka	0 ka	284/791/275	1700
piORB	21 ka	0 ka	284/791/275	3900
pi256	21 ka	0 ka	256/664/255	5700
pi230	21 ka	0 ka	230/548/236	11450
pi206	21 ka	0 ka	206/444/218	12350
pi185	21 ka	0 ka	185/350/200	4000
pi149	21 ka	0 ka	149/196/162	4000
LGM353	21 ka	21 ka	353/1078/318	1400
LGM284	21 ka	21 ka	284/791/275	2000
LGM230	21 ka	21 ka	230/548/236	1400
LGMref	21 ka	21 ka	185/350/200	2300
LGM149	21 ka	21 ka	149/196/162	2800

listed in Table 2.3 and will be introduced in detail in their respective sections.

All experiments are integrated for at least 1400 years to reach a quasi-equilibrium. This approach is justified because the forcing at the LGM was relatively stationary over a few millennia. The ocean in the control simulations piCTL, piORB and LGMref was started from a preindustrial and glacial state, respectively, which were obtained from simulations with earlier versions of MPI-ESM. To shorten the spin-up period of the respective pi*xxx* and LGM*xxx* simulations, the three-dimensional ocean temperature field was adjusted by a best-guess estimate at the beginning of each simulation. In the following, I analyse averages of the last 300 years of the respective simulations if not stated otherwise.

Table 2.3: List of sensitivity experiments and the respective forcing configurations. The modifications with respect to the reference simulation are listed in the third column. All other forcings are identical to the reference simulations. The length of the simulations is given in years.

Experiment	Reference	Modifications	Length	Chapter
piORB_brine	piORB	$S_{seaice,SO}$=20 g kg^{-1}	2200	Ch. 4.5
pi185_brine	pi185	$S_{seaice,SO}$=20 g kg^{-1}	3600	Ch. 5.4
pi206_rest	pi206	T and S restoring in the South Atlantic	4000	Ch. 6.2
LGM284_glac	LGM284	preindustrial glacier mask	3000	Ch. 7.1.1
LGMref_brine	LGMref	$S_{seaice,SO}$=20 g kg^{-1}	1400	Ch. 4.5
LGM149_brine	LGM149	$S_{seaice,SO}$=20 g kg^{-1}	1800	Ch. 4.5

3 | The combined and individual effects of the glacial forcings

Before the glacial AMOC response can be decomposed into the respective contributions of the orbit, the ice sheets and the low GHG concentrations, it is necessary to give an overview of the response of the climate system to the total glacial forcing. The first part of this chapter describes the response of the surface climate, the changes of the water masses in the deep Atlantic and the associated AMOC response. To evaluate how well MPI-ESM is simulating the overturning, I discuss not only the AMOC response but also the simulated preindustrial AMOC state. I further compare the results with reconstructions and previous results from PMIP2, PMIP3 and other simulations where applicable. The second part of this chapter then addresses the effect of the individual glacial forcings. The analysis follows the same structure as in the first part, beginning with the surface response and concluding with the deep water masses and the overturning.

3.1 The control and glacial climates

3.1.1 Surface climate

Surface air temperature

The simulated global-mean surface air temperature in LGMref cools by 5.18 K with respect to piCTL. The most recent estimate of the global-mean cooling based on reconstructions is 4.0 ± 0.8 K (*Annan and Hargreaves*, 2013; *Shakun et al.*, 2012). In PMIP2, the global-mean cooling ranged from 3.6 to 5.7 K (*Braconnot et al.*, 2007) and five PMIP3 models evaluated by *Braconnot and Kageyama* (2015) simulated a global-mean cooling ranging from 4.41 to 5 K. Hence, the simulated estimate in LGMref appears reasonable, being slightly colder than the reconstructions and well within the range of previous simulations.

The strongest cooling in the LGMref simulation takes place over the ice sheets in response to the ice-sheet elevation and albedo (Fig. 3.1 a). Cooling over the ice-free continents ranges from 3 to 8 K. A weak warming can be seen over the North Atlantic and over the Gulf of Alaska. The warming over the North Atlantic is an imprint of underlying warm SSTs (see Sect. 3.1.1), the warming over the Gulf of Alaska is generally explained by atmospheric circulation changes due to the Laurentide ice sheet (see e.g., *Justino et al.* (2005), *Otto-Bliesner et al.* (2006) and Sect. 3.2).

The simulated latitudinal cooling pattern agrees well with reconstructions between 60°S and 60°N, as a comparison of simulated and reconstructed surface air temperature differences over land at the proxy sites shows (Fig. 3.2 a). The reconstructions are taken from *Bartlein et al.* (2011) and *Shakun et al.* (2012). The simulated temperatures are height corrected to account for discrepancies between the coarse model topography and the actual high-resolution PMIP3 topography. Still, the model overestimates cooling over Antarctica and in the vicinity of the ice sheets north of 60°N. These areas are characterised by large height gradients, which may be resolved neither by the coarse model grid nor the higher-resolution PMIP3 topography. This issue was recognised as *representativeness error* by *Hargreaves et al.* (2013). In addition, the surface temperature over the ice sheets cannot exceed 0°C within the model which may induce additional cooling directly over and downstream of the ice sheets. This may explain in part why the simulated global-mean estimate of the surface cooling in LGMref is slightly stronger than the reconstructed estimate of *Annan and Hargreaves* (2013).

Sea surface temperature

The simulated global-mean SST in LGMref cools by 2.61 K with respect to piCTL. This fits within the range of the MARGO reconstructions which indicate a cooling of 1.9 ± 1.8 K (*MARGO Project Members*, 2009). It is also similar to previous results from *Brady et al.* (2013), who simulated a ΔSST of 2.4 K with CCSM4.

The tropical ocean cools by 1.6 to 2.6 K (Fig. 3.3 a), which is also in good agreement with the MARGO estimate of 1.7 ± 1 K and the range of the PMIP2 ensemble of 1 to 2.4 K in the tropics (*Otto-Bliesner et al.*, 2009). The cooling increases towards subpolar latitudes where it exceeds 4 K in the Labrador Sea, the Nordic Seas, in the North Pacific and over the Antarctic Circumpolar Current. The Arctic Ocean does not show any significant cooling as the Arctic surface waters are already close to the freezing point in piCTL. The surface ocean around Antarctica cools by 0.4 to

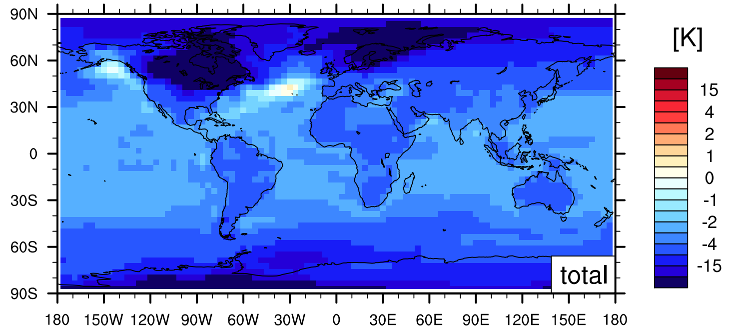

(a) ΔT_{2m} (LGMref – piCTL)

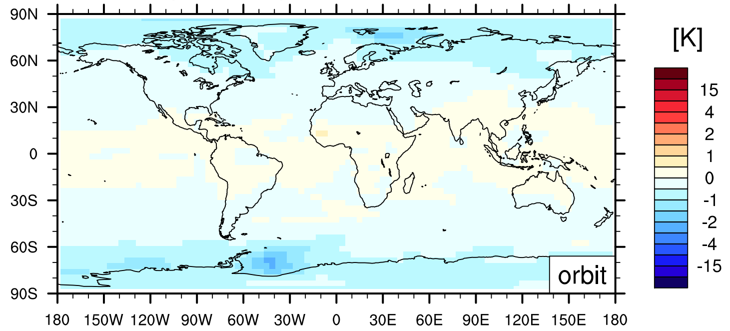

(b) ΔT_{2m} (piORB – piCTL)

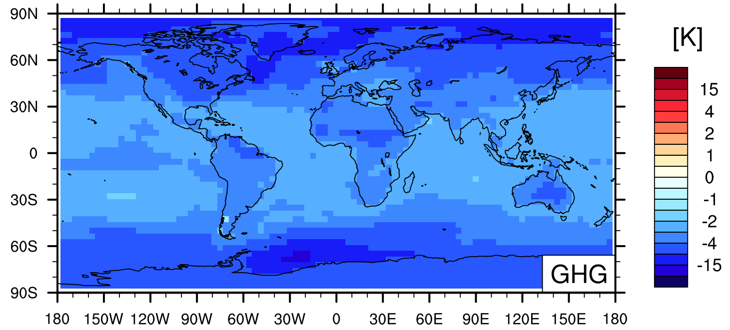

(c) ΔT_{2m} (LGMref – LGM284)

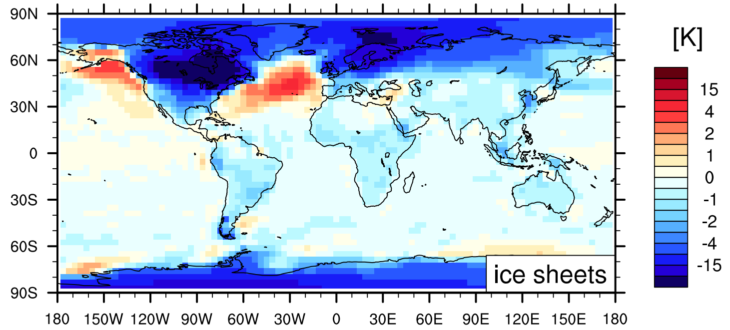

(d) ΔT_{2m} (LGM284 – piORB)

Figure 3.1: 2m air-temperature differences in response to **(a)** the total glacial forcing (LGMref – piCTL), **(b)** the orbital configuration (piORB – piCTL), **(c)** the glacial GHG concentrations (LGMref – LGM284) and **(d)** the ice sheets (LGM284 – piORB).

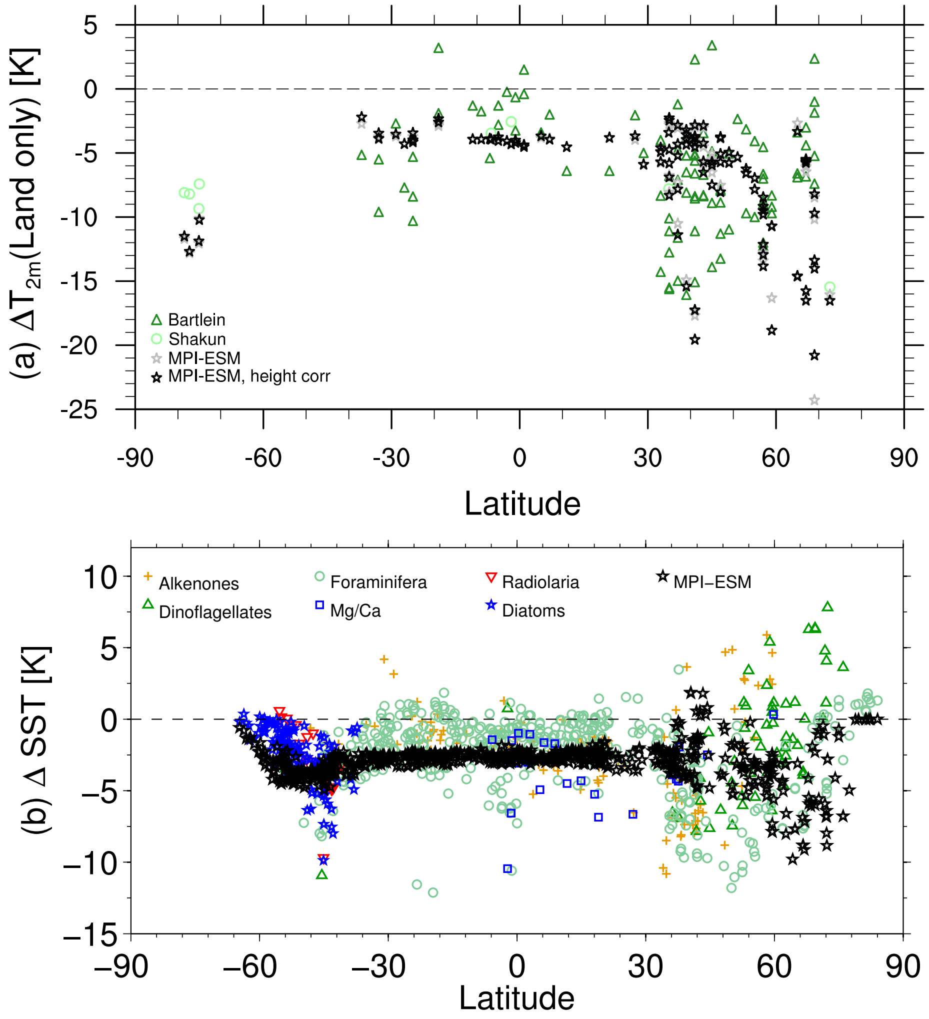

Figure 3.2: Comparison of the temperature differences within the model to reconstructed temperature differences at the proxy sites (LGMref – piCTL). **(a)** Land based temperature differences from *Bartlein et al.* (2011) (dark-green triangles), additional points from the compilation by *Shakun et al.* (2012) provided in the online supporting material of *Schmittner et al.* (2011) (light-green circles) and simulated surface temperature differences (without height correction: grey stars, with height correction: black stars). **(b)** SST differences from MARGO (coloured symbols) and simulated SST differences (black stars).

0.8 K. The central North Atlantic warms by 1.6 to 2.6 K. This warming is caused by a shift of the subtropical gyre (STG) and the subpolar gyre (SPG) (Fig. 3.4 a), which enhances the transport of warm subtropical water to the North Atlantic.

Comparing the simulated SST differences with the MARGO reconstructions at the proxy sites as a function of latitude (Fig. 3.2 b), shows that the model is always within the range of the reconstructions but generally colder than the proxy mean cooling. From 70°S to 30°N both model and proxies show a relatively small scatter, and the latitudinal pattern of cooling is quite similar. North of 30°N, the scatter of both model and proxies increases, and there is very little agreement between the two. Although the North Atlantic and Nordic Seas are the most densely sampled areas, it remains very difficult to constrain the temperature anomaly in this region due to divergent proxy results (*MARGO Project Members*, 2009). In fact, the simulated SST differences agree quite well with the reconstructions based on foraminifera, but there is little agreement with reconstructions based on dinoflagellates and alkenones.

Sea surface salinity

The lower glacial sea level leads to a global-mean salinity increase of about 1.21 g kg^{-1}. This corresponds to the increase seen over most of the tropical ocean, where salinity increases by 0.5 to 1.5 g kg^{-1} (Fig. 3.3 c). Larger increases can be seen on the shelves of the Weddell Sea, Baffin Bay and Beaufort Sea. In the Mediterranean the salinity increase exceeds 5 g kg^{-1} due to the reduced exchange with the Atlantic (*Mikolajewicz*, 2011). The eastern North Atlantic shows a salinity increase of about 2.5 g kg^{-1} which can also be attributed to the shift in the STG-SPG system (Fig. 3.4 a). Freshening occurs in areas where runoff from the Laurentide and Fennoscandian ice sheets reaches the ocean.

3.1.2 Deep water masses in the Atlantic

A section of temperature differences between LGMref and piCTL through the Atlantic from the Southern Ocean to the Nordic Seas shows that cooling occurs over the entire water column (Fig. 3.5 b). The cooling is strongest at about 2500 m depth, right above the boundary between NADW and AABW in piCTL. The water-mass boundary is inferred from the location of the strongest vertical gradient in both temperature and salinity (Fig. 3.5 a and e). There is, however, no clear indication of an upward shift of the water-mass boundary in LGMref.

Also the salinity anomalies do not indicate an upwards shift of the water-mass

(a) ΔSST (LGMref − piCTL)

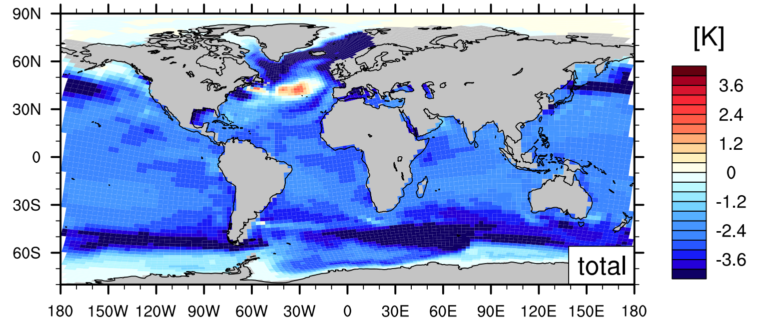

(b) ΔSST (LGM284 − piORB)

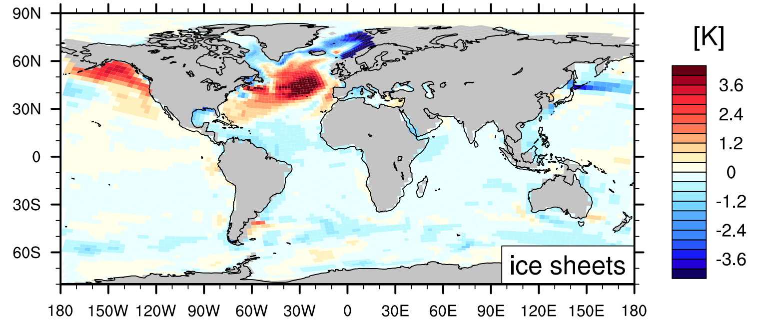

(c) ΔSSS (LGMref − piCTL)

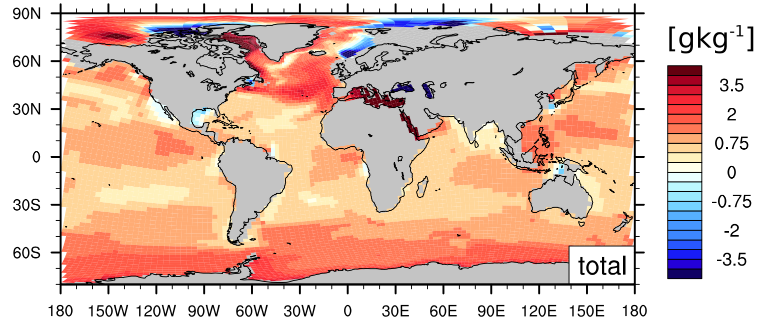

(d) ΔSSS (LGM284 − piORB)

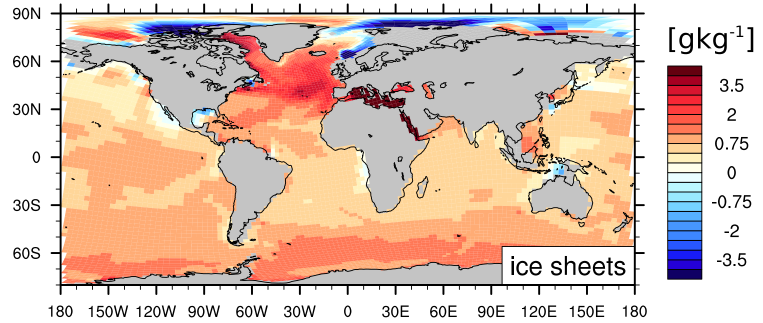

Figure 3.3: **(a)** SST response to the total glacial forcing (LGMref – piCTL) **(b)** SST response to the ice sheets (LGM284 – piORB), **(c)** SSS response to the combined glacial forcings (LGMref – piCTL) and **(d)** SSS response to the ice sheets (LGM284 – piORB).

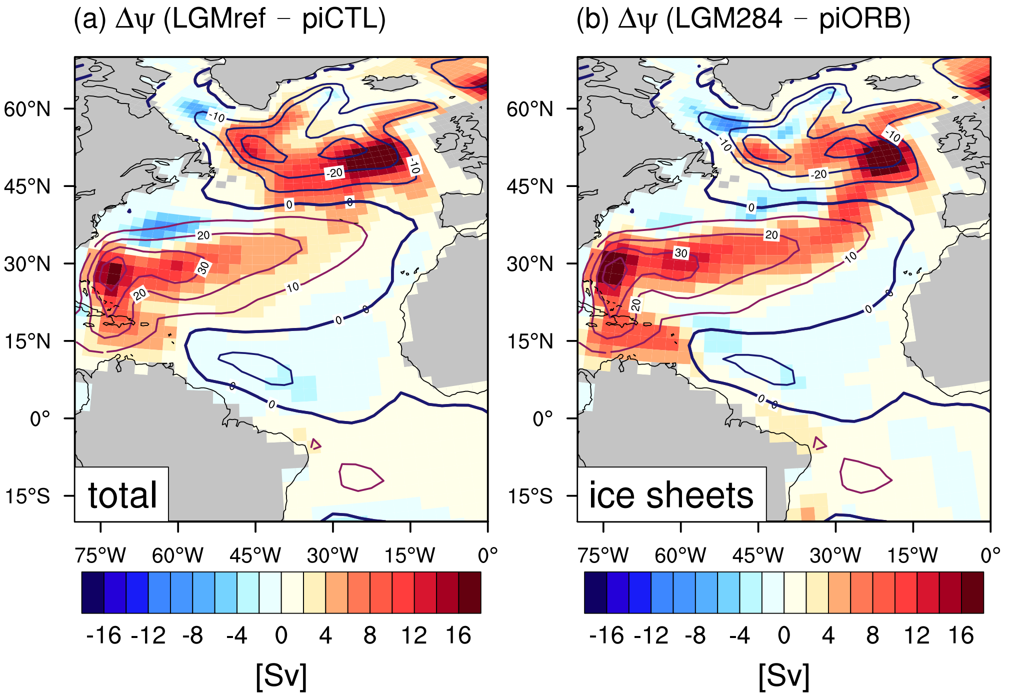

Figure 3.4: Changes in the barotropic stream function induced by **(a)** the total glacial forcing (LGMref – piCTL) and **(b)** the ice sheets (LGM284 – piORB). Superimposed contours show the absolute barotropic stream function in the respective reference experiment, i.e., piCTL in (a) and piORB in (b). Cyclonic rotation is indicated by blue contours, anti-cyclonic rotation by red contours.

boundary (Fig. 3.5 f). Instead, they show that the salinity difference between AABW and NADW decreases. The salinity increase is strongest in the deep Weddell Sea. Here, the salinity increase is on the order of 0.3 g kg^{-1} above the global-mean increase. In contrast, the salinity increase of NADW is smaller than the global mean increase. Because the salinity increase of AABW is larger than that of NADW, the north-south salinity difference in the deep Atlantic is reduced by a factor of three to 0.1 g kg^{-1}. The simulated salinity increase of AABW is weaker than suggested by reconstructions. *Adkins et al.* (2002) found that the north-south salinity gradient in the deep glacial Atlantic was reversed with respect to modern conditions, with AABW being saltier than NADW. They found that glacial AABW was about 2.4 ± 0.17 g kg^{-1} saltier than the modern AABW. The simulated salinity difference between LGMref and piCTL in the Weddell Sea is about 1.5 g kg^{-1}. Therefore, the simulated glacial AABW is not salty enough to produce a north-south salinity gradient of the correct sign and magnitude. This is a problem that many coupled LGM simulations have in common: out of the nine models that participated in PMIP2, only one succeeded in producing a salinity increase in the deep Southern Ocean of a comparable magnitude (*Weber et al.*, 2007), and only two were able to simulate the reversal of the north-south salinity gradient (*Otto-Bliesner et al.*, 2007).

3.1.3 Overturning

The simulated preindustrial AMOC has a maximum overturning strength of 16.5 Sv (Fig. 3.6 a). This maximum occurs at 30°N. The northward transport of AABW has a maximum of 4 Sv near 15°N. Latest results from the RAPID-MOCHA array at 26°N reveal a mean AMOC strength of 17.2 ± 0.9 Sv (*McCarthy et al.*, 2015). Estimates of northward AABW transport are within the range of 1.9 to 4 Sv (*Frajka-Williams et al.*, 2011). Therefore, the simulated strength of the two cells lies well within the uncertainty range of the observations.

The NADW cell extends down to about 2900 m in piCTL. The boundary between the two overturning cells is quite flat, having the same depth at all latitudes. Thus, the model produces a too shallow NADW cell north of 26°N compared with a depth of 4300 m at 26°N in the RAPID-MOCHA observations (*Msadek et al.*, 2013). A too shallow NADW cell has also been reported for many of the preindustrial simulations in PMIP2 (*Weber et al.*, 2007) and newer simulations (e.g., *Msadek et al.*, 2013; *Brady et al.*, 2013, for CCSM4).

The simulated glacial AMOC of 20 Sv exceeds the preindustrial AMOC (Fig. 3.6 b). The depth of the NADW cell remains unchanged, as does the strength of the AABW

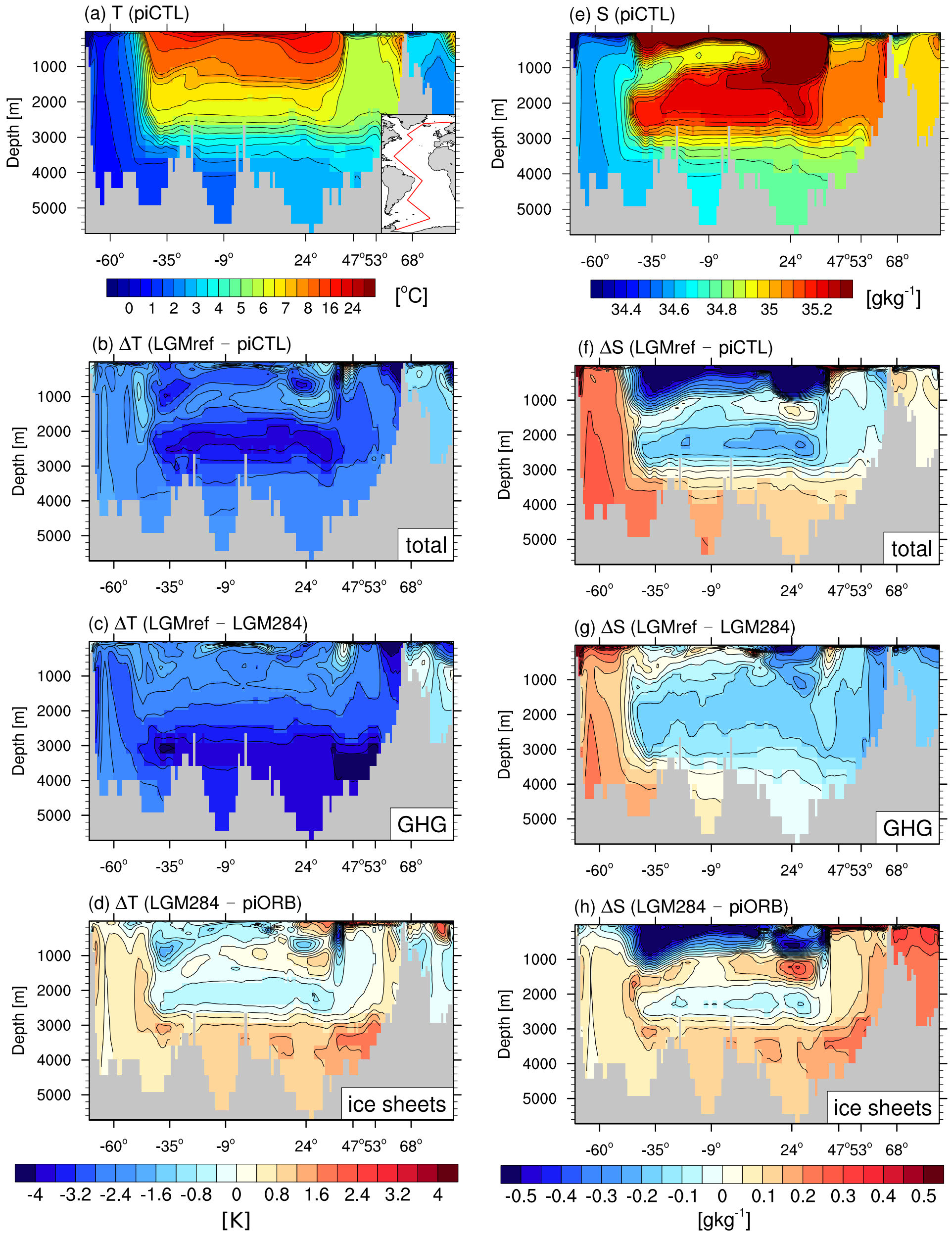

Figure 3.5: Transect through the Atlantic. **(a-d)** From top to bottom: potential temperature in piCTL and temperature changes due to the total glacial forcing (LGMref – piCTL), the glacial GHG concentrations (LGMref – LGM284) and the ice sheets (LGM284 – piORB). **(e-h)** As left column but for salinity. Before calculating the differences, the salinity of piCTL and piORB has been increased by 1.21 $\mathrm{g\,kg^{-1}}$ for comparison with the GHG induced differences (LGMref – LGM284). A map of the transect is shown in (a).

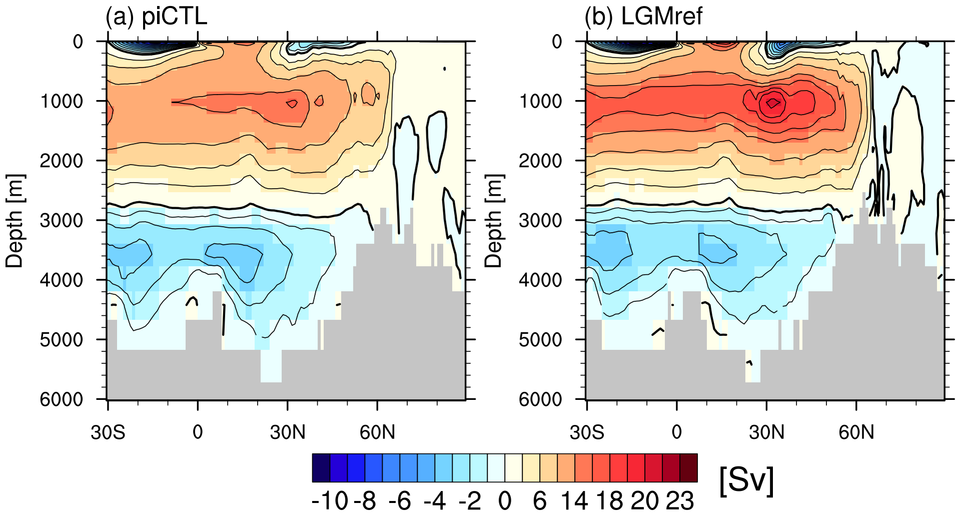

Figure 3.6: Atlantic meridional overturning stream function for **(a)** the preindustrial state and **(b)** the glacial state. Red shading indicates clockwise, blue shading anticlockwise flow. Note that the contour levels are not symmetric.

cell. This response is quite common for models that have participated in PMIP3. All models simulate a stronger AMOC and all models but one simulate either a deepening or no change of the NADW cell depth (*Muglia and Schmittner*, 2015).

The relationship between the geometry of the two overturning cells and the actual vertical distribution of NADW and AABW is not necessarily straightforward. The temperature and salinity sections in piCTL (Fig. 3.5 a and e) show that a significant amount of NADW reaches levels below 3000 m, even though this is not depicted by the zonally-integrated overturning stream function (Fig. 3.6 a). Hence, changes in the relationship between NADW and AABW inferred only from the overturning stream function need to be interpreted with great care. In the LGMref simulation, however, the responses of hydrography and overturning stream function appear consistent; neither of them indicate a change in the vertical extent of NADW.

3.2 Effect of individual glacial forcings

3.2.1 Surface climate

Surface temperature

The orbital configuration has the smallest effect on the annual average surface temperature distribution, a finding which is in agreement with previous studies (e.g., *Hewitt and Mitchell*, 1997). The tropical-temperature change is mostly smaller than ± 0.5 K (Fig. 3.1 b). The cooling is stronger at high latitudes with 1 to 2 K. The strongest cooling is located over the Weddell Sea and the Barents Sea. In these regions, the temperature change is amplified by an expansion of the sea ice and the subsequent reduction of oceanic heat loss to the atmosphere. Because the orbital effect on the mean climate is very small, I will in the following focus only on the effects of GHG reduction and ice sheets.

The effect of the GHG reduction shows the typical pattern of a GHG reduction experiment, with polar amplification and stronger cooling over the continents than over the ocean (Fig. 3.1 c). Also here, the strongest cooling takes place over the Weddell Sea due to the expansion of the winter sea ice. The GHG reduction accounts for most of the cooling over the ocean in the total response.

The ice sheets induce stronger cooling over the continents than over the ocean (Fig. 3.1 d). The cooling is strongest directly over the Laurentide, Fennoscandian and West Antarctic ice sheets, from the combined effect of albedo, elevation and glacier mask. The warming over the North Pacific and North Atlantic seen in the total glacial response can be attributed to the effect of the ice sheets: There is a strong warming over the North Pacific and North Atlantic, which is also present in the SST pattern (see Fig. 3.3 b). These warmer patches are most likely caused by circulation changes of both ocean and atmosphere. The North Pacific warming was also found in earlier modelling studies in response to both the ICE-4G (*Justino et al.*, 2005; *Kim*, 2004) and the ICE-5G reconstruction (*Otto-Bliesner et al.*, 2006). *Justino et al.* (2005) connected the warming to topographic blocking upstream of the Laurentide ice sheet. The warming in the North Atlantic is caused by a shift in the STG-SPG system in response to wind-stress changes due to the ice sheets. In LGM284, the STG extends further north than in piORB (Fig. 3.4 b). The maximum warming collocates with the northward extension of the STG. Because the STG-SPG system is strongly controlled by the surface wind-stress forcing, this warming pattern is very sensitive to the prescribed ice sheets. The warming did not occur in simulations using the ICE-4G ice sheets (*Justino et al.*, 2005; *Kim*, 2004) but it was present in simulations using the ICE-5G ice sheets (*Pausata et al.*, 2011). *Ziemen et al.* (2014) found that different ice-sheet configurations had a large impact on deep-water formation patterns in the North Atlantic and thus also on regional heat budgets and surface temperatures.

Surface salinity

The GHG reduction causes a salinity increase in high latitudes and a freshening in the entire North Atlantic and the subtropical latitudes of the Southern Hemisphere (not shown). This pattern corresponds to a weaker water cycle in cold climates. It also agrees well with the GHG effect on surface salinity found by *Kim* (2004). The salinity increase in the high-latitude Southern Ocean favours the formation of AABW.

The ice-sheet effect dominates the total surface salinity response (see Fig. 3.3 c and d). The freshening in the high northern latitudes occurs due to precipitation changes in the vicinity of the ice sheets. The strong salinity increase in the eastern North Atlantic is caused by a combination of effects: In piORB, the relatively fresh SPG extends very far eastwards (see contours in Fig. 3.4 b). This causes the upper 200 m of the water column in the eastern North Atlantic to be much fresher than the underlying water. In LGM284, the SPG retreats westwards and the STG extends further north (Fig. 3.4 b), enhancing the surface salinity in the eastern North Atlantic. In addition, the wind-stress anomaly due to the ice sheets (Supp.Fig. B.2 c) induces an offshore Ekman transport and upwelling off the Bay of Biscay and the Irish coast. This upwelling brings the saltier water from deeper layers to the surface, thus enhancing surface salinity further. *Kim* (2004) did not find this salinity increase in the North Atlantic in response to the ice sheets. Instead, he found that the ice sheets induced a substantial freshening in the North Atlantic (see his ICEAN effect). The salinity of the North Atlantic is an important factor for the formation of NADW; a salinity increase favours NADW formation while a salinity decrease counteracts it. Hence, the surface salinity response has a direct impact on the deep water masses and the overturning, as the next sections will show.

3.2.2 Deep water masses in the Atlantic

The ice sheets induce a warming throughout the Atlantic below 3000 m, which increases towards the north (Fig. 3.5 d). This warming indicates a larger percentage of relatively warm NADW below 3000 m and a corresponding reduction of cold AABW. Between 1500 and 2500 m, there is a cooling associated with a weaker Mediterranean Outflow and increased convection in the Labrador Sea. In piCTL, there is a strong vertical temperature gradient centred around 3000 m, indicating the boundary between AABW and NADW. In LGM284, this gradient is weakened by a factor of two due to the larger percentage of NADW present below 3000 m. The salinity anomalies (Fig. 3.5 h) are similar to the temperature anomalies. There is a freshening above 2500 m in response to the reduced Mediterranean outflow. The strong salinity increase in the North Atlantic below 3000 m north of 47°N also indicates the increased fraction of NADW, which agrees well with the surface salinity increase in the North Atlantic.

The GHG reduction causes a cooling of the entire water column (Fig. 3.5 c). The cooling is strongest north of 30°N below 3000 m, indicating a larger percentage of cold AABW and a smaller percentage of NADW below 3000 m. The density difference between the two water masses increases due to salinity changes; NADW becomes fresher and AABW saltier (Fig. 3.5 g). The strongest salinity increase takes place in the Weddell Sea both at the surface close to the coast and in the deep Weddell Sea. This increase is caused by changes in the haline density flux due to enhanced sea-ice formation and increased brine release (more details in Ch. 4.4 and 4.5).

The decreased fraction of NADW below 3000 m in response to the GHG reduction is similar to the response suggested by the reconstructions based on $\delta^{13}C$ (*Duplessy et al.*, 1988; *Curry and Oppo*, 2005). However, the effect of the GHG reduction and that of the ice sheets compensate for each other in the deep Atlantic, so that no clear indication of a shoaling of the water mass boundary can be observed in the LGMref simulation.

3.2.3 Overturning

The presence of the glacial ice sheets causes the strength of the NADW cell to increase by 8 Sv at 30°N (compare orange and black solid lines in Fig. 4.1). The boundary between the two cells (indicated by the level of zero transport) is shifted downwards by about 300 m. This reflects the increased NADW formation due to the increased northward salt transport (Fig. 3.3 d) and is consistent with the increased fraction of NADW below 3000 m seen in the hydrographic sections (Fig. 3.5 d and h).

The GHG reduction induces a decrease in the NADW cell strength by 4 Sv and a shoaling of the NADW cell by about 300 m (compare orange and cyan lines in

Fig. 4.1). Again, the overturning response is in agreement with the response of the deep water masses. The GHG-induced shoaling of the NADW cell is exactly compensated for by the ice-sheet-induced deepening.

While the ice-sheet effect described in previous studies varies both in sign and magnitude, the GHG effect appears to be more consistent across the different studies, at least in its sign. The ice-sheet effect depends on the ice-sheet reconstruction and also on the model. The ICE-4G ice sheets induced a weakening of the NADW cell and an expansion of the AABW cell (*Kim*, 2004). The PMIP3 ice sheets induced a strengthening and shoaling of the NADW cell in CCSM4 (compare experiments LGM and LGMCO$_2$ in *Brady et al.*, 2013). In a recent study, *Muglia and Schmittner* (2015) found that applying glacial wind stress anomalies from the PMIP3 ensemble in the UVic model led to an increased northward salt transport, enhanced overturning and a deeper NADW cell, which is consistent with the ice-sheet effect in MPI-ESM. The sign of the GHG effect appears more consistent. Both *Kim* (2004) and *Brady et al.* (2013) find a shoaling and weakening of the NADW cell as well as an enhanced AABW cell in response to the GHG reduction, which is consistent with the GHG effect in MPI-ESM.

In the following chapters, I will explore the sensitivity of the AMOC to different GHG concentrations in one setup with glacial ice sheets and in another setup with preindustrial ice sheets. These simulations will give insight into the processes which determine the geometry and strength of the overturning. The two setups with the different ice-sheet configurations will also provide a larger set of estimates of the ice-sheet effect and the GHG effect. Thus, the robustness of the two effects under different background climates can be tested.

3.3 Conclusions

Based on the simulations piCTL, piORB, LGMref and LGM284, I conclude the following:

- The simulated glacial AMOC in MPI-ESM is stronger than the preindustrial AMOC and no shoaling of the NADW cell occurs. The latter is at odds with reconstructions.

- The glacial orbital configuration has only a small effect on the mean surface climate and a negligible effect on the overturning state.

- The PMIP3 ice sheets induce a deepening of the NADW cell and an increase in the overturning strength caused by wind-stress changes which favour NADW formation.

- The GHG reduction induces a shoaling of the NADW cell and a decrease in the overturning strength. This is caused by changes in the salinity of NADW and AABW. NADW becomes fresher and lighter; AABW becomes saltier and denser.

- The ice-sheet effect and the GHG effect compensate for one another in the deep ocean, so that no shoaling of the boundary between NADW and AABW is simulated in the glacial reference simulation LGMref.

4 | Effect of different GHG concentrations in the glacial setup

This chapter discusses the effect of different GHG concentrations on the AMOC and the deep Atlantic water masses in the setup with the glacial ice sheets. As described in Ch. 2, the radiative forcing between the respective simulations decreases approximately linearly. The analyses will always start with the highest pCO_2 and then discuss the effects of decreasing pCO_2. The focus of this chapter is on the processes which control the shoaling of the NADW cell.

4.1 Overturning

The LGM*xxx* simulations show that the AMOC response to a GHG reduction is a function of the GHG concentration itself. The AMOC profiles of LGM353 and LGM284 at 30°N are indistinguishable from each other, both in terms of the NADW cell strength and its depth (Fig. 4.1 and Fig. 4.2 a and b). For pCO_2 below 284 ppm, the overturning decreases approximately linearly with the decreasing radiative forcing in steps of about 2 Sv per ΔRF. The shoaling of the NADW cell sets in only for pCO_2 below 230 ppm (Fig. 4.1 and Fig. 4.2 c). LGM353, LGM284 and LGM230 all have the same overturning geometry with a cell boundary near 3200 m. In LGMref, the cell boundary is then located at 2900 m, and in LGM149 it shifts further upward to 2600 m. LGM149 is the only experiment in which the NADW cell becomes shallower than in piCTL (Fig. 4.1 and Fig. 4.2 d). The overturning strength of 18 Sv in LGM149 still exceeds the preindustrial overturning strength. Hence, the overturning state in LGM149 is consistent with the glacial cold mode indicated by the reconstructions (*Lippold et al.*, 2012; *Böhm et al.*, 2015; *Lippold et al.*, 2016). Therefore, I conclude that the AMOC in LGM149 is in better agreement with reconstructions than the AMOC in LGMref. The reason for this will be explored in the remainder

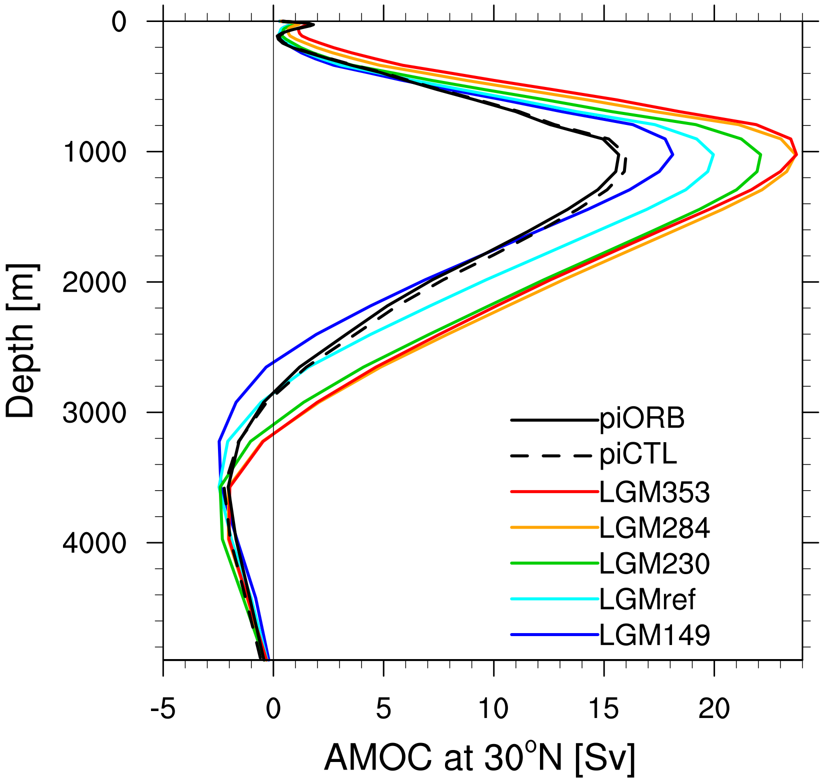

Figure 4.1: Profile of the AMOC at 30°N for the different experiments. Experiments with LGM setup are shown in colour, piCTL and piORB are shown in black.

of this chapter.

4.2 NADW formation

Deep mixed-layer depths (MLD) are a good indicator of deep convection. In both piCTL and piORB, NADW formation through deep convection takes place mainly in the ice-free part of the Nordic Seas (Fig. 4.3 a, only piCTL is shown). In the Labrador Sea, deep convection varies on pentadal to decadal time scales with years in which MLDs become as deep as 3400 m and years in which no deep convection occurs. In addition, the exact location of the deep convection varies in time. The long-term mean MLDs in the Labrador Sea are therefore rather shallow with 400 to 600 m. Higher-resolution versions of MPI-ESM simulated continuous deep convection in the Labrador Sea (see e.g., *Jungclaus et al.*, 2013). However, the different behaviour of the Labrador Sea convection does not affect the total glacial response of the AMOC.

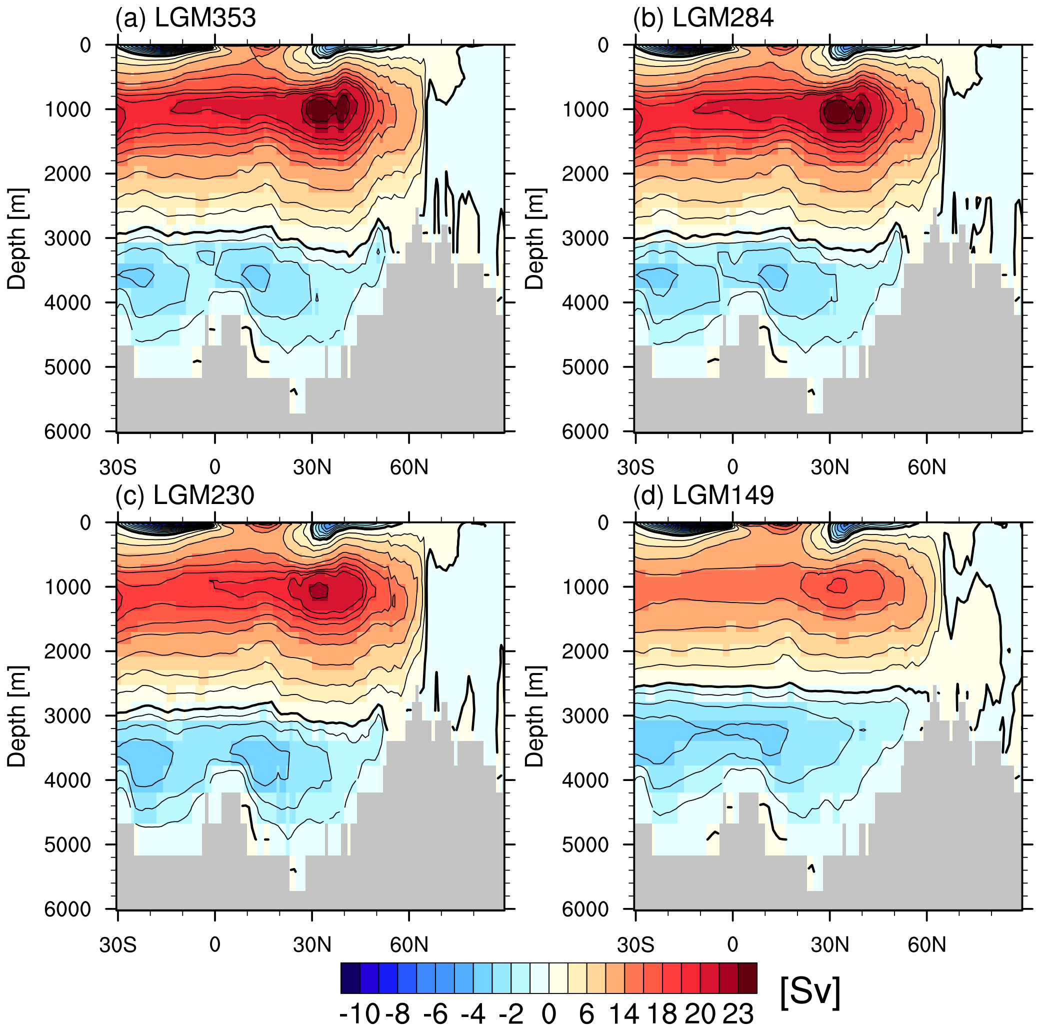

Figure 4.2: Atlantic meridional overturning stream function for **(a)** LGM353, **(b)** LGM284, **(c)** LGM230 and **(d)** LGM149. Red shading indicates clockwise, blue shading anti-clockwise flow. Note that the contour levels are not symmetric.

Comparing the preindustrial control simulation and the LGM simulation of MPI-ESM-P in the CMIP5/PMIP3 database shows that the depth of the NADW cell remains almost unchanged and the maximum overturning strength increases (see Table 1 in *Muglia and Schmittner*, 2015).

In the relatively warm glacial experiments LGM353 and LGM284, the deepest mixed layers are found in the Labrador Sea (Fig. 4.3 b and c). There is also deep convection in the Nordic Seas, but the extent of the convection area is reduced in comparison to piCTL, because sea-ice cover in the Nordic Seas increases in the glacial setup. With decreasing pCO_2, the sea-ice edge advances southwards in the Nordic Seas both in summer and winter, and deep convection decreases. In the Labrador Sea, the sea-ice edge advances eastwards and the deep-water formation area shifts with it. In LGM149, the main deep-water formation area is located in the central SPG and the eastern North Atlantic (Fig. 4.3 f).

4.3 Water-mass properties

To understand how the deep-water formation drives the overturning it is not sufficient to look only at the Northern Hemisphere. The overturning strength and geometry are set to a large extent by the density difference between NADW and AABW. In the following, I analyse how the properties of the two water masses change with decreasing pCO_2. I choose the Nordic Seas and the North Atlantic to study the NADW properties and the Weddell Sea to study the AABW properties. In each region, I select a fixed depth representative of the water-mass properties in this region. In the Nordic Seas, the water-mass properties are determined at 560 m depth which corresponds to the depth of the deepest model layer with a connection between the glacial Nordic Seas and the glacial North East Atlantic. In the North Atlantic and the Weddell Sea, the water-mass properties are determined at 2000 m depth because this depth is representative of the core properties of NADW. The spatial maximum of the climatological mean in-situ density on the selected level within each region is then determined (Fig. 4.4 a and b) and the corresponding temperature and salinity compared (Fig. 4.4 c). The in-situ density is converted to potential surface density (σ_Θ) and potential density referenced to 2000 m (σ_2) for the comparison.

In the North Atlantic, density (σ_Θ and σ_2) increases with decreasing pCO_2 (circles in Fig. 4.4 a and b). The density increase is caused by cooling, which dominates the effect of a simultaneous freshening (circles in Fig. 4.4 c). σ_2 increases quasi-linearly with decreasing radiative forcing; σ_Θ increases less below a pCO_2 of

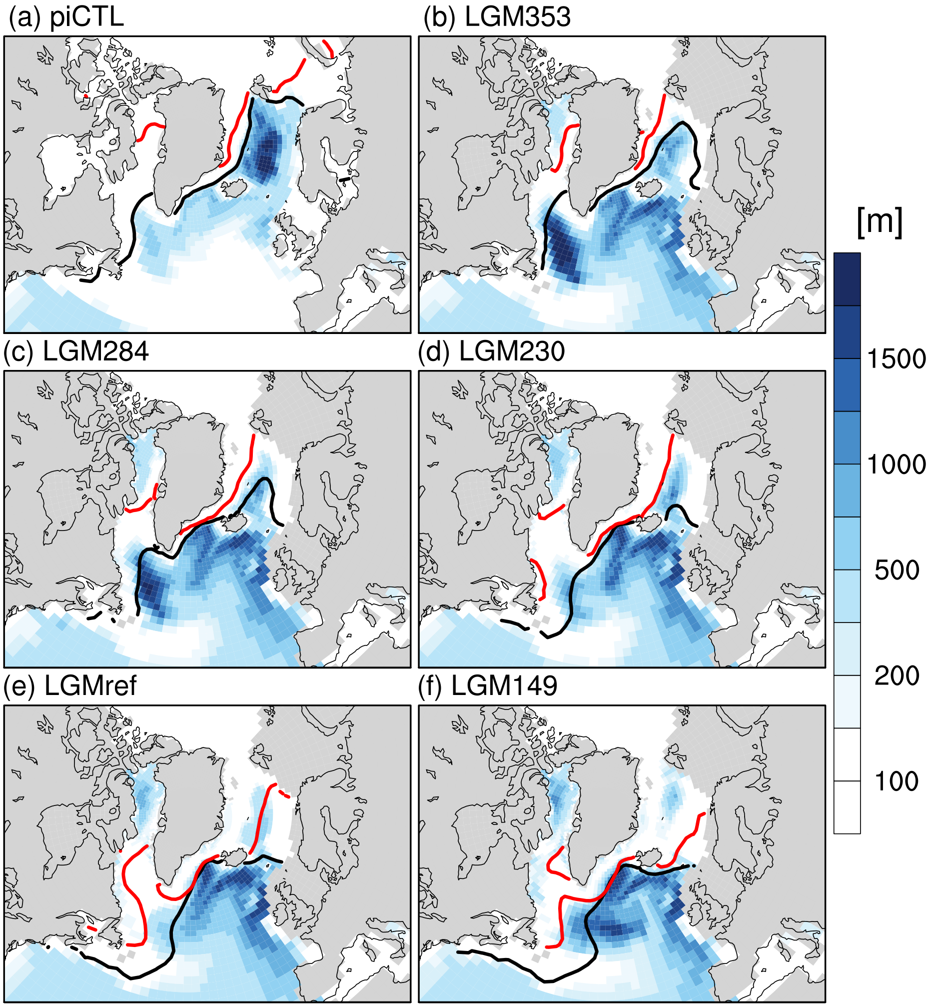

Figure 4.3: Climatological mean winter (JFM) mixed layer depth (shading), winter (JFM) ice edge (30 percent coverage, black contour) and summer ice edge (30 percent coverage, red contour).

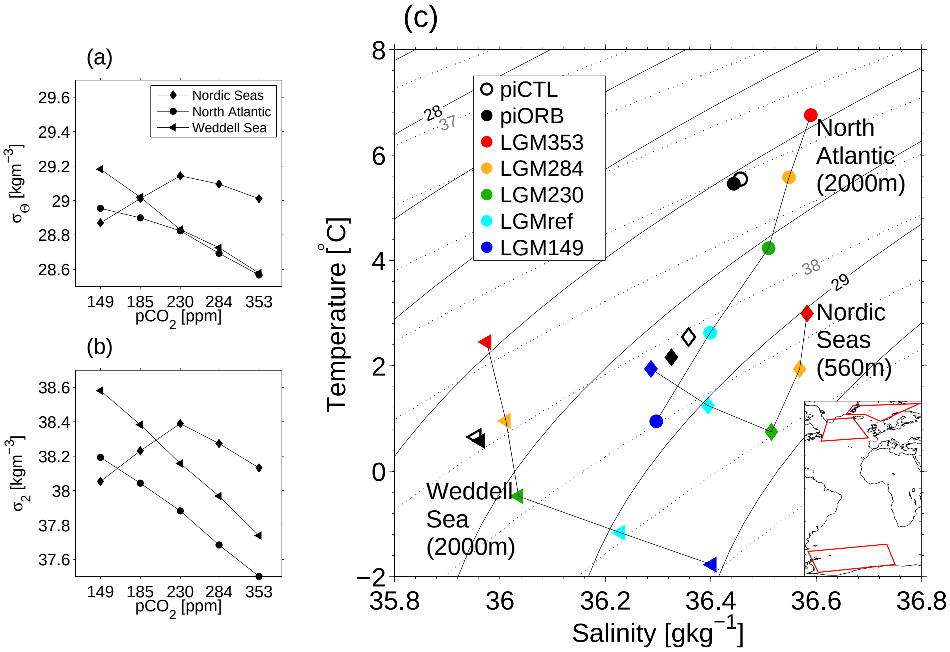

Figure 4.4: Maximum of **(a)** σ_Θ and **(b)** σ_2 at 560 m in the Nordic Seas and at 2000 m in the North Atlantic and Weddell Sea as a function of pCO_2 in the glacial setup. **(c)** Temperature and salinity corresponding to the maximum density in each region. Solid contours indicate σ_Θ, dotted contours indicate σ_2. The contour interval is 0.2 kg m^{-3}. For an easier comparison with the glacial setup runs, the salinity of piCTL and piORB has been offset by 1.21 g kg^{-1} to account for the global mean salinity difference caused by the lower glacial sea level. The small map shows the definition of the three selected regions.

230 ppm because the relative importance of the freshening effect on surface density increases at lower water temperatures.

In the Nordic Seas, both σ_Θ and σ_2 initially increase with decreasing pCO_2 until 230 ppm; at lower pCO_2 both decrease (diamonds in Fig. 4.4 a and b). The initial increase is caused by cooling, the subsequent decrease by freshening and warming (diamonds in Fig. 4.4 c). From 353 to 230 ppm, there is deep convection in the Nordic Seas associated with a strong surface-density gain and heat loss. The water that is leaving the Nordic Seas is contributing to NADW formation, because it is much denser than that south of the Greenland-Scotland Ridge. Below 230 ppm, however, the Nordic Seas are completely ice covered during winter and only little or no deep convection occurs in LGMref and LGM149, respectively. The water that enters the Nordic Seas is merely recirculated without gaining density and the water that flows out over the Greenland-Scotland Ridge is too light to contribute to NADW formation.

In the Weddell Sea, both σ_Θ and σ_2 increase with decreasing pCO_2 (triangles in Fig. 4.4 a and b). From 353 to 230 ppm, the density increase is dominated by cooling (triangles in Fig. 4.4 c). The salinity changes are positive but relatively small. Below 230 ppm, the density increase is dominated by a strong salinity increase. The cooling weakens as the Weddell Sea temperature approaches the freezing point. Even though the dominant process switches from cooling to salinity increase, σ_2 increases quasi-linearly with decreasing radiative forcing. The increase of σ_Θ, on the other hand, strengthens below 230 ppm.

The salinity increase in the Weddell Sea and the freshening of the North Atlantic lead to a reduction and ultimately to a sign reversal of the north-south salinity gradient, with AABW becoming saltier than NADW in LGM149. Hence, I conclude that the simulated state of the overturning and the Southern Ocean water masses in LGM149 are closer to the glacial state described by proxies than the state simulated in LGMref: The NADW cell becomes significantly shallower as compared with piCTL, and the North-South salinity gradient in the deep Atlantic is reversed with respect to the present day. This underlines the key role of the Southern Ocean salinity for the glacial AMOC state.

4.4 The surface density flux in the Weddell Sea

To understand the salinity increase in the Southern Ocean, I analyse the different components of the surface density flux in the Weddell Sea (defined as the region between 0 to 60°W and south of 60°S). The surface density flux is defined as the sum of the density changes due to heat fluxes, atmospheric freshwater fluxes (precipitation - evaporation + runoff) and brine release. The respective components are integrated over two different regions, the Weddell Sea shelves and the area in which open-ocean convection occurs. This way, the relative importance of shelf convection and open-ocean convection for the formation of AABW can be estimated.

I define the shelf region as the area between the coast and the 1000 m isobath. Defining the open-ocean convection area is less straightforward because the sign and magnitude of the density flux over the open-ocean convection area is very sensitive to the definition of the latter. The most appropriate approach in terms of the flux balance would be to consider only the area in which deep convection occurs (e.g., defined by maximum MLDs exceeding 2000 m). But the integrated fluxes would be difficult to compare this way, because the extent of the deep-convection area varies strongly between the respective experiments. I therefore choose two different approaches, each with a fixed definition of the open-ocean convection area. The first approach considers every grid point in which the annual-maximum MLD in *any* of the experiments exceeds 2000 m (OOC_{max}). The second approach considers only those grid points in which the annual-maximum MLD in *all* experiments exceeds 2000 m (OOC_{min}). The OOC_{max} case is more representative of the cold experiments with a very extensive open-ocean convection area, the OOC_{min} is more representative of the warm experiments with a smaller open-ocean convection area.

Over the shelves, there is a net density gain in all experiments (Fig. 4.5 a). The gain is determined entirely by the balance of the brine component and the freshwater component. The heat-flux component is very small because the surface water is close to the freezing point and therefore further heat loss leads to sea-ice formation and contributes to the brine component. The brine release causes a density gain which remains approximately constant with decreasing pCO_2 except for a stronger increase in LGM149. The freshwater flux causes a density loss which decreases with decreasing pCO_2 as the atmosphere can hold less moisture with decreasing air temperature. As a result, the net density gain over the shelves increases with decreasing pCO_2.

Over the open-ocean convection area (Fig. 4.5 b and c), there are two different regimes, a thermal and a haline regime. The thermal regime occurs in LGM353 and LGM284. For this regime, the OOC_{min} case best describes the surface density flux. There is a net density gain caused by heat loss. The brine component is negative, reducing the density gain through net sea-ice melt. Because the considered area in the OOC_{max} case is larger than the actual open-ocean convection area, the sea-ice melt dominates the net density flux, resulting in an overall density loss in the OOC_{max} case. The haline regime occurs in LGMref and LGM149. Here, the density gain is dominated by brine release. As over the shelves, the heat-flux component becomes small because the water temperature is already close to the freezing point. This is true for both the OOC_{max} and the OOC_{min} case. The OOC_{min} case, however, underestimates the effect of the brine release because the considered area is smaller than the actual open-ocean convection area. The balance in LGM230 lies in between the two regimes, the brine component is close to zero and the heat-flux component and the freshwater component add to a small density loss.

The annual mean density at 500 m averaged over the respective regions shows that the shelf water is lighter than the open-ocean convection water in LGM353 and LGM284 (Fig. 4.6). In LGM230, the potential density σ_Θ of the two water masses is very similar, and in LGMref and LGM149, the shelf waters become denser than the open-ocean convection water. So only in these two experiments can the very salty waters from the shelves reach deeper layers and contribute to AABW formation. Hence, I conclude that the contribution of Weddell Sea shelf waters to AABW is key to the shoaling of the NADW cell in response to the GHG reduction in MPI-ESM.

4.5 The effect of brine release

Only those PMIP2 models which simulated a north-south salinity gradient similar to the one reconstructed by *Adkins et al.* (2002) also simulated a shallower NADW cell under glacial conditions. These models had a strong haline contribution to the surface density flux in the Southern Ocean, driven by sea-ice formation and brine release (*Otto-Bliesner et al.*, 2007). The importance of brine release for the glacial overturning state in a CCSM3 simulation had already been identified by *Shin et al.* (2003). However, so far no study has tried to quantify the effect of brine release on the glacial overturning. In order to estimate the effect of brine release for the AABW formation and overturning strength in the glacial simulations, I perform three additional sensitivity experiments in which brine release on the Southern Hemisphere is reduced. To this end, I set the salinity of sea ice to 20 g kg^{-1} on the Southern Hemisphere (instead of 5 g kg^{-1}), thus reducing the amount of brine that is released when sea ice is formed in the Southern Ocean by roughly 50 %. I apply these changes to piORB, LGMref and LGM149 (see piORB_brine, LGMref_brine and LGM149_brine in Table 2.2) and analyse the effect of the reduced brine release on the surface density

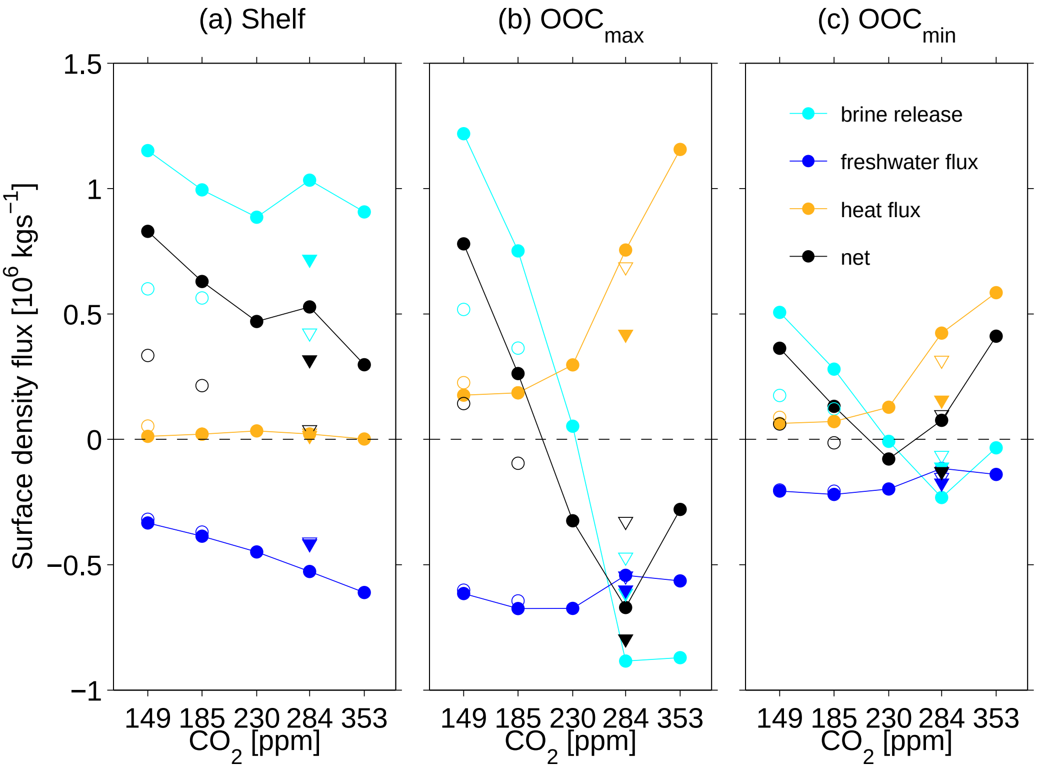

Figure 4.5: Components of the annual mean density flux integrated over different regions of the Weddell Sea as a function of pCO_2 integrated over **(a)** the shelf area defined by the 1000 m isobath, **(b)** the open-ocean convection area defined by the maximum extent of MLD>2000 m from all experiments and **(c)** the open-ocean convection area defined by the minimum extent of MLD>2000 m from all experiments. Positive values indicate a density gain, negative values a density loss. The x-axis is scaled logarithmically. Open symbols indicate the experiments with reduced brine release. Circles indicate the LGM*xxx* experiments, the triangles represent the piORB experiments.

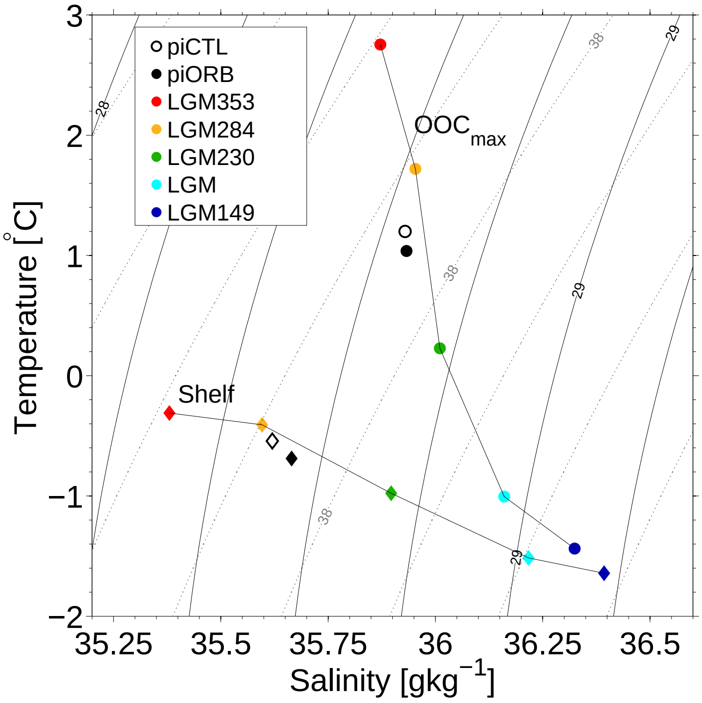

Figure 4.6: Annual mean temperature and salinity at 500m averaged over the Weddell Sea shelf region (diamonds) and the OOC$_{max}$ region (circles). Solid contours indicate σ_Θ, dotted contours indicate σ_2. The contour interval is 0.2 kg m^{-3}. For an easier comparison with the glacial setup runs, the salinity of piCTL and piORB has been offset by 1.21 g kg^{-1} to account for the global mean salinity difference caused by the lower glacial sea level.

flux, the Atlantic hydrography and the overturning.

4.5.1 Surface density flux changes

As expected, shelf convection is weakened in all three sensitivity experiments because the net density gain over the shelves is reduced as a direct consequence of the reduced brine release (open symbols in Fig. 4.5 a). Open-ocean convection is also reduced in the two glacial sensitivity experiments LGMref_brine and LGM149_brine (open circles in Fig. 4.5 b and c). In piORB_brine, however, open-ocean convection is enhanced with respect to piORB (open triangles in Fig. 4.5 b and c). In piORB, melting sea ice induces a density loss in the open-ocean convection area. This effect is weaker in piORB_brine because of the higher sea-ice salinity. The weaker density loss due to sea-ice melt and an increased density gain due to heat loss add to a net density gain in piORB_brine.

4.5.2 Atlantic hydrography changes

The resulting temperature and salinity differences between piORB_brine and piORB are relatively small (Fig. 4.7 a and d). The most prominent temperature signal is a northward shift of the Antarctic Circumpolar Current front. The northward shift is associated with an expansion of the open-ocean convection area in the Weddell Sea. The largest salinity change is also associated with the northward shift of the Antarctic Circumpolar Current front. A weak freshening of AABW occurs below 3000 m in the North Atlantic.

In LGMref_brine and LGM149_brine, the resulting temperature and salinity changes are much larger than in piORB_brine. In both experiments, there is a warming of up to 2.4 K below 3000 m (Fig. 4.7 b and c), which indicates that NADW replaces AABW in the deep North Atlantic. The salinity differences show a freshening of AABW and a salinity increase of NADW in both experiments (Fig. 4.7 d and f). The freshening of AABW and the salinity increase of NADW lead to a reduction of the density difference between the two water masses, as AABW becomes lighter and NADW becomes denser. Therefore, NADW can replace AABW in the deep North Atlantic.

4.5.3 Overturning changes

The response of the overturning reflects the hydrographic changes. Changes in overturning strength and geometry are very small from piORB to piORB_brine (Fig. 4.8).

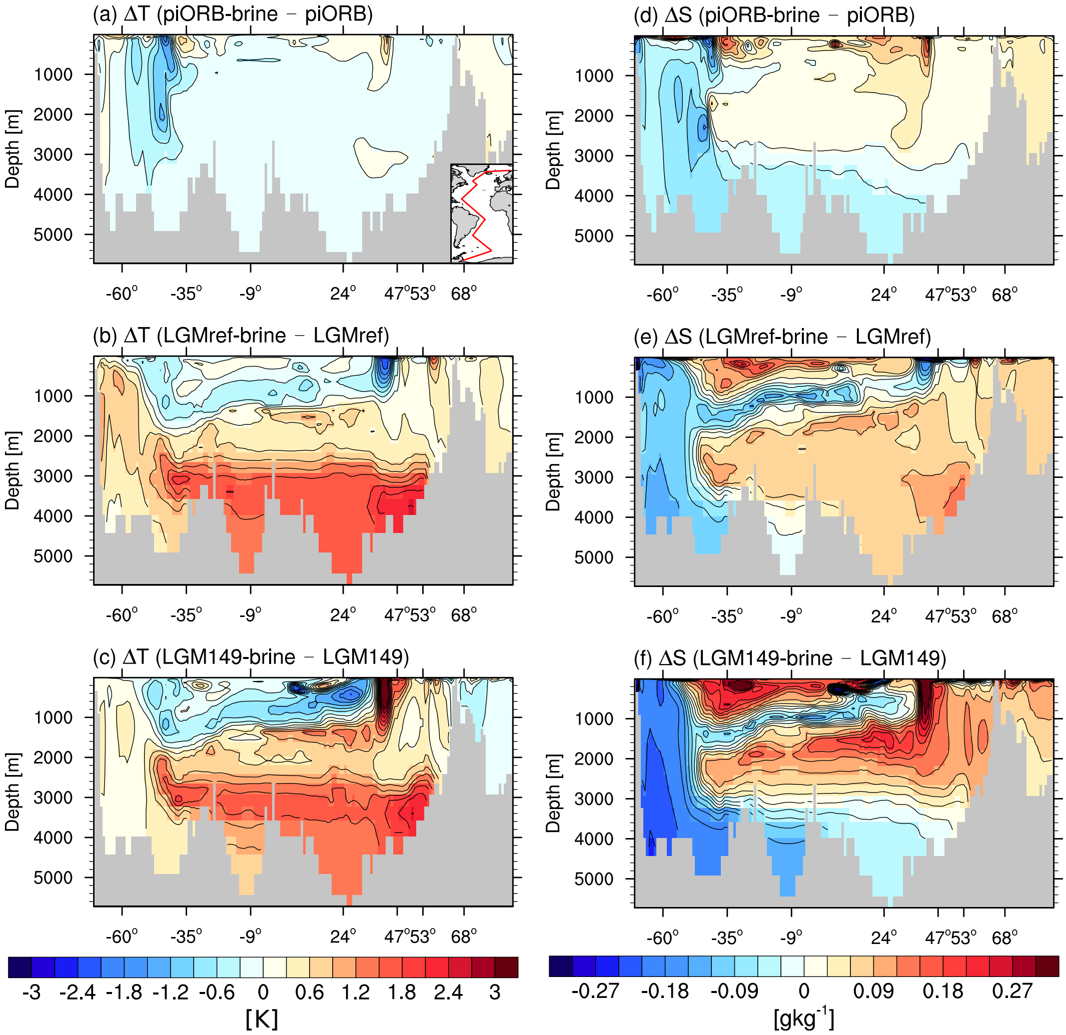

Figure 4.7: Temperature and salinity changes caused by the reduced brine release. Shown is the same transect through the Atlantic as in Fig. 3.5. Temperature difference for **(a)** piORB_brine – piORB, **(b)** LGMref_brine – LGMref and **(c)** LGM149_brine – LGM149. Salinity difference for **(d)** piORB_brine – piORB, **(e)** LGMref_brine – LGMref and **(f)** LGM149_brine – LGM149. Contour intervals are 0.3 K and 0.03 g kg^{-1}, respectively.

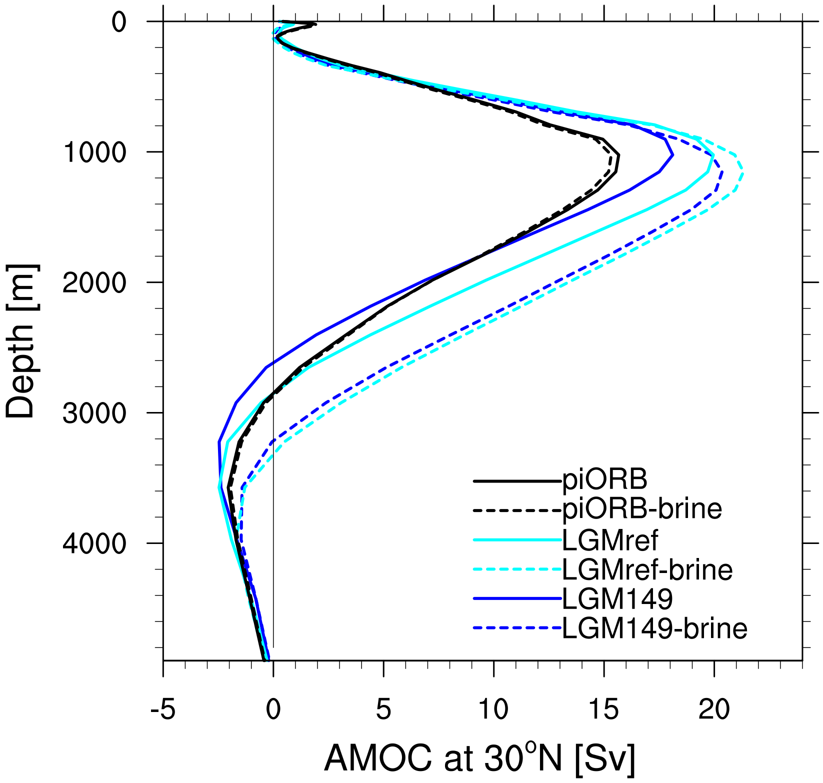

Figure 4.8: Profile of the AMOC at 30°N. Experiments with reduced brine release are indicated by dashed lines.

In both LGMref_brine and LGM149_brine, the lighter AABW induces a weakening of the AABW cell and the NADW cell deepens and strengthens. In LGM149_brine, the effect is strongest with a deepening of the NADW cell of 600 m and an increase in overturning strength of 2.5 Sv. These results confirm that the contribution of the very salty coastal water to the formation of AABW is key to the shoaling of the NADW cell in LGMref and LGM149 in MPI-ESM.

4.6 Discussion

Previous studies have identified both the Southern Ocean and the North Atlantic as the origin of the salinity increase and expansion of AABW and the subsequent shoaling of the NADW cell. A comparison of the water-mass formation rates of NADW and AABW in modern and glacial simulations of CCSM3 suggested that the shoaling of the NADW cell in the glacial simulation was caused by changes in the Southern Ocean haline density flux and not by changes in the North Atlantic density flux (*Shin et al.*, 2003). The changes in the Southern Ocean haline density flux were attributed to the expansion of Antarctic sea ice and brine release (see also *Ferrari et al.*, 2014). Simulations with a regional ocean model coupled to an ice-shelf-cavity model, on the other hand, suggested that the cooling of NADW was the driver of the salinity increase of AABW (*Miller et al.*, 2012; *Adkins*, 2013). Colder NADW would decrease the basal melting of the Antarctic ice sheet and thus increase the salinity of AABW. *Miller et al.* (2012) stated that the effect of increased brine release due to ocean cooling was negligible as it was compensated by decreased evaporation. It is, however, questionable whether the surface density flux in their experiments was representative of glacial conditions, because they used present-day forcing for the ocean model in all their experiments and cooled the water column directly at the open boundaries of the model domain. The changes of the haline density flux might therefore be underestimated in their experiments. Because MPI-ESM does not account for basal ice-sheet melt, the reduced basal ice-sheet melting cannot be the driver in the simulations presented here. The sensitivity experiments with reduced brine release confirm that changes in the haline density flux of the Southern Ocean are the main driver of the salinity increase of AABW and that brine release is a key factor for the shoaling of the NADW cell.

LGM149 is the only experiment in which a shoaling of the NADW cell with respect to the preindustrial state occurs. Further cooling than that induced by the glacial GHG concentrations is needed to overcome the deepening effect of the ice sheets. The shoaling takes place once the shelf-convection contribution to AABW becomes relevant. In piCTL, AABW is formed almost entirely through open-ocean convection, because the shelf waters are too fresh and too light (Fig. 4.6). This may be the result of missing shelf dynamics in the model and the simplified representation of ice-sheet mass loss. Therefore, the threshold beyond which changes in shelf convection become relevant appears to be located at a too low pCO_2 in MPI-ESM. The location of the threshold might depend on the way the ice-sheet runoff is treated in the model, because this has a direct effect on the freshwater flux (E-P+R). In MPI-ESM, the P-E over the ice sheets directly enters the runoff and is put into the ocean at the corresponding coastal grid point. This reduces the density immediately at the coast due to the additional freshwater input. The most realistic way to account for mass loss of the ice sheets would be to explicitly simulate the calving of icebergs, which then melt at lower latitudes. A simpler way, which does not require an explicit iceberg model, could be to put the ice-sheet runoff into the ocean at lower latitudes to account for the melting of the icebergs. *Stössel et al.* (2015) showed that the properties of present-day AABW improved if the ice-sheet runoff was distributed homogeneously over the Southern Ocean from the coast to 60°S instead of being put directly into the coastal grid points. This might also be true for the properties of glacial AABW.

The LGM*xxx* simulations presented in this chapter are a coupled-model equivalent of the experiment series HT-wind by *Oka et al.* (2012). The decreasing GHG concentrations correspond to the step-wise increase of glacial cooling in the heat-flux forcing of the ocean-only model. The prescribed glacial ice sheets correspond to the glacial wind-stress forcing. *Oka et al.* (2012) found that the cooling had to exceed the glacial level to cause the transition from the strong AMOC state to the weak AMOC state. In the LGM*xxx* experiments, there is no such abrupt transition. The AMOC decrease is rather gradual, at least within the studied range of pCO_2. It is possible that a similar transition could still occur at even lower pCO_2. It is also possible that the different response is an effect of the mixed boundary conditions in the stand-alone ocean model used by *Oka et al.* (2012) because mixed boundary conditions are known to cause an AMOC and deep convection that are overly sensitive to changes in forcing (e.g., *Mikolajewicz and Maier-Reimer*, 1994). Coupled model simulations, however, also indicated that the AMOC response to a doubling of pCO_2 depends on the prescribed ice sheets (*Zhu et al.*, 2015). To complete the analysis, I will therefore study the AMOC response to decreasing GHG concentration in the setup with preindustrial ice sheets in the following chapters.

4.7 Conclusions

Based on the LGM*xxx* simulations and the sensitivity simulations with reduced brine release in the Southern Ocean, I conclude the following:

- The AMOC is insensitive to a pCO_2 reduction from 353 ppm to 284 ppm. Below 284 ppm, the AMOC strength declines quasi linearly with decreasing radiative forcing.
- Within the studied pCO_2 range, there is no threshold beyond which an abrupt decline of the overturning strength occurs in the glacial setup.
- Brine rejection in the Southern Ocean is key to the shoaling of the boundary between NADW and AABW. Shoaling sets in only below an atmospheric pCO_2 of 230 ppm, when Southern Ocean shelf water becomes denser than open-ocean convection water and contributes significantly to AABW formation.
- The GHG concentrations needed to induce changes in the Southern Ocean shelf convection, which in turn result in a shoaling of the NADW cell and a reversal of the north-south salinity gradient with respect to piCTL, are too low in MPI-ESM. Therefore, the simulated state of the AMOC and the deep ocean in LGM149 is closer to the reconstructed glacial state than that in LGMref.

5 | Effect of different GHG concentrations in the preindustrial setup

This chapter discusses the effect of different GHG concentrations on the AMOC and the deep Atlantic water masses in the setup with preindustrial ice sheets. The first part of the analysis follows the concept of the analysis in Ch. 4, discussing the changes in the overturning, NADW formation and water-mass properties. Two distinct AMOC modes are identified and their stability is discussed in the last part of the chapter. It needs to be kept in mind that the radiative forcing difference between the simulations pi185 and pi149 is twice as large as the radiative forcing difference between the other pi*xxx* simulations. Between pi185 and pi149 it corresponds to ΔRF, and between the remaining simulations it corresponds to $0.5 \times \Delta RF$.

5.1 Overturning

As in the LGM*xxx* simulations, the NADW cell weakens and shoals with decreasing pCO_2 in the pi*xxx* simulations. But while the weakening is gradual in the simulations with glacial ice sheets, the NADW cell shows a strongly non-linear behaviour in the simulations with preindustrial ice sheets. There are two different AMOC modes: a strong, deep mode, which occurs in piORB, pi256 and pi230, and a weak, shallow mode, which occurs in pi185 and pi149 (see Fig. 5.1 a). The strong AMOC mode becomes *unstable* at a pCO_2 between 230 ppm and 206 ppm. The weak AMOC mode becomes *stable* at a pCO_2 between 206 ppm and 185 ppm (see Ch. 5.5 for details). In the pi206 simulation, neither the strong nor the weak AMOC mode are stable. As a consequence, the NADW cell does not reach a steady state in pi206. Instead, the NADW cell switches between the weak and the strong mode on millennial timescales (Fig. 5.1 b). The remainder of this chapter will only discuss the simulations in which a steady state is reached. Composites of the unstable weak and the strong phases in pi206 and the transitions between them will be discussed separately in Ch. 6.

The AMOC operates in the strong mode for the pCO_2 range of 284 to 230 ppm. Within this pCO_2 range, the strength of the NADW cell decreases linearly from 16 Sv in piORB to 13 Sv in pi230. This corresponds to an AMOC decrease of 3 Sv per ΔRF. The boundary between the NADW cell and the AABW cell shoals slightly from 2900 m to 2700 m. Within the pCO_2 range of 185 to 149 ppm, the AMOC operates in the weak mode. The strength of the NADW cell is 7 Sv in pi185 and 6 Sv in pi149. This corresponds to a decrease of 1 Sv per ΔRF. There is almost no significant further shoaling of the NADW cell in the weak AMOC mode. The cell boundary is located approximately at 2550 m in pi185 and at 2500 m in pi149.

5.2 NADW formation

5.2.1 Deep convection

To see how the location of NADW formation changes with decreasing pCO_2, I again compare the MLD patterns between the different pi*xxx* simulations, analogous to Ch. 4.2. During the strong AMOC mode, the main deep-convection sites are located in the Nordic Seas, the Labrador Sea and the Irminger Sea. In piORB, the deepest MLDs are located in the ice-free regions of the Nordic Seas. (Fig. 5.2 a). As described in Ch. 4.2, the Labrador Sea convection is highly variable in space and time, therefore the long-term average MLDs appear quite shallow. In pi256, the sea-ice edge in the Nordic Seas advances slightly to the southeast but the extent and depth of the deep convection area remain similar to piORB. (Fig. 5.2 b). In the Labrador Sea, the sea-ice edge advances eastwards and deep convection is reduced. This reduction is partly compensated for by an increase in convection in the Irminger Sea. In pi230, the sea-ice edge advances further towards the southeast in both the Nordic Seas and the Labrador Sea. The Nordic Sea convection is reduced with respect to piORB and pi256 and there is no more convection in the Labrador Sea.

The weak AMOC in pi185 and pi149 is sustained by sporadic deep convection, which is mostly confined to the Iceland basin, the Reykjanes Ridge and Rockall Trough. In pi185, deep-convection events with MLDs down to 2500 m occur every 10 to 15 years (not shown). One such event can last between one and five consecutive winters. As a result, the long-term mean MLDs in the Iceland basin do not

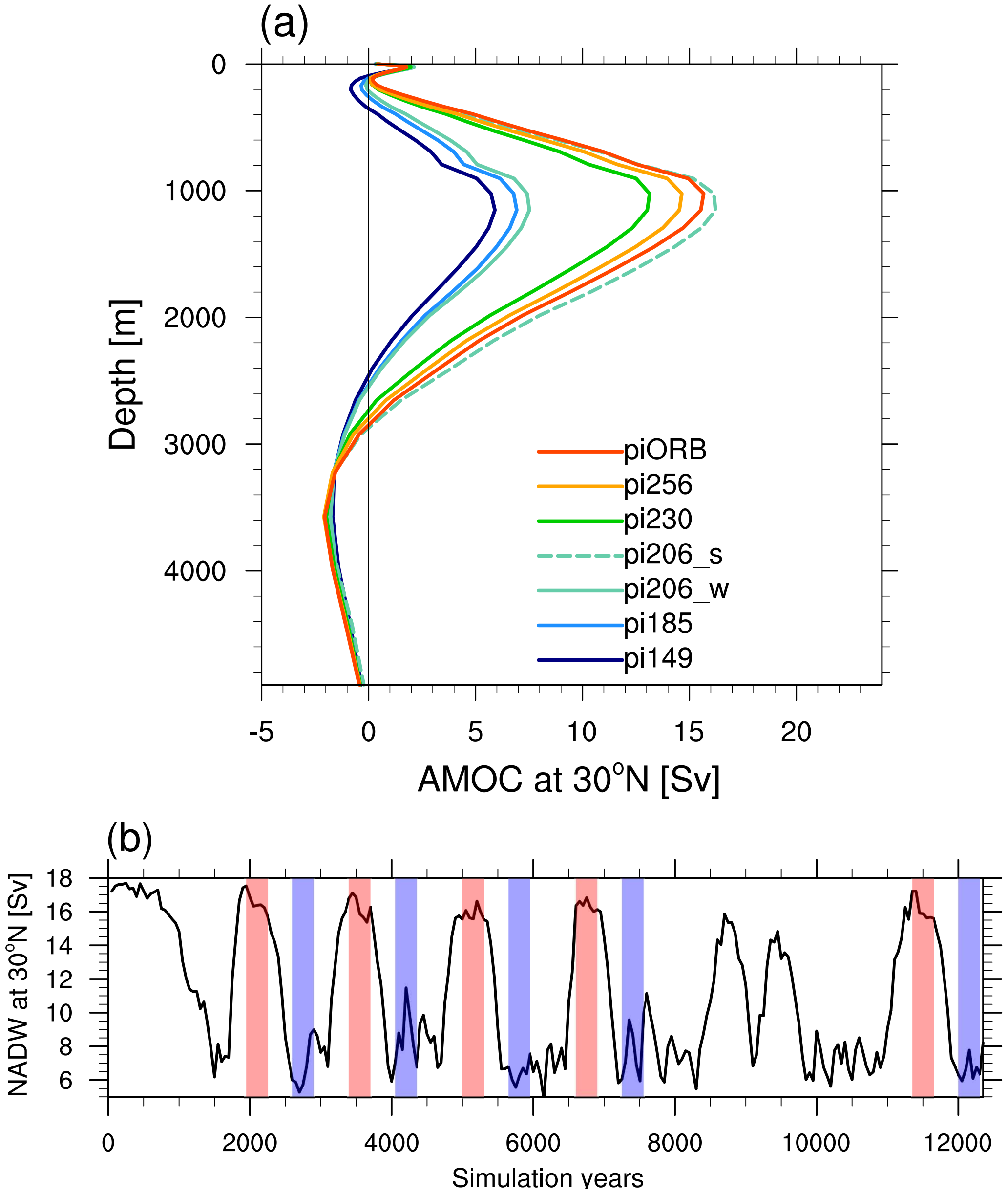

Figure 5.1: (a) Profile of AMOC strength at 30°N in the different experiments of the pi*xxx* series. **(b)** Time series of 50 year means of the maximum overturning strength at 30°N in pi206. The blue and red bars indicate the time spans used to form the composites of the weak and strong AMOC state, respectively.

exceed 500 m. In pi149, the long-term mean MLDs are even shallower, because the deep convection becomes less frequent. Deep-convection events occur only every 20 to 50 years, and MLDs range from 1600 to 2200 m during one event (not shown).

The Arctic Ocean is not a deep-convection site under preindustrial conditions. With decreasing pCO_2, however, MLDs in the Arctic Ocean increase. In piORB, there is a strong halocline in the Arctic Ocean, which prevents the formation of deep mixed layers. The halocline is maintained by freshwater input from the atmosphere and river runoff. This freshwater input exceeds the freshwater export by sea-ice export through the Fram Strait and the Barent Shelf by 48 mSv in piORB. With decreasing pCO_2, the atmospheric freshwater input decreases because the atmosphere holds less moisture. At the same time, the sea-ice export increases. In pi256, the net freshwater input into the Arctic is reduced to 7 mSv. In pi230, the freshwater export exceeds the input by 7 mSv. The halocline can no longer be maintained, and the Arctic mixed layer extends down to 2000 m. In the weak AMOC mode, sea-ice melt in the Nordic Seas is reduced. This leads to thicker sea ice in the Nordic Seas and to a smaller gradient in sea-ice thickness between the Arctic Ocean and the Nordic Seas. As a consequence, less freshwater is exported from the Arctic in the form of sea ice. The Arctic mixed layer depth becomes shallower again but the halocline cannot be re-established.

5.2.2 Surface density fluxes

The density budget over the convective regions can give further insight into the processes which drive the deep-water formation and help to characterise the two AMOC modes. The density fluxes are calculated in analogy to the OOC$_{max}$ case in Ch. 4.4. The area of integration is defined as all grid points in which the MLD in any of the pi*xxx* simulations exceed 1000 m. The budget is calculated for the North Atlantic including the Labrador Sea (Fig. 5.3 a) and for the Nordic Seas (Fig. 5.3 b) in order to estimate the relative importance between the deep-water formation regions north and south of the Greenland-Scotland Ridge. The Arctic Ocean is excluded from this analysis. Even though the mixed layers indicate ongoing deep convection in the Arctic Ocean at a pCO_2 of 230 ppm and below, the Arctic water is not dense enough to contribute to the formation of NADW (not shown).

Over the Nordic Seas, the net density flux during the strong AMOC mode is positive (i.e. a density gain). In piORB, the dominant contribution to the net density flux is the density gain due to heat loss. Sea-ice melt and atmospheric freshwater input induce a density loss but they are outweighed by the heat-flux contribution.

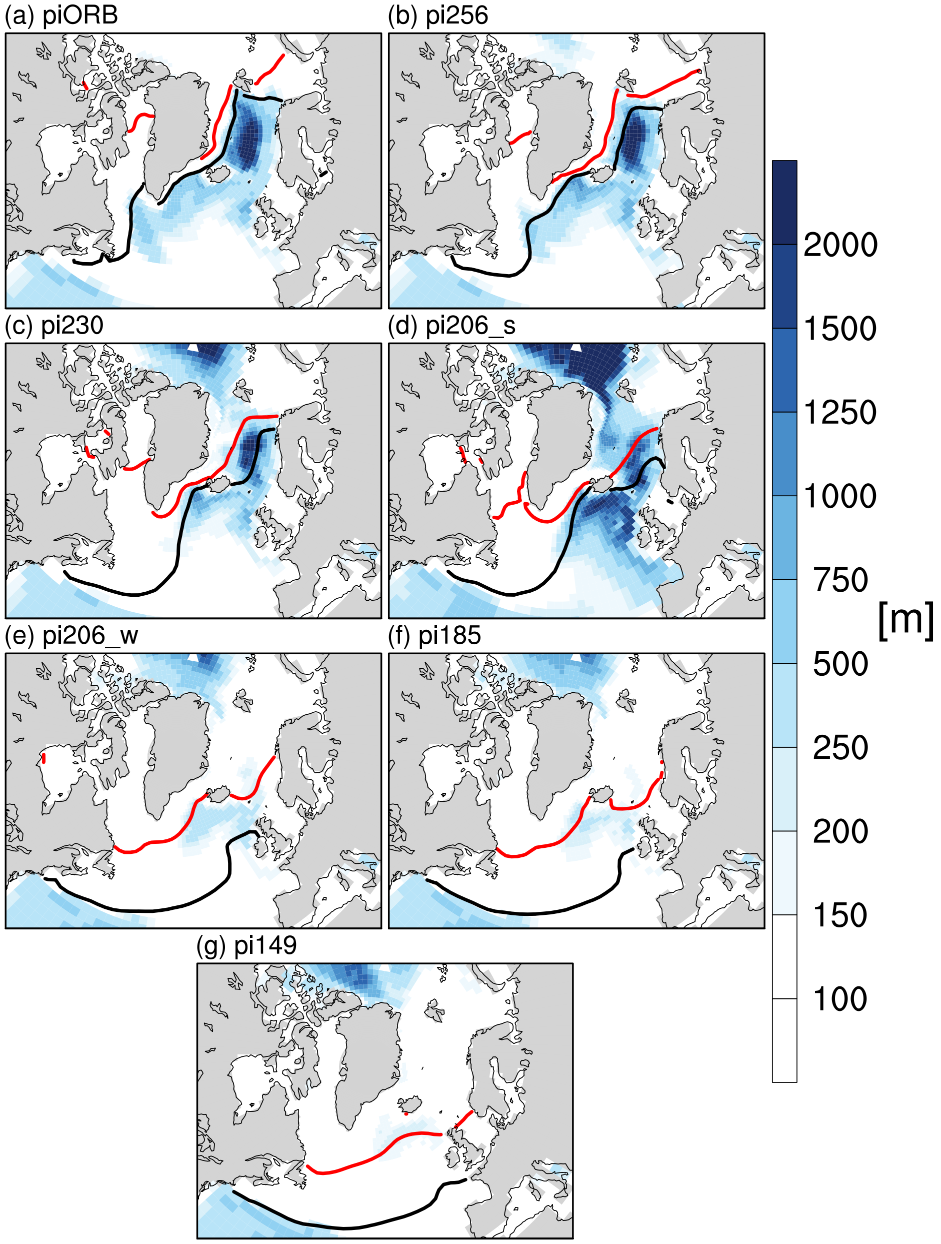

Figure 5.2: Maximum mixed layer depth from the 300-year climatologies (shading). The contours denote the 30% sea-ice cover isoline for maximum (black) and minimum (red) sea ice extent.

With decreasing pCO_2, the heat-flux contribution weakens. The water that enters the Nordic Seas is colder (see next section for more details), and its cooling potential decreases while the water temperature approaches the freezing point. As the heat-flux contribution decreases, the net density gain also decreases. In pi256, the heat-flux contribution is still strong enough to outweigh the density loss due to sea-ice melt and freshwater input. In pi230, the three contributions add up to a very small net density gain. During the weak AMOC mode, the heat-flux contribution is zero. As the Nordic Seas become completely ice-covered, the sea-ice formation induces a weak density gain which is compensated for by the atmospheric freshwater input. The resulting net density flux is almost zero in both pi185 and pi149.

Over the North Atlantic and Labrador Sea, as with the Nordic Seas, the strong AMOC mode is characterised by a large density gain due to heat loss. In piORB, the net density flux is almost entirely determined by the heat-flux component. The density gain due to heat loss is counteracted only by a comparatively small density loss due to freshwater input because the sea-ice contribution is close to zero. In pi256, the heat loss even increases with respect to piORB, but the net density gain is slightly smaller as a consequence of increasing sea-ice melt. In pi230, the net density gain decreases further because of decreased heat loss and increased sea-ice melt. During the weak AMOC mode, the net density flux is negative (i.e. a density loss) in the long-term mean. The positive heat-loss contribution results from the sporadic deep-convection events. This is consistent with the MLD pattern in pi185 and pi149 (Fig. 5.2 f and g). During these events, there is a net density gain (not shown) but in the long-term mean, the heat-flux contribution is outweighed by the sum of contributions from sea-ice melt and atmospheric freshwater input.

5.3 Water-mass properties

To get a better understanding of how NADW formation and the overturning state are linked, I again compare the NADW and AABW properties in their source regions (Fig. 5.4). The analysis follows the procedure in Ch. 4.3, but different depth levels are chosen for the analysis. Because the glacial sea level was approximately 120 m below the preindustrial sea level, the connection between the Nordic Seas and the North Atlantic is deeper in the preindustrial bathymetry than in the glacial bathymetry. In the pi*xxx* simulations, the deepest model layer with a connection between the Nordic Sea and the North Atlantic is centred at 650 m. In the Nordic Seas, I therefore analyse the water-mass properties at 650 m. In the North Atlantic,

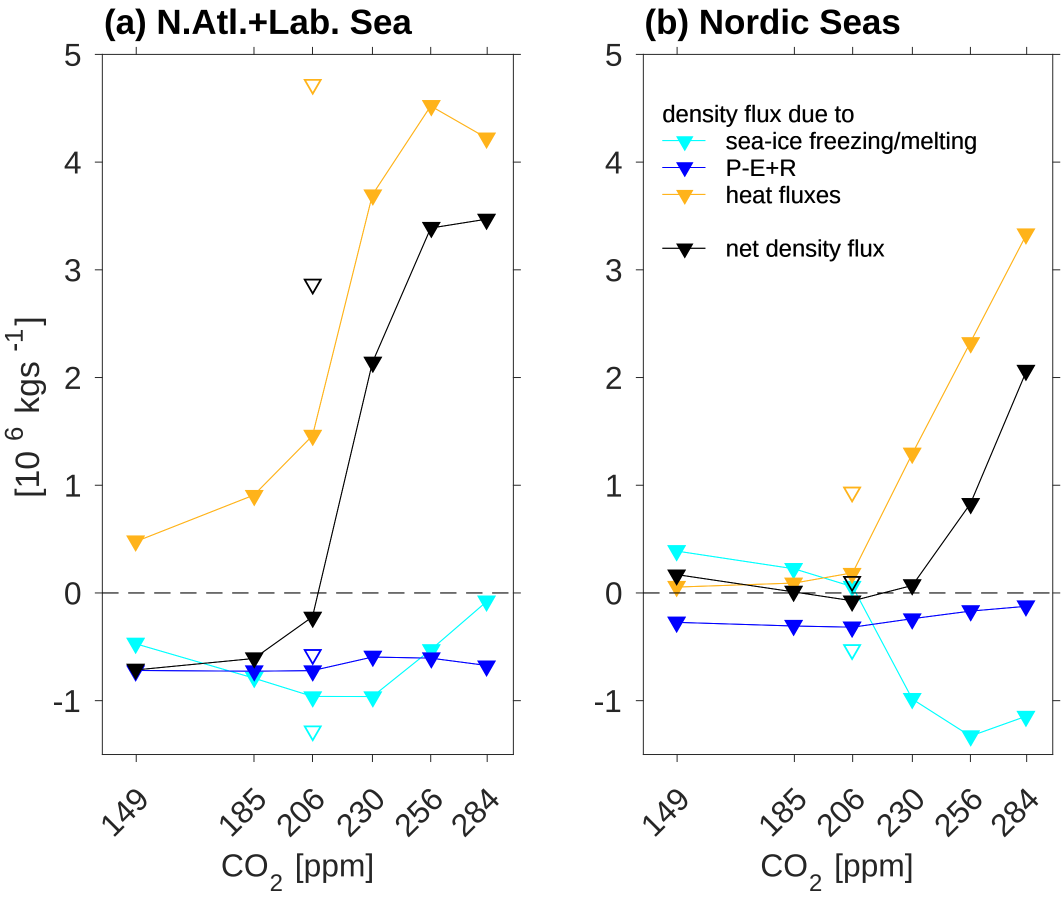

Figure 5.3: Annual mean net density flux (black) as a function of pCO_2, and its components: density flux due to heat loss or gain (orange), due to atmospheric freshwater input (blue) and due to sea-ice freezing and melting (cyan). The fluxes are integrated over the OOC_{max} region of **(a)** the North Atlantic including the Labrador Sea, and **(b)** the Nordic Seas. Positive values indicate a density gain, negative values indicate a density loss. The open symbols indicate the pi206_s composite. The x-axis is scaled logarithmically.

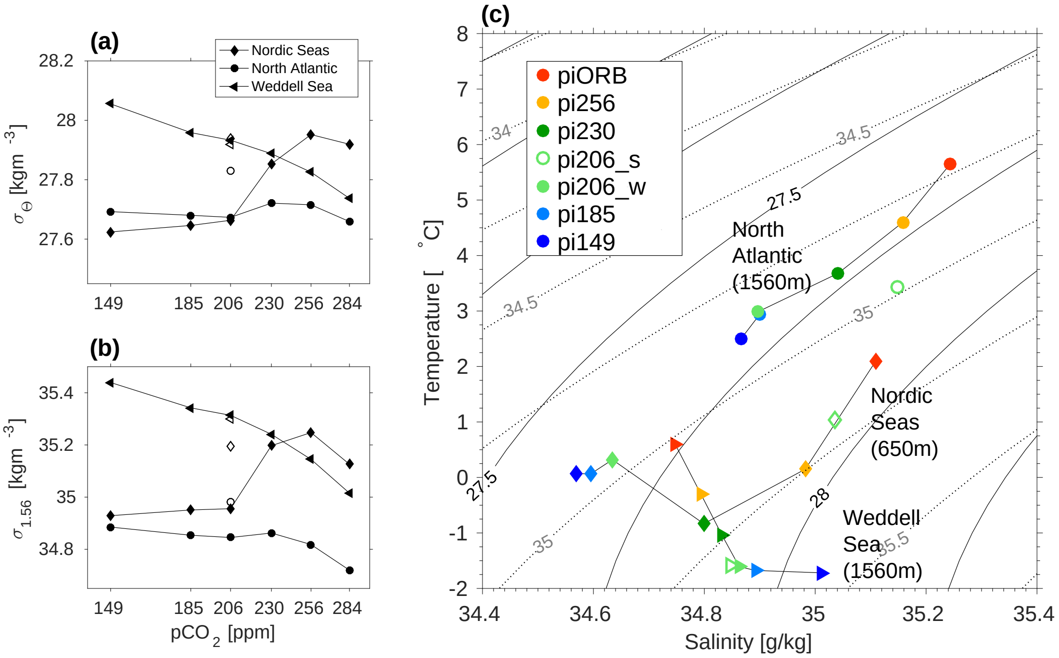

Figure 5.4: Maximum of **(a)** σ_Θ and **(b)** $\sigma_{1.53}$ at 650 m in the Nordic Seas and at 1530 m (diamonds) in the North Atlantic (circles) and Weddell Sea (triangles) as a function of pCO_2 in the setup with preindustrial ice sheets. The x-axis is scaled logarithmically. **(c)** Temperature and salinity corresponding to the maximum density in each region. Solid contours indicate σ_Θ, dotted contours indicate $\sigma_{1.53}$. The contour interval is 0.25 kg m^{-3}. Open symbols indicate the pi206_s composite.

the core of NADW is shifted upwards during the weak AMOC mode. Thus, 2000 m is no longer representative of the NADW properties. Instead, I compare the water-mass properties in the North Atlantic and the Weddell Sea at 1530 m. The water-mass properties on this level are representative of NADW also during the strong AMOC mode, because the water column in the North Atlantic is quite homogeneous between 1200 and 2000 m during the strong AMOC mode. The maximum in-situ density in every region is accordingly converted to σ_Θ and to $\sigma_{1.53}$ (potential density referenced to 1530 m) for the comparison.

In the North Atlantic, temperature and salinity decrease with decreasing pCO_2 during the strong AMOC mode (circles in Fig. 5.4). The effect of the cooling and that of the freshening on σ_Θ almost compensate for one another. There is only a very small increase in σ_Θ when pCO_2 is reduced to 256 ppm. Below 256 ppm, σ_Θ remains approximately constant. At 1530 m, the cooling effect still outweighs the freshening effect on density. As a result, $\sigma_{1.53}$ increases also when pCO_2 is reduced to 230 ppm. During the weak AMOC mode, the water cools and freshens further with respect to pi230 but σ_Θ and $\sigma_{1.53}$ remain approximately constant. Reducing pCO_2 from 185 to 149 ppm still induces a cooling and freshening, but the magnitude is much smaller as compared with the strong AMOC mode, and density remains constant.

In the Nordic Seas, the temperature and salinity decrease with decreasing pCO_2 during the strong AMOC mode (diamonds in Fig. 5.4). When the pCO_2 is decreased to 256 ppm, the cooling effect on density outweighs the effect of the freshening, and σ_Θ and $\sigma_{1.53}$ increase with respect to piORB. As in the North Atlantic, the increase in $\sigma_{1.53}$ is much larger than the increase in σ_Θ. When pCO_2 is reduced to 230 ppm, the water temperature approaches the freezing point, the freshening increases and its effect outweighs the cooling effect. As a result, both σ_Θ and $\sigma_{1.53}$ decrease with respect to pi256. In the weak AMOC mode, the water in the Nordic Seas freshens further and warms with respect to pi230. This results in much lower densities as compared with the strong AMOC mode. Once the AMOC operates in the weak mode, a further reduction of pCO_2 has only a very small effect on the water-mass properties in the Nordic Seas. Temperature, salinity and density remain almost the same in pi185 and pi149.

The source of the water in the deep Nordic Seas is different between the two AMOC modes. In the strong mode with active deep convection, the water-mass properties in the deeper Nordic Seas are set by surface fluxes. In the weak mode, the Nordic Seas are covered by sea ice and the surface fluxes become very small (Fig. 5.3 b). The water-mass properties are then primarily determined by the properties of the inflow from the North Atlantic. The Atlantic water recirculates in the Nordic Seas and its properties get only modified through entrainment.

In the Weddell Sea, both σ_Θ and $\sigma_{1.53}$ increase almost linearly with decreasing pCO_2, regardless of the AMOC mode (triangles in Fig. 5.4). During the strong AMOC mode, this density increase is caused by a cooling and a simultaneous salinity increase. During the weak AMOC mode, the water temperature has reached the freezing point, and the density increase from pi185 to pi149 is caused by a salinity increase alone.

The water-mass properties allow one to draw two main conclusions for the characterisation of the two AMOC modes. First, the density evolution in the source regions of NADW confirms that the Nordic Seas only contribute significantly to the NADW formation during the strong AMOC mode. In piORB, pi256 and pi230, the water in the Nordic Seas is denser than the water in the North Atlantic. In the weak AMOC mode, the water in the Nordic Seas becomes lighter than the water in the North Atlantic, at least in terms of σ_Θ (Fig. 5.4 a). Thus, it is not dense enough to contribute to the formation of NADW. Second, the response of salinity to decreasing pCO_2 determines the density difference between NADW and AABW. The density of AABW increases faster than that of NADW because the salinity of AABW *in*creases while the salinity of NADW *de*creases. The larger the density difference between the two water masses, the weaker the NADW cell becomes. In the simulations with glacial ice sheets, a reversed north-south salinity difference is crucial for the shoaling of the NADW cell. In the simulations with preindustrial ice sheets, the weak AMOC mode becomes stable when the north-south salinity difference reverses, and AABW becomes as salty (pi185) or saltier (pi149) than NADW. A possible explanation for the freshening of NADW during the strong AMOC mode is the increasing sea-ice melt as the pCO_2 is reduced (Fig. 5.3 a). Due to the colder climate more sea-ice is advected into the deep-convection sites and melts there. Feedbacks with the AMOC strength may also play a role in the freshening. The salinity increase of AABW is caused by brine release in the Southern Ocean, as was shown in Ch. 4.5 (more details follow in the next section).

5.4 The role of Southern Ocean salinity and brine release

The temporal evolution of density and salinity during the spin-up of pi185 gives additional support to the hypothesis that the north-south salinity difference is crucial for the density difference between NADW and AABW and consequently for the

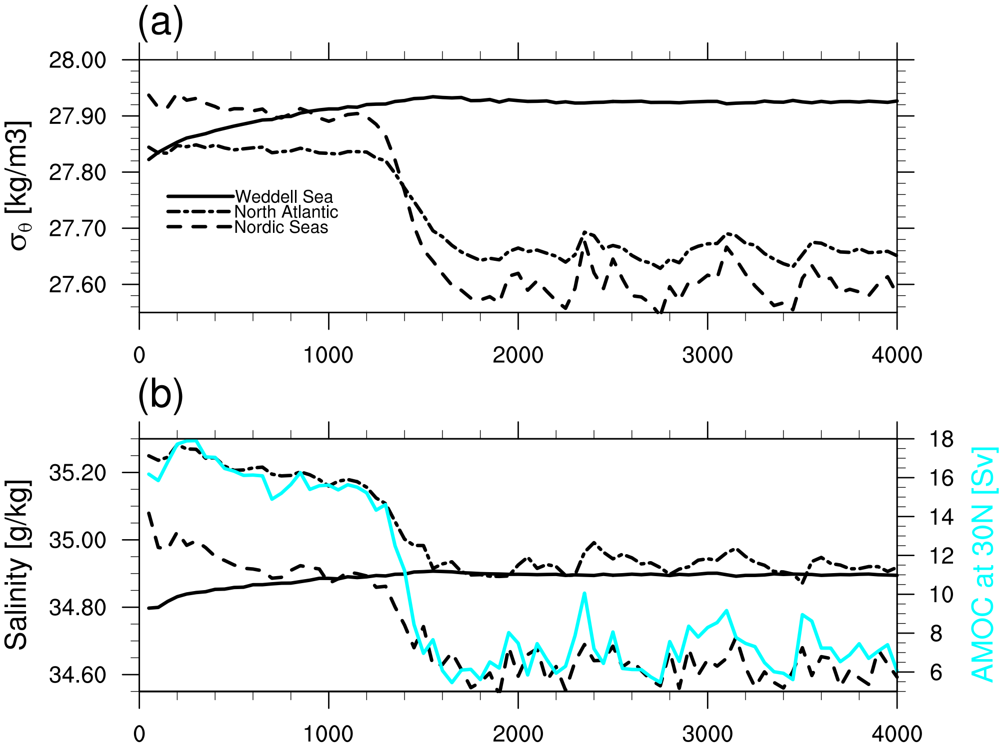

Figure 5.5: Time series of **(a)** σ_Θ and **(b)** salinity in the Weddell Sea (solid), the North Atlantic (dash-dot) and the Nordic Seas (dashed), as well as the NADW strength at 30°N. All time series are taken from pi185. σ_Θ and salinity are averaged over the same regions and at the same depth levels as in Fig. 5.4.

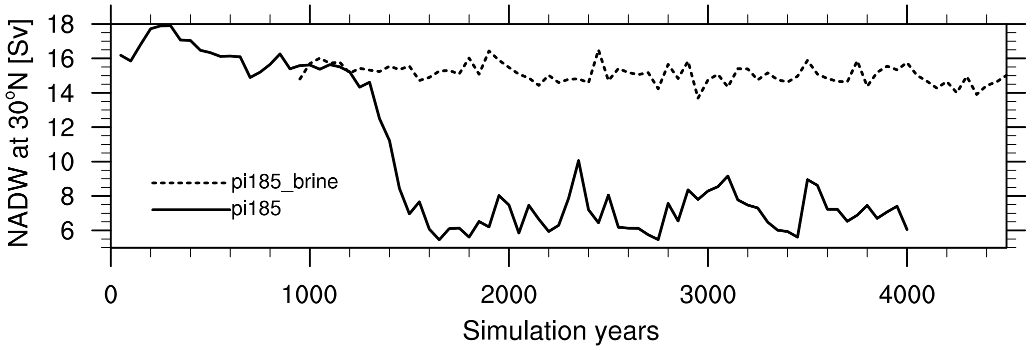

Figure 5.6: Times series of the overturning strength at 30°N in pi185 (solid) and pi185_brine (dashed).

state of the AMOC. As in Ch. 4.3, the north-south salinity difference is defined as the difference in salinity between the deep North Atlantic and the Weddell Sea (as shown in Fig. 5.4). The pi185 simulation is initialised from a preindustrial ocean state with an adjusted temperature field. The ocean temperature was reduced globally by 2 K as a best guess in order to shorten the spin-up period.

The salinity and σ_Θ of the Weddell Sea at 1530 m increase by 0.1 $\mathrm{g\,kg^{-1}}$ and 0.12 $\mathrm{kg\,m^{-3}}$, respectively, during the first 1400 years of the simulation and then stay approximately constant for the remaining 2600 years (Fig. 5.5). The salinity increase is caused by enhanced brine-release and shelf convection in the Southern Ocean in combination with reduced freshwater input from precipitation and runoff. At the same time, the salinity in the Nordic Seas and North Atlantic decreases as a consequence of the weakening AMOC. The AMOC decreases by approximately 3 Sv over the first 1300 years of the simulation. The density in the Weddell Sea becomes greater than the density in the Nordic Seas after about 1200 years, which coincides with the time when the Weddell Sea salinity exceeds the salinity in the Nordic Seas. The AMOC starts to decrease rapidly about 100 years later. The NADW cell weakens by 8 Sv in 200 years and then stays in the weak AMOC mode. The rapid AMOC decline is accompanied by a salinity decrease of about 0.2 $\mathrm{g\,kg^{-1}}$ in the North Atlantic and Nordic Seas. Once the AMOC has reached the weak state, the North Atlantic and Weddell Sea waters at 1530 m have the same salinity.

The spin-up of pi185 illustrates that the north-south salinity difference is determined by brine release in the Southern Ocean and by advective feedbacks with the AMOC strength in the North Atlantic. To test, whether the salinity of the Southern Ocean controls the stability of the two AMOC modes, I perform a sensitivity experiment with reduced brine release in the Southern Ocean (pi185_brine). The pi185_brine experiment is set up in analogy to LGMref_brine and LGM149_brine. The brine release in the Southern Ocean is again reduced by approximately 50 %. Otherwise, the setup is identical to pi185. The pi185_brine simulation is branched off pi185 during the spin-up phase after 900 years when the AMOC is still in the strong mode.

The AMOC in pi185_brine remains in the strong mode for the entire length of the simulation (see dashed line in Fig. 5.6). The pi185_brine simulation is integrated for 4000 years to make sure that no transition to the weak AMOC mode occurs at a later point. In pi185, the Atlantic below 2800 m is dominated by AABW (Fig. 5.7 a). The reduced brine release in pi185_brine causes a freshening of 0.06 $\mathrm{g\,kg^{-1}}$ in the Weddell Sea (Fig. 5.7 b). The associated density decrease of AABW allows for NADW to

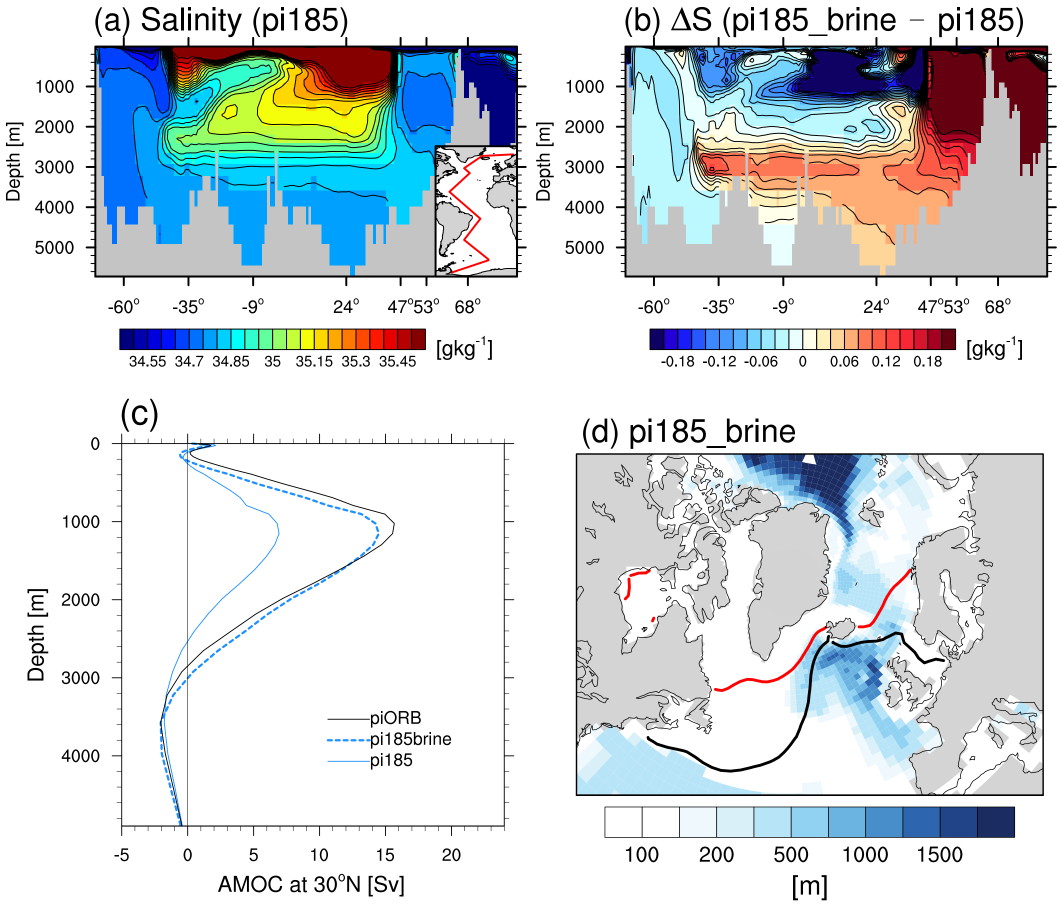

Figure 5.7: Effect of reduced brine release in the Southern Ocean: **(a)** Salinity section in pi185 through the Atlantic basin and **(b)** salinity difference between pi185_brine and pi185 along the same section. **(c)** Profile of the AMOC strength at 30°N in pi185 and pi185_brine. The AMOC profile in piORB is shown for comparison. **(d)** Mixed layer depth and sea-ice edge in pi185_brine.

penetrate deeper levels, and the percentage of NADW below 2800 m increases with respect to pi185. The deepening of the NADW cell is indicated by the increased salinity in the North Atlantic below 2800 m (Fig. 5.7 b) as well as by the change in the overturning stream function. In pi185_brine, the NADW cell is about 500 m deeper and about 7.5 Sv stronger than in pi185 (Fig. 5.7 c). The MLD patterns indicate deep convection over the Reykjanes Ridge, in the Iceland basin, the Nordic Seas and the Arctic Ocean (Fig. 5.7 d). The density at 650 m in the Arctic Ocean and Nordic Seas exceeds the density in the Irminger Basin by 0.12 to 0.15 kg m^{-3} (not shown). While the Arctic water in pi185 is not dense enough to contribute to NADW formation, the Arctic Ocean becomes an additional source for NADW in pi185_brine.

The strong and deep AMOC in pi185_brine supports the hypothesis that stability of the strong and the weak AMOC mode depends on the salinity and density of AABW. Hence, the north-south salinity difference determines the pCO_2 thresholds beyond which the strong AMOC mode becomes unstable and the weak AMOC mode becomes stable.

5.5 Two stability thresholds

If a system is in a stable state, a perturbation will always be dampened by restoring forces such as negative feedbacks, and the perturbed system will quickly return to its unperturbed state. Close to a bifurcation point beyond which the system becomes unstable, the restoring forces weaken and small perturbations can result in large changes in the system. A good indication for the presence of a stability threshold is, therefore, the increase of noise or temporal variability as the threshold is approached (*Tziperman*, 2000; *Knutti and Stocker*, 2002; *Kleinen et al.*, 2003). As a simple measure for the temporal variability, I compare the temporal standard deviation of the 50-year mean AMOC time series between the different simulations (Fig. 5.8). At 284 ppm (piORB), the standard deviation of the NADW strength lies between 0.4 Sv and 0.7 Sv. The largest standard deviation is located between 30°N and 45°N at a depth of 1000 m to 2000 m. With decreasing pCO_2, the standard deviation increases. At 230 ppm, the standard deviation of the NADW strength lies between 0.7 Sv and 1 Sv. At 206 ppm, the standard deviation increases to a maximum of 4.2 Sv (not shown), which reflects the amplitude of the state transitions in pi206 (Fig. 5.1 b). Below 206 ppm, the standard deviation decreases with decreasing pCO_2. At 185 ppm, the standard deviation lies between 0.85 Sv and 1.2 Sv. At 149 ppm, the standard deviation is reduced to 0.55 Sv to 0.85 Sv. Of the five simula-

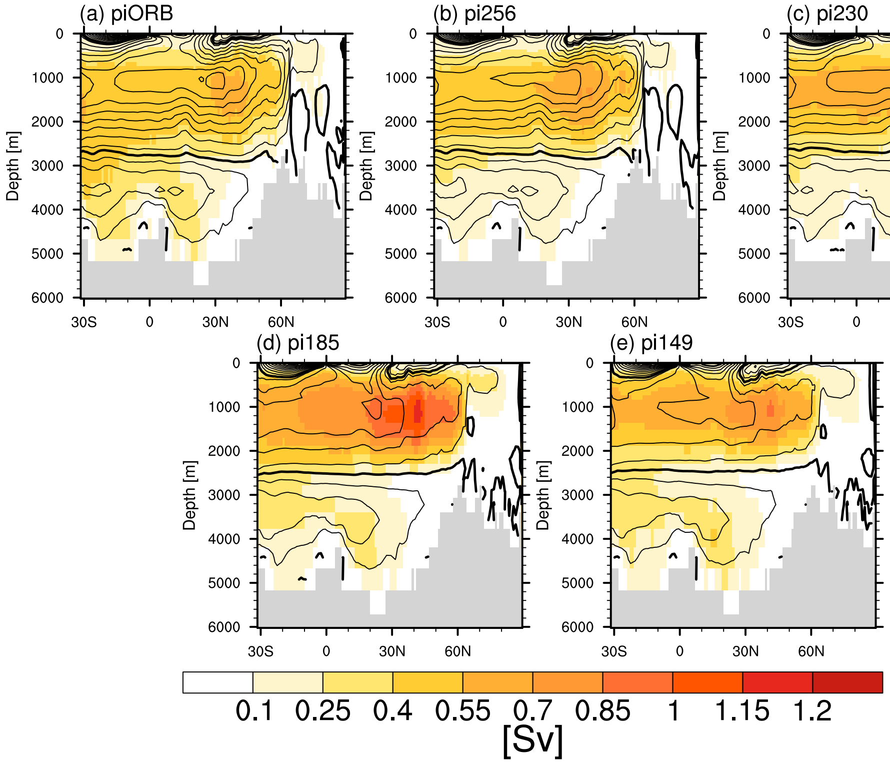

Figure 5.8: Standard deviation of the 50-year mean time series for the AMOC in (a) piORB, (b) pi256, (c) pi230, (d) pi185 and (e) pi149. The time series have been detrended before the calculation. The 300-year mean state of the AMOC is overlaid in contours. The contour levels are (-3,-2,-1,0,1,3,5,7,9,11,13,15,16). The thick line indicates the zero contour line.

tions shown in Fig. 5.8, the largest variability occurs in pi185. This suggests that the weak AMOC mode in pi185 is still relatively close to the second stability threshold.

The response of the temporal variability to decreasing pCO_2 can also be seen in other variables such as sea-ice concentration (Fig. 5.9 a to e) and ocean surface heat flux (Fig. 5.9 f to j). In all simulations, the largest standard deviation of the sea-ice concentration is located close to the climatological-mean 90 %-contour. With decreasing pCO_2, the 10 %-contour advances faster than the 90 % contour, and the area with strong temporal variability increases. The standard deviation increases from piORB to pi230 and decreases again from pi185 to pi149. The pattern of variability of the sea-ice concentration is closely linked to the pattern of the surface heat flux variability. Together, they reflect the variability of deep convection. A highly variable sea-ice cover and surface heat flux indicate deep convection which varies strongly in time. In periods with active deep convection, the heat release from the ocean reduces the sea-ice cover.

The change of temporal variability with decreasing pCO_2 indicates that there are two thresholds of atmospheric cooling. The first is located at a pCO_2 between 230 ppm and 206 ppm. The strong AMOC mode is stable above this first threshold and unstable below. The second threshold is located at a pCO_2 between 206 ppm and 185 ppm. The weak AMOC mode is unstable above the second threshold and stable below. The simulation pi206 lies exactly in the window between the two thresholds, where neither of the two modes are stable. Hence, the transitions in pi206 are a result of oscillations between two unstable modes (e.g. *Colin de Verdière*, 2007). The presence of the bifurcation points does not, however, explain which physical mechanisms are driving the transitions in pi206. In this chapter, I have shown that the north-south salinity difference is crucial for controlling the stability of the strong and the weak AMOC mode. In the following chapter, I will investigate the mechanism behind the transitions in pi206.

5.6 Conclusions

Based on the simulation series with preindustrial ice sheets and decreasing GHG concentrations I conclude:

- In the presence of preindustrial ice sheets, the AMOC has two possible modes: a strong and deep mode, which occurs at high pCO_2 between 284 ppm and 230 ppm and a weak and shallow mode, which occurs at low pCO_2 between 185 ppm and 149 ppm.

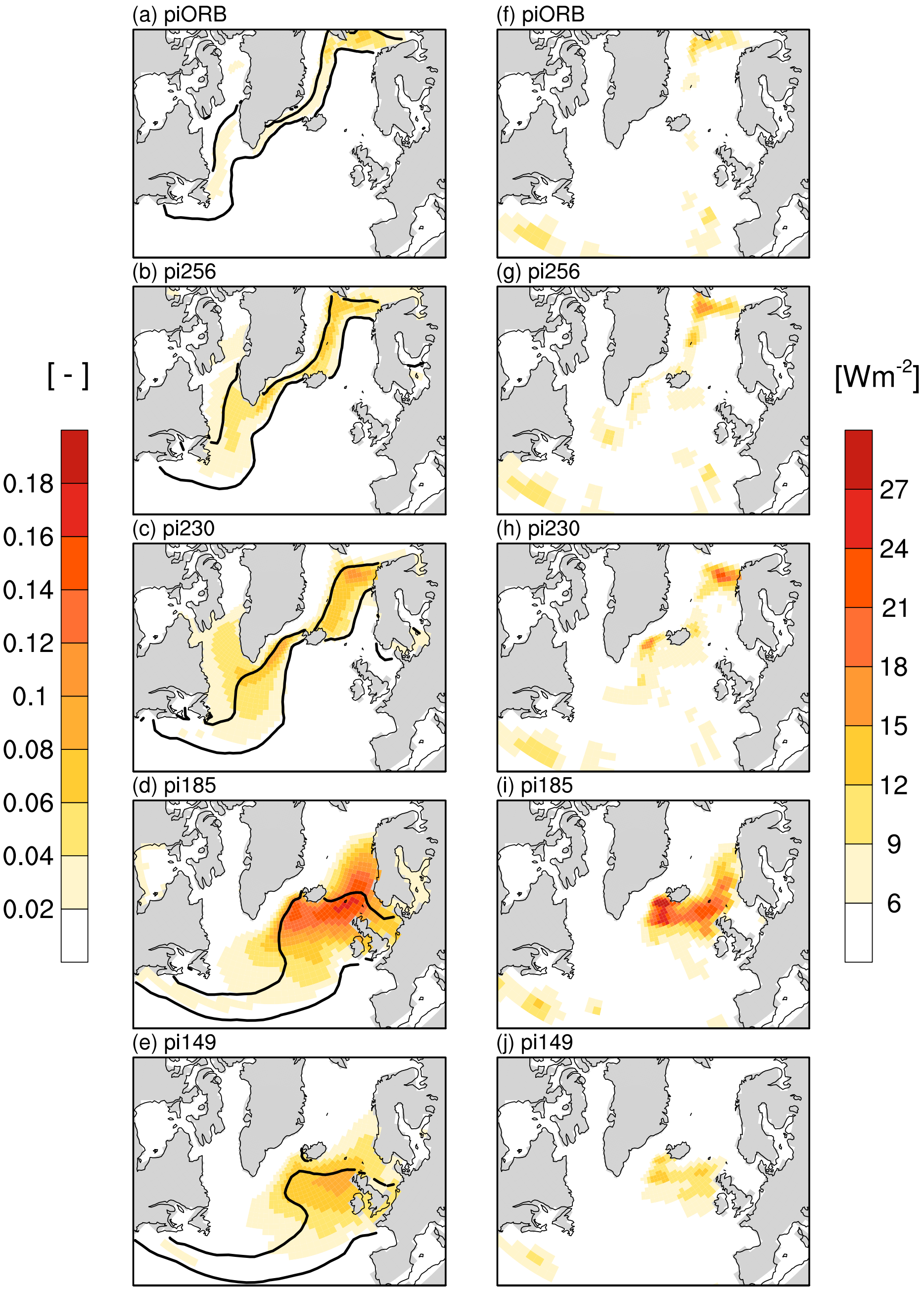

Figure 5.9: (a)-(e) Standard deviation of the 50-year mean time series for sea-ice concentration. Overlaid are the 90 % and the 10 % contours of the annual maximum sea-ice concentration from the 300-year climatologies. **(f)-(j)** Same as left column for the ocean surface heat flux. All time series have been detrended before the calculation.

- The strong AMOC mode becomes unstable at a pCO_2 between 230 ppm and 206 ppm. The weak AMOC mode becomes stable at a pCO_2 between 206 ppm and 185 ppm. The temporal variability of the AMOC and other related variables increases in the vicinity of these two thresholds.
- The simulation pi206 is located between the two thresholds, therefore the AMOC does not reach a steady state.
- Two conditions need to be fulfilled for the AMOC to operate in the weak mode: AABW needs to be sufficiently dense and saline and the Nordic Seas do not contribute to NADW formation. Instead the formation of NADW must be confined to the regions south of the Greenland-Scotland Ridge, i.e., the Irminger Sea and the Iceland Basin.
- The transition from the strong to the weak AMOC mode is qualitatively consistent with the cooling threshold identified by *Oka et al.* (2012) in their simulations with preindustrial wind-stress forcing.

Based on the sensitivity experiment pi185_brine, I conclude:

- The stability of the two AMOC modes depends on the salinity of AABW. With reduced brine release in the Southern Ocean and fresher AABW, the strong AMOC mode is stable also at 185 ppm.

6 | Transitions between the strong and the weak AMOC mode

This chapter discusses the physical mechanisms which drive the transitions between the unstable weak and strong AMOC modes in the pi206 simulation. In the first and second part of the chapter, I characterise composites of the weak and the strong AMOC phases in pi206, compare them with the other simulations of the pi*xxx* series and identify where the transitions are triggered. The characterisation of the weak and strong phases follows the analyses of the previous chapter. In the third part of the chapter, I analyse the transition periods and present a feedback loop which can explain the transitions between the two modes.

6.1 Composites of the strong and weak phases in pi206

6.1.1 Overturning

In pi206, the AMOC does not reach a stable equilibrium state. The NADW cell switches back and forth between the strong, deep mode and the weak, shallow mode. It takes about 1500 to 1700 years to complete one cycle (Fig. 5.1 b). To analyse the weak and the strong AMOC phases in pi206 separately, I calculate composites of 300-year periods in which the AMOC is weak or strong, respectively. The respective periods are marked in blue and red in Fig. 5.1 b. The first 1500 years of the simulation are considered as spin-up and therefore left out of the analysis. The years 8000 to 10000 have also not been considered in order to not corrupt the composites. The transition to the strong mode is interrupted in year 8700, which causes a weaker double event. In the following, the composite of the weak phases will be referred to as pi206_w, the composite of the strong phases will be referred to as pi206_s.

In pi206_w the NADW cell has an average strength of 7.5 Sv (light green, solid line in Fig. 5.1 a and Fig. 6.1 a), in pi206_s it has an average strength of 16.5 Sv (light

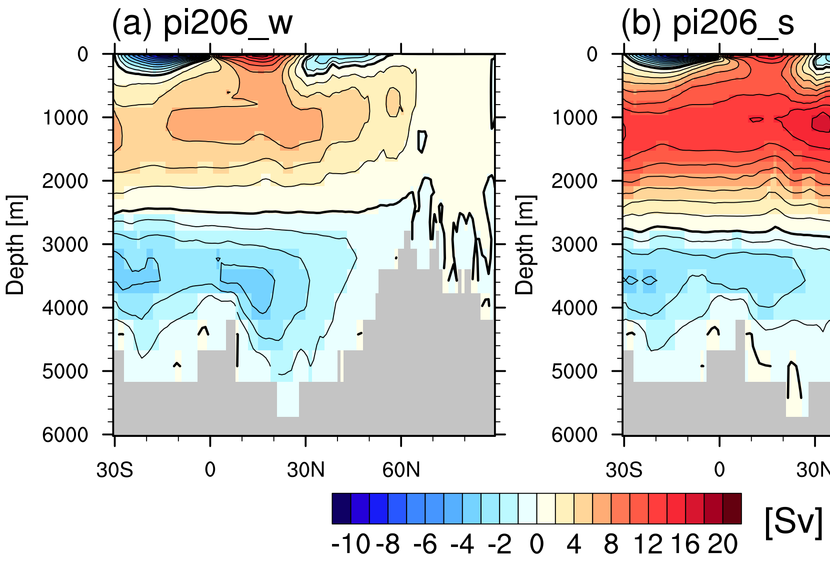

Figure 6.1: Composites of **(a)** the weak AMOC phases and **(b)** the strong AMOC phases.

green, dashed line in Fig. 5.1 a and Fig. 6.1 b). The boundary between the NADW cell and the AABW cell is located at 2500 m pi206_w and at 2900 m in pi206_s. The AMOC strength in pi206_w is 0.5 Sv stronger than in pi185. This is consistent with the AMOC decrease of 1 Sv per ΔRF in the weak AMOC mode (Ch. 5.1), as the radiative forcing difference between pi206 and pi185 is $0.5 \times \Delta RF$. The AMOC in pi206_s is, in contrast, much stronger than one could expect given the low pCO_2. Instead of switching to a state similar to the closest strong stable AMOC state in pi230, the AMOC in pi206_s overshoots. Its strength and geometry are very similar to the AMOC in piORB.

6.1.2 NADW formation

Deep convection

In pi206_w, the deep-convection sites are similar to those in pi185. The MLD patterns indicate sporadic deep convection in the Iceland Basin and over the Reykjanes Ridge (Fig. 5.2 e). The long-term mean mixed layer in pi206_w is slightly deeper than in pi185, which is consistent with the slightly stronger NADW cell in pi206_w. Deep-convection events last between 10 and 15 consecutive winters (not shown). Between the events there lie 5 to 10 years without any deep convection. In pi206_s, the deep-convection sites are similar to those in pi185_brine, with deep convection occurring continuously in the Iceland basin, the Nordic Seas and the Arctic Ocean (compare Fig. 5.2 d and Fig. 5.7 d). The deepest mixed layer is located in the Arctic Ocean, but the Arctic water is again not dense enough to contribute to the formation of NADW (not shown).

Surface density fluxes

The net density flux over the Nordic Seas is weakly negative in pi206_w (Fig. 5.3 b). The small density gain due to heat loss and brine release is outweighed by the density loss due to freshwater input. In pi206_s, the net density flux is weakly positive (open symbols in Fig. 5.3 b). During the strong AMOC phases, more heat and salt is advected into the Nordic Seas. The warm and salty water acts as a preconditioning for deep convection. The density gain due to heat loss increases with respect to pi206_w, indicating active deep convection. However, the stronger heat loss is largely compensated for by increased sea-ice melt.

Also over the North Atlantic, the net density flux is negative in pi206_w (Fig. 5.3 a). The heat-flux contribution is outweighed by the contributions from freshwater input and sea-ice melt. The net density flux is, however, still close to zero. Thus small changes in any of the three components can induce a switch from a net density loss to a net density gain and support a transition from the weak AMOC phase into the strong AMOC phase. In pi206_s, the net density flux is positive as the result of a very strong density gain due to heat loss (open symbols in Fig. 5.3 a). The heat loss in pi206_s is stronger than in any of the other pi*xxx* simulations. But also the sea-ice melt is stronger than in any of the other simulations in which the AMOC is in the strong mode, because there is more sea ice available for melting due to the colder climate. As a result, the net density gain is stronger than in pi230 but weaker than in pi256 and piORB. The surface density flux gives a first hint on why the strong AMOC mode in pi206_s is unstable. The AMOC of preindustrial strength in pi206_s cannot be sustained by a surface density gain that is considerably weaker than in piORB.

6.1.3 Water-mass properties

In the Nordic Seas, the water-mass properties in pi206_w are very similar to pi185 (Fig. 5.4). In pi206_s, salinity increases by about 0.4 g kg^{-1} and the temperature increases by 0.6 K with respect to pi206_w. The temperature increase does not represent a mean warming of the Nordic Seas but a shift in the location of the density maximum. In pi206_w, the density maximum in the Nordic Seas is located in

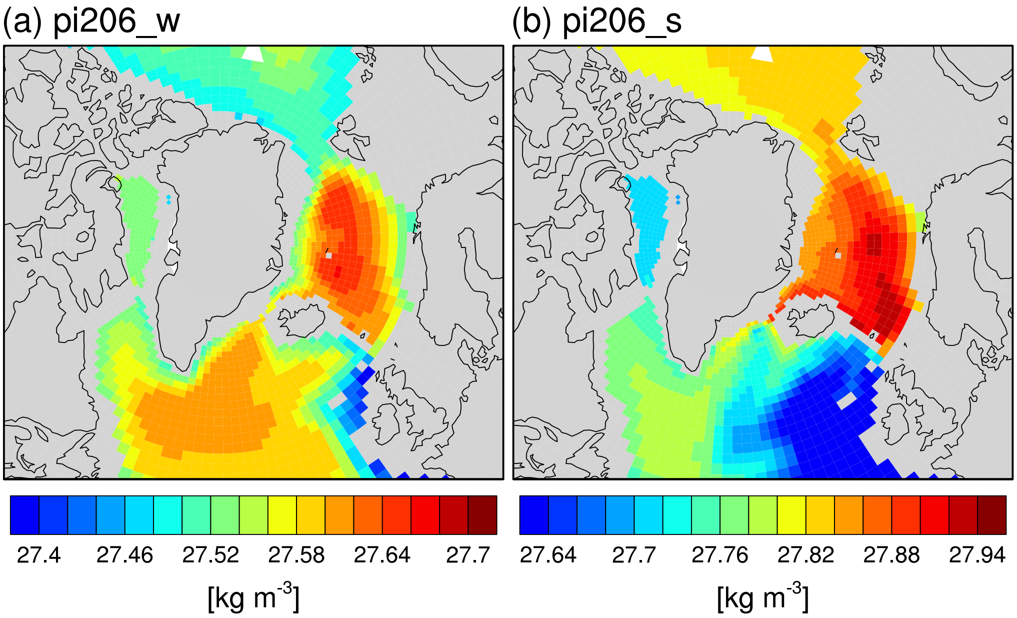

Figure 6.2: σ_Θ at 650 m in **(a)** pi206_w and **(b)** pi206_s. Note that the density range is different between the two panels.

the centre of the basin, away from the lighter and warmer water of Atlantic origin which circulates around the basin (Fig. 6.2 a). In pi206_s, on the other hand, the density maximum is located directly in the Atlantic inflow, where deep convection takes place north of the Iceland-Scotland Ridge (Fig. 6.2 b). There, the water is warmer than in the centre, despite the heat loss which occurs during deep convection. The average subsurface temperature in the Nordic Seas is lower in pi206_s than in pi206_w (see also Fig. 6.5 a). A similar average warming occurs when the AMOC switches into the weak mode during the spin-up of pi185 (not shown). This is also consistent with the Nordic Seas being warmer in pi185 than in pi230 (Fig. 5.4 c). In the weak AMOC mode, the Nordic Seas are capped by a halocline (see also Fig. 6.5 b) and covered by sea ice (Fig. 5.2 e to g), both of which insulate the subsurface waters. No heat loss occurs and the Atlantic inflow warms the layer between 100 and 700 m. Similar temperature differences have been reconstructed in the south-east Nordic Seas during the DO-cycles between 30000 and 40000 years before present (*Dokken et al.*, 2013). Colder periods over Greenland (stadials) were associated with warmer subsurface waters and increased sea-ice cover with respect to the warmer periods (interstadials).

In the North Atlantic, the water-mass properties in pi206_w are nearly indistinguishable from those in pi185. In pi206_s, salinity increases by about 0.25 g kg^{-1} with respect to pi206_w and the temperature increases by 0.5 K. The salinity increase and the warming reflect the active formation of NADW, which sustains the strong AMOC mode. In pi206_w, the water temperature is close to the freezing point and the salinity is slightly lower than in pi185. The Weddell Sea water in pi206_s freshens by 0.02 g kg^{-1} with respect to pi206_w and the temperature remains at the freezing point. The north-south salinity difference, again defined as the difference between North Atlantic salinity and Weddell Sea salinity, is about 0.04 g kg^{-1} in pi206_w and 0.29 g kg^{-1} in pi206_s. Because the salinity changes in the Weddell Sea are so small, changes in the north-south salinity difference are mostly controlled by changes in the North Atlantic salinity.

At low water temperatures, the effect of salinity on the potential density σ_Θ is larger than that of temperature. Hence, the σ_Θ changes in pi206 are to first order a function of the salinity changes. In pi206_w, the Weddell Sea water is by far the densest of the three regions (Fig. 5.4 a and b). In pi206_s, σ_Θ in the Nordic Seas increases by about 0.32 kg m^3 due to the strong salinity increase and is thus slightly higher than in the Weddell Sea. The strong AMOC in pi206_s can only be sustained as long as the North Atlantic and the Nordic Seas are salty enough to keep the σ_Θ of NADW high enough to compete with AABW.

6.2 Location of the trigger

The density changes in the Nordic Seas and North Atlantic are out of phase with the density changes in the Weddell Sea (Fig. 6.3, only the Nordic Seas and Weddell Sea are shown). The Weddell Sea water is lightest when the *increase* in Nordic Sea density is strongest, and the Weddell Sea water is densest when the *decrease* in Nordic Sea density is strongest. The density variations in the Nordic Seas are an order of magnitude larger than in the Weddell Sea (approximately 0.3 kg m^{-3} versus 0.04 kg m^{-3} peak-to-peak difference, respectively). The different magnitude of the density variations suggests that the density variations in the Weddell Sea are driven by the variations in the North Atlantic. However, the salinity signal in the North Atlantic is very likely amplified by an advective salinity feedback with the AMOC. Therefore, it cannot be straight away excluded that the small density variations in the Weddell Sea are triggering the AMOC transitions. To test the hypothesis of the Weddell Sea driving the North Atlantic, I perform the sensitivity experiment pi206_rest in which temperature and salinity in the deep South Atlantic are restored

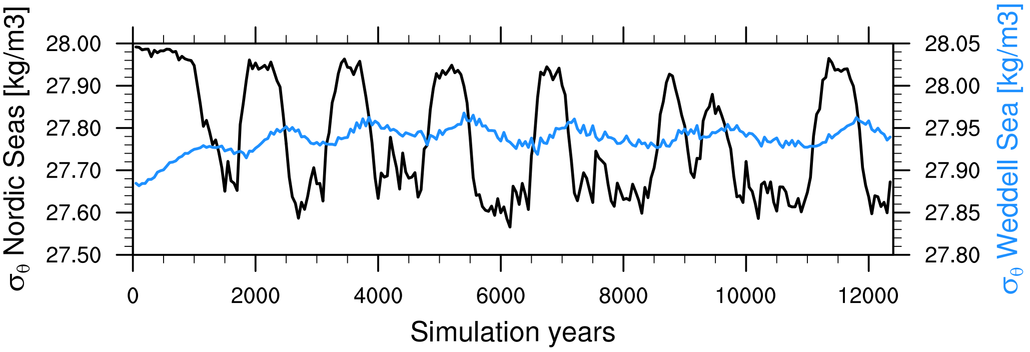

Figure 6.3: Time series of the σ_Θ in the Nordic Seas (black) and the Weddell Sea (blue) in pi206. Note that the range of the right Y-axis is half of the range of the left y-axis for a better visibility of the variability in the Weddell Sea.

to a fixed climatology. The restoring takes place across the width of the Atlantic basin below 3700 m, between 26°S and 37°S. The restoring climatology is defined as the average of a 300-year period at the beginning of a strong AMOC phase in pi206 (years 4900 to 5199, see grey bar in Fig. 6.4). In this period, the Weddell Sea water is still in its light phase. The pi206_rest simulation is branched off pi206 in year 4900 and integrated for 4000 years. The restoring prevents the northward propagation of Weddell-Sea variability. Hence, if the North Atlantic were driven by the Weddell Sea variability, the AMOC in pi206_rest should stay in the strong mode.

However, state transitions also occur in pi206_rest (see dashed line in Fig. 6.4). During the first 300 years, the AMOC stays in the strong mode and then switches into the weak mode. It stays in the weak mode for approximately 2000 years and then switches back into the strong mode where it remains for another 600 years before switching to the weak mode again. Hence, I conclude that the Weddell Sea variability is a response to the changes in the North Atlantic and not vice versa. The signal of the North Atlantic is advected to the Southern Ocean via the deep branch of the NADW cell and the phase shift corresponds to the advective timescale of the weak AMOC mode. The period during which the AMOC stays in the weak mode is longer in pi206_rest than in pi206, where the longest duration of the weak phase is 1200 years. This may suggest that the density variations in the Weddell Sea modify the time between transitions. But the integration time of pi206_rest is too short for testing this hypothesis.

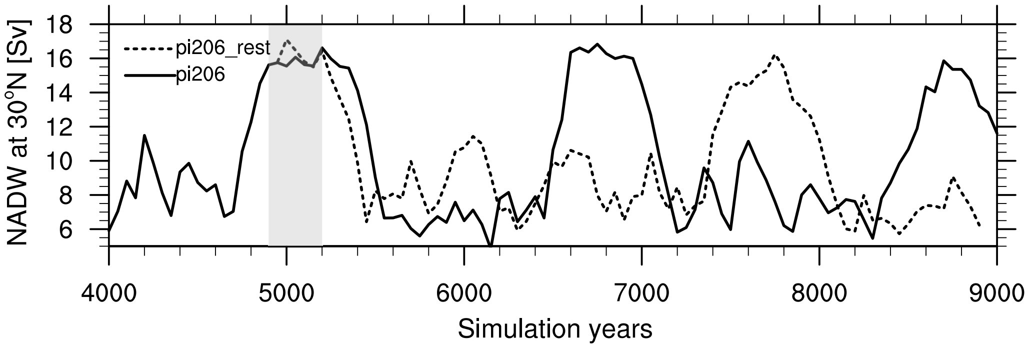

Figure 6.4: Time series of the overturning strength at 30°N in pi206 (solid) and pi206_rest (dashed).

6.3 Mechanisms behind the AMOC transitions

6.3.1 Salinity oscillations

The results of pi206_rest confirm that the trigger for the abrupt transitions in pi206 is not located in the Southern Ocean. Hence, it is very likely that the transitions are triggered by changes in the northern half of the Atlantic basin. The large salinity fluctuations in the Nordic Seas and the North Atlantic suggest that a redistribution of salt plays a crucial role in the AMOC transitions. During the weak phases, salt and heat accumulate in the upper 1000 m of the tropical Atlantic (Fig. 6.5). The salinity increases by up to 0.5 g kg^{-1} between the equator and 24°N. North of 47°N, the Atlantic and the Nordic Seas freshen by up to 0.4 g kg^{-1}. Hence, a strong salinity gradient develops between the tropical and the subpolar Atlantic during the weak AMOC phases.

The build up of such a salinity gradient was proposed as a possible mechanism to explain abrupt AMOC changes during DO-events (*Peltier and Vettoretti*, 2014; *Brown and Galbraith*, 2016). *Peltier and Vettoretti* (2014, hereafter PV14) referred to this mechanism as a *kicked salt oscillator*. During weak AMOC phases, salinity accumulated in the Atlantic south of 30°N, and a halocline formed in the subpolar North Atlantic. Once the salinity gradient exceeded a critical threshold, a strong northward salt transport set in. The supply of salty water to the North Atlantic increased the density in the deep-water formation areas and enhanced the deep convection. This led to an abrupt increase and overshoot of the overturning strength. Once the salinity gradient collapsed, the AMOC declined gradually, accompanied by sea-ice expansion. During the decline of the AMOC, the subpolar halocline was

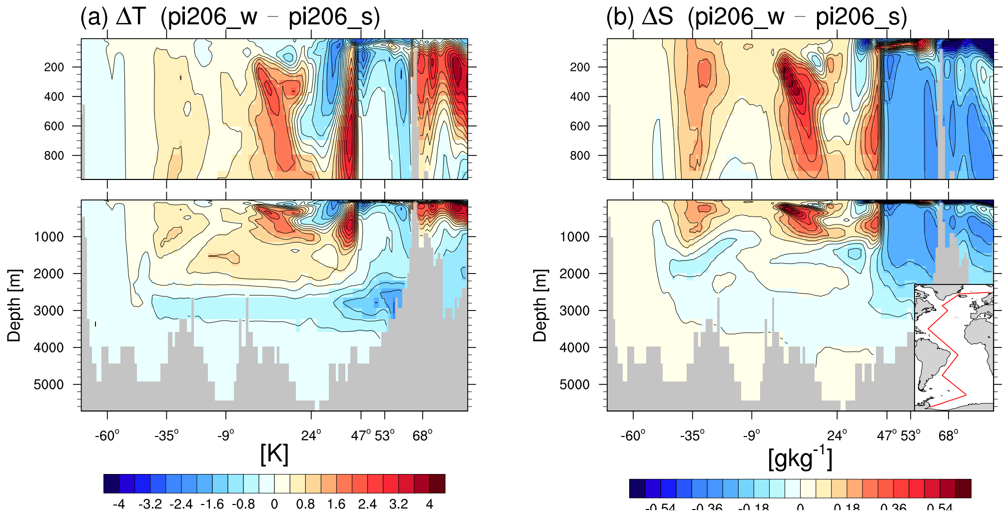

Figure 6.5: Section along the western Atlantic basin. Shown are composite differences between pi206_w and pi206_s for **(a)** temperature and **(b)** salinity. The respective upper panels show only the upper 960 m (upper 23 model levels) for a more detailed view of the upper water column. The section is shown in the map in the bottom right corner of (b).

re-established and the salinity gradient began to build up again.

The salinity changes in pi206 agree qualitatively very well with the mechanism proposed by PV14. The salt content of the subpolar North Atlantic is highly correlated with the AMOC strength with a correlation coefficient of 0.94. The high correlation confirms that the salinity-advection feedback determines the salinity of the North Atlantic. In strong AMOC phases, the salinity in the North Atlantic is high; in weak AMOC phases, the salinity is low (Fig. 6.6 a, blue line). The salt content in the tropical Atlantic is inversely correlated with the AMOC strength with a correlation coefficient of -0.74. During the transition from a strong AMOC phase to a weak AMOC phase, the salt content in the tropical Atlantic increases abruptly (Fig. 6.6 a, red line). While the AMOC remains in the weak phase, the tropical salinity increases further, albeit more slowly. The transition from a weak to a strong AMOC phase is accompanied by a strong northward salt transport (Fig. 6.6 b, blue line). The peak in the salt transport lasts for about 300 years during which the tropical salinity decreases rapidly. Once the tropical salt reservoir is exhausted, the density gain over the Nordic Seas and the North Atlantic (Fig. 5.3) is not sufficient to sustain the strong AMOC state. The transition to the weak state sets in, and the salinity in

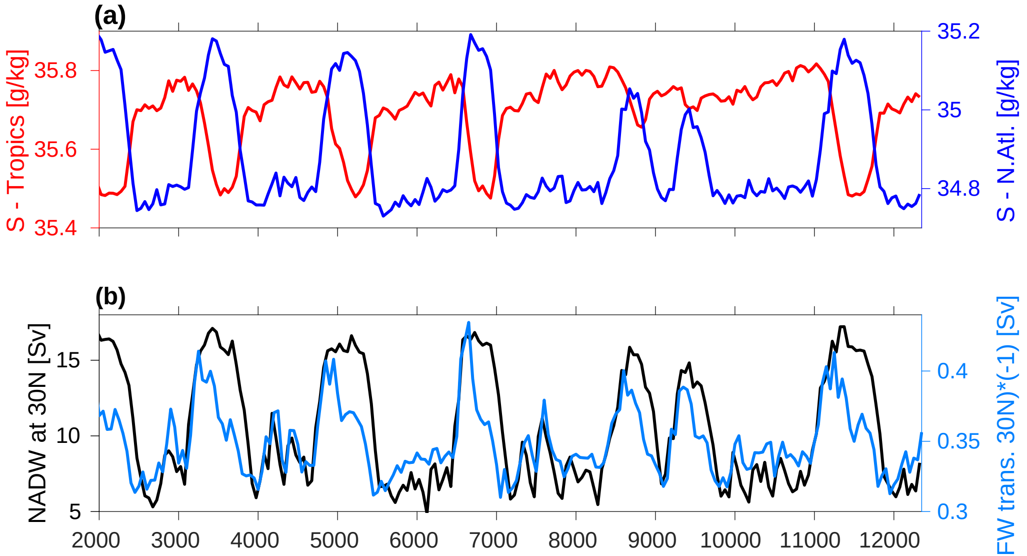

Figure 6.6: **(a)** Time series of the salt content of the upper 50 to 1000m in the tropical Atlantic (red) and in the North Atlantic (blue) in pi206. The two regions are defined as boxes on the curvilinear ocean grid. The tropical Atlantic is defined here as the Atlantic basin between approximately 8°N and 30°N. The North Atlantic box extends meridionally from 45°N to 60°N and zonally from 16°W to 44°W on the northern edge and from 8°W to 44°W on the southern edge. Note that the absolute salinity values on the left and right axes differ while the range is the same. **(b)** Time series of the freshwater transport near 30°N (light blue) and of the overturning strength at 30°N (black). The freshwater transport is calculated from the freshwater budget of the Atlantic north of 30°N (see App.A). It is multiplied by (-1) to indicate salt transport. Positive values imply a southward transport of freshwater and hence a northward transport of salt.

the tropical Atlantic begins to increase simultaneously. An increase of tropical subsurface salinities has also been reconstructed for DO-stadials (*Schmidt et al.*, 2006).

It should be noted that the length of one oscillation cycle in PV14 was about half as long as in pi206. One complete cycle in PV14 took 690 to 770 years, while it takes 1500 to 1700 years in pi206. However, the length of one cycle scales well with the strength of the AMOC. The AMOC in PV14 oscillated between 30 Sv and 12 Sv. Hence, it seems that the length of one oscillation cycle is related to the flushing time scale of the AMOC: the stronger the AMOC, the shorter one cycle.

The transition from the strong state to the weak state is gradual in PV14 but abrupt in pi206. PV14 attribute the gradual decline to the gradual expansion of the sea-ice edge and the gradual re-establishing of the subpolar halocline. However, the expansion of the sea-ice edge and the subpolar freshening can also be interpreted as a consequence of the AMOC decline rather than its cause. Instead, I would argue that the cause of the AMOC decline is the weakened northward salt transport and the resulting cessation of deep convection in the Nordic Seas. In addition to the salinity gradient between the tropical and subpolar Atlantic, circulation changes in the North Atlantic have a large impact on the northward salt transport.

6.3.2 Feedback with the SPG

Correlation between AMOC and SPG

A key component of the circulation in the North Atlantic is the SPG (represented here by the barotropic stream function). Changes in the strength and extent of the SPG play an important role in the transition from the strong to the weak AMOC state. The strength and extent of the SPG are anti-correlated with the AMOC with a correlation coefficient of -0.83. During the weak AMOC phases, the SPG has a maximum strength of 32 Sv and extends far to the east of the Atlantic basin (Fig. 6.7 a). During the strong AMOC phases, the SPG weakens by about 12 Sv with respect to the weak AMOC phases and is more contracted (Fig. 6.7 b). With a strong SPG which extends far eastwards, the North Atlantic and the Nordic Seas are dominated by relatively fresh subpolar water and only very little saline water of subtropical origin reaches the deep-convection areas in the Iceland basin and Irminger Sea. The salinity and flow field integrated over the upper 500 m illustrate this very well (Fig. 6.7 c and d). In pi206_w, the inflow of saline water from the STG is visible as a narrow band of northward flow in the salinity range of 34.7 to 34.9 $\mathrm{g\,kg^{-1}}$ off the Bay of Biscay and the Irish coast. In pi206_s, the inflow extends over the entire Atlantic basin east of the Mid-Atlantic Ridge and its salinity ranges from 34.9

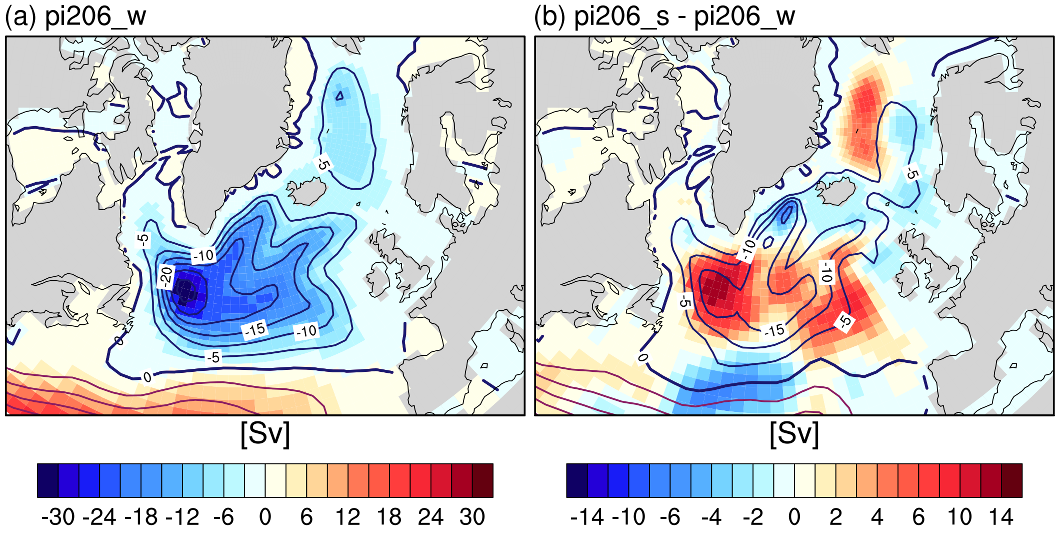

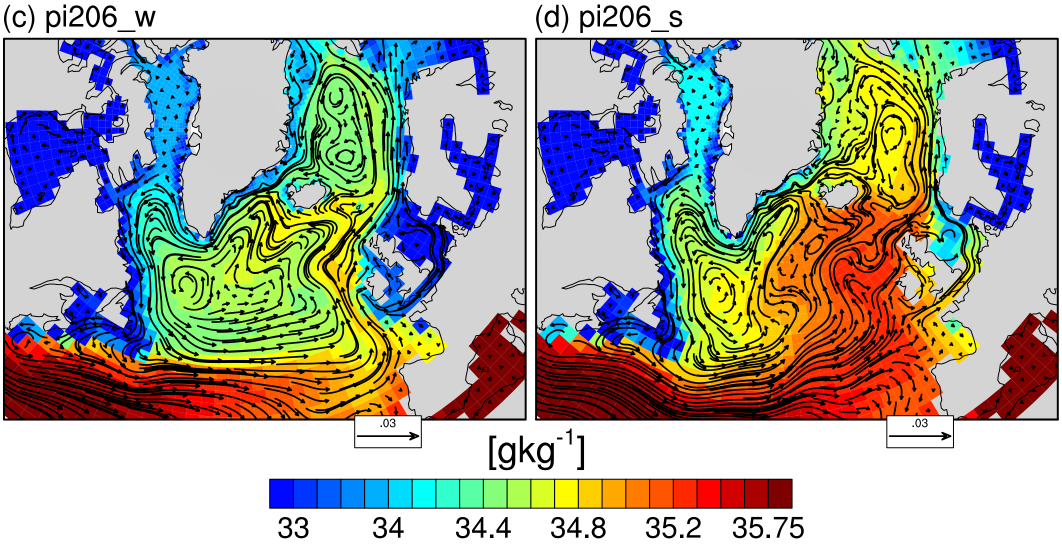

Figure 6.7: **(a)** Barotropic stream function in pi206_w. **(b)** Difference in the barotropic stream function between pi206_s and pi206_w as colour shading and the absolute stream function in pi206_s overlain as contours. **(c)** and **(d)** Salinity and horizontal velocity integrated vertically over the upper 500m in pi206_w and pi206_s, respectively.

to 35.2 g kg^{-1}. The inflow pattern in pi206_s is anomalous in the sense that it is not present in any of the other pi*xxx* simulations in which the AMOC operates in the strong mode. The anomalously strong inflow from the subtropics supplies salty water to the deep-convection areas in the Iceland basin and in the Nordic Seas and can thus explain the preindustrial strength of the AMOC during the strong AMOC phases in pi206.

To analyse the interaction between the AMOC and the SPG in more detail, I compare the temporal evolution of the SPG strength and of the AMOC strength in pi206. The SPG strength is determined as the maximum of cyclonic transport in the centre of the SPG. The sign of the transport is inverted, so that larger positive values indicate stronger cyclonic flow. The transition from a weak to a strong SPG and vice versa take place at approximately the same time as the AMOC transitions, and the time scales are similar (Fig. 6.8 a). From the 50-year averages it is, however, difficult to see whether the AMOC and SPG transitions occur simultaneously or whether one is leading the other. A time series of the first two cycles (simulation years 1500 to 4200) with yearly averages smoothed with a 15-year running mean shows that the SPG is leading the AMOC when the AMOC switches from the strong to the weak phase, and that the AMOC is leading the SPG when the AMOC switches from a weak to a strong phase (Fig. 6.8 b). The strengthening of the respective leading component appears more abrupt, while the weakening of the respective lagging component appears more gradual.

A scatter plot of SPG-transport anomalies against AMOC anomalies during the transitions phases confirms the inverse AMOC-SPG relationship (Fig. 6.8 c and d). The time periods considered for the scatter plot are marked by the red and blue bars in Fig. 6.8 a and b. The intervals are chosen based on the AMOC time series. They are centred approximately at the mid point of a transition period and extend 150 to 200 years in both directions, so that one interval is between 300 and 400 years long. The transition from the strong to the weak AMOC state (blue dots in Fig. 6.8 c and d) can be separated into two phases. During the first phase (see 1. in Fig. 6.8 c), the SPG strengthens faster than the AMOC weakens. During the second phase, the SPG has reached its strong state and the AMOC continues decreasing (see 2. in Fig. 6.8 c). The transition from the weak to the strong AMOC state (red dots in Fig. 6.8 c and d) can be split in a similar way. During the first phase of the AMOC strengthening, the AMOC increases while the SPG remains in its strong state (see 3. in Fig. 6.8 c). The SPG weakening sets in at the beginning of the second phase, when the AMOC strengthening is approximately half completed (see 4. in Fig. 6.8 c).

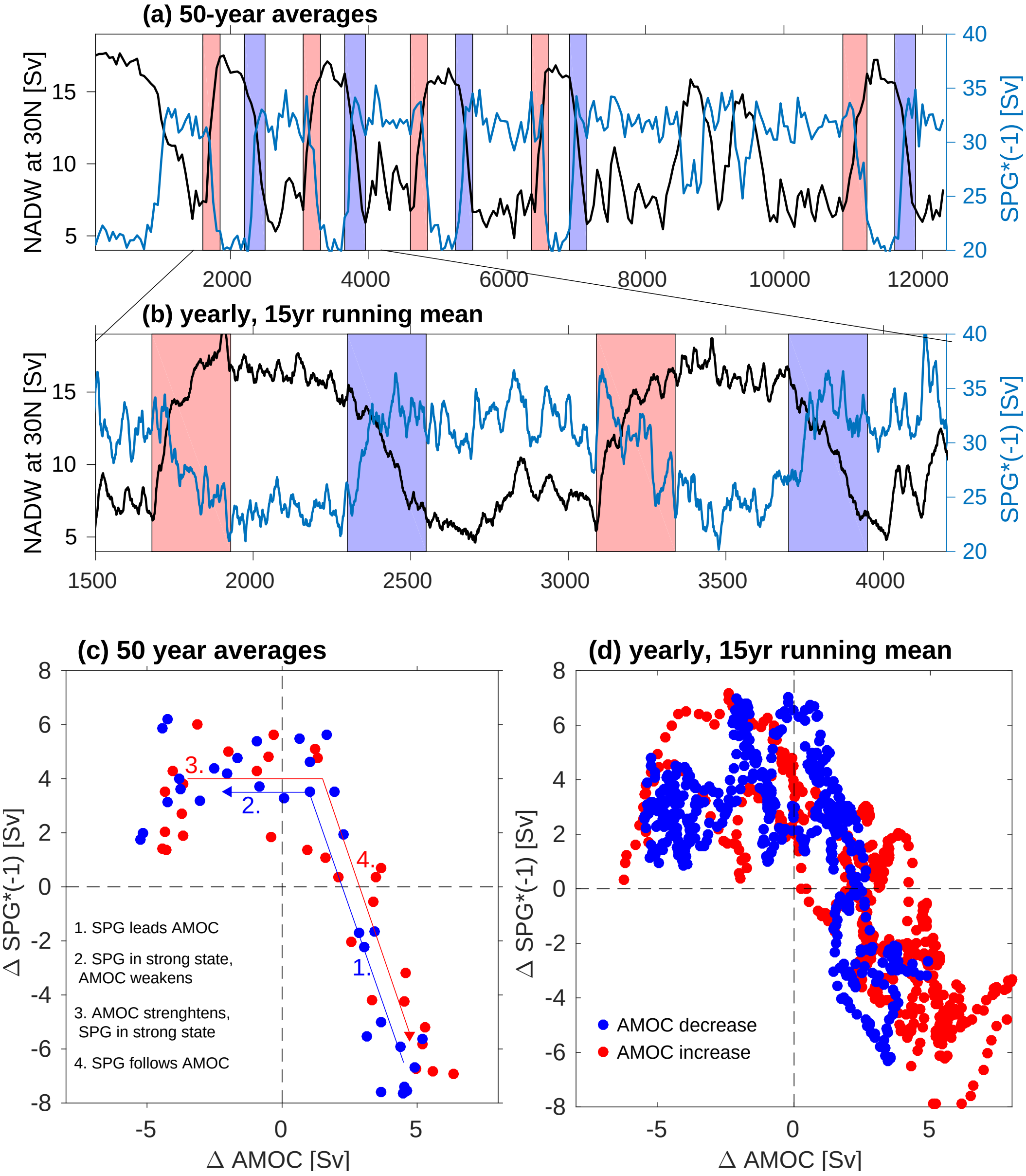

Figure 6.8: **(a)** and **(b)** Time series of the AMOC strength and the SPG strength in pi206. Shown are 50-year averages and yearly values, smoothed with a 15-year running mean. The SPG strength is determined as the spatial minimum of the barotropic stream function in the SPG region and multiplied by (-1). **(c)** and **(d)** Relationship between between AMOC strength and SPG strength during the transitions from the strong to the weak phase (blue dots) and from the weak to the strong phase (red dots). The respective time periods are marked by the red and blue bars in (a) and (b). The transports are expressed as deviations from the mean of the complete simulation. Positive anomalies indicate a strengthening. The red and blue lines in (c) are an orientation aid; they do not indicate a fit to the data.

The strengthening of the SPG and its effect on the northward salt transport provide a mechanism to trigger the transition from the strong to the weak AMOC state. Using observations and model results, *Hátún et al.* (2005) found that the strength of the SPG and the salt transport into the Nordic Seas are inversely correlated. A strong SPG circulation reduced the salinity of the inflow from the North Atlantic to the Iceland basin and the Nordic Seas, because the percentage of subtropical water in the inflow was reduced. *Hátún et al.* (2005) studied interannual SPG variability, but *Thornalley et al.* (2009) showed that the same relationship between SPG strength and inflow salinity held also on centennial to millennial timescales during the Holocene. A stronger SPG which extends further into the eastern North Atlantic reduces the amount of salty subtropical water which enters into the Iceland basin and the Nordic Seas. Hence, the strengthening and expansion of the SPG in pi206 cuts off the supply of salty water that feeds the convection in the Nordic Seas during the strong AMOC phases and thus triggers the transition into a weak AMOC phase.

The interaction between the SPG and the Denmark Strait overflow

A possible mechanism for the changes in the SPG strength is the interaction between the Denmark Strait overflow and the across-gyre density gradient. The SPG strength changed rapidly in simulations with the coarse-resolution climate model CLIMBER-3α, depending on whether or not deep-water formation took place in the Nordic Seas (*Montoya et al.*, 2011). The SPG was strong, when deep-water formation took place south of the Greenland-Scotland Ridge, and then reduced abruptly when deep-water formation became active in the Nordic Seas. The reduction in the SPG strength was attributed to the effect of the active Denmark Strait overflow on the across-gyre density gradient. The dense overflow water reduced the density gradient and hence the SPG transport. This relationship between the overflow and the SPG strength was already mentioned as an 'external feedback loop' in *Levermann and Born* (2007). A similar relationship between the Denmark Strait overflow, the AMOC and the SPG was found in a high-resolution simulation (*Zhang et al.*, 2011). An abrupt increase in the Denmark Strait overflow resulted in a strengthening and deepening of the NADW cell and a weakening and contraction of the SPG. This interaction between the SPG and deep convection in the Nordic Seas can explain the anti-correlation between the SPG and the AMOC in pi206 and also the lead-lag relationship between the two (Fig. 6.8 c and d). The strong northward salt flux at the onset of an AMOC strengthening triggers deep convection in the Nordic Seas. The overflow of dense Nordic Sea water reduces the across-gyre density gradient and the SPG weakens. In this case, the AMOC leads the SPG. Once the salt flux is not strong enough to sustain deep convection in the Nordic Seas, the overflow weakens and the SPG strengthens and expands again, reducing the salt flux into the Iceland basin further. As a consequence, the AMOC decline accelerates, led by SPG strengthening.

A crucial role of the SPG in abrupt climate transitions has also been found in previously published studies. A weakening of the SPG was found to play a crucial role in the onset of the Little Ice Age (e.g, *Copard et al.*, 2012; *Moreno-Chamarro et al.*, 2016). *Kleppin et al.* (2015) attributed an abrupt cooling event in a preindustrial control run to a weakening of the SPG. In these cases, however, the correlation between the SPG and the AMOC was positive. A reduction of the wind-stress curl and a reduction in Labrador Sea convection triggered and sustained a weak SPG. The AMOC weakened as a consequence of the reduced Labrador Sea convection. The positive correlation can be explained by the positive feedback loop described in *Levermann and Born* (2007) and *Born and Stocker* (2014). A weaker gyre would transport less salt trough eddy-salt flux into the interior of the gyre, decreasing the density at the centre of the gyre and hence reducing the across-gyre density gradient and deep convection. Reduced deep convection would reduce the heat loss at the gyre centre and weaken the density gradient further. This feedback was identified also in several CMIP3 models which featured a bistable SPG circulation (*Born et al.*, 2013).

The negative correlation between SPG and AMOC in pi206 does not necessarily imply that the positive feedback cannot be acting e.g. on shorter time scales. However, if the climate system is in a state in which deep-water formation in the Nordic Seas switches on and off on centennial time scales, then the effect of the Denmark Strait overflow on the across-gyre density gradient becomes the dominant feedback. In both *Moreno-Chamarro et al.* (2016) and *Kleppin et al.* (2015), the deep-water formation in the Nordic Seas remained largely unchanged. This corroborates the hypothesis that the deep-water formation in the Nordic Seas is the crucial tipping element in the locked AMOC-SPG transitions in pi206.

6.4 Conclusions

Based on the composites pi206_s and pi206_w, the time series of pi206 and the sensitivity experiment pi206_rest, I conclude the following:

- The AMOC transitions in pi206 are caused by a redistribution of salinity between the tropical and the subpolar Atlantic and interactions between the SPG and deep convection in the Nordic Seas.

- The switching on and off of deep convection in the Nordic Seas is crucial for the mechanism to work.
- The transition from the weak to the strong AMOC state is caused by the build-up of a salinity gradient between the tropical and the subpolar Atlantic. A sufficiently strong gradient acts as a preconditioning for enhanced NADW formation. Once a strong northward salinity transport sets in, deep convection starts in the Nordic Seas and triggers the transition from the weak to the strong AMOC state.
- The AMOC transition from the strong to the weak state is triggered by the interaction between the Denmark Strait overflow and the strength and extent of the SPG. During the strong AMOC phase, the SPG is weak and contracted, allowing for a large amount of salty subtropical water to feed the deep-convection sites in the Iceland basin and the Nordic Seas. A weakening of the overflow leads to an increase in the cross-gyre density gradient, which triggers a rapid strengthening of the SPG once the overflow is sufficiently weak. The strong subpolar gyre reduces the salt flux into the North Atlantic and thus triggers the AMOC transition into the weak state.

7 | Synthesis and discussion

The coexistence of the strong and the weak AMOC mode in a pCO_2 range somewhere between 230 ppm and 185 ppm and the instability of both modes are necessary conditions for the millennial-scale oscillations which occur in pi206. In the setup with glacial ice sheets, the AMOC strength decreases gradually but no abrupt transition to a weak AMOC mode is found. This suggests that the AMOC in the LGM*xxx* series is still far away from the bifurcation point at which the strong mode becomes unstable.

The presence of the weak AMOC mode in the preindustrial setup and its apparent absence in the glacial setup shows that the AMOC response to decreasing pCO_2 is non-linear, i.e., the GHG effect depends also on the prescribed ice sheets. This raises two related questions: First, why does the AMOC remain in the strong mode in the glacial setup? Second, are there specific conditions which favour the existence of a weak AMOC mode and abrupt AMOC transitions? I will discuss these two questions in the first half of this chapter. In the second half, I will discuss the implications of the non-linear AMOC response and the lessons that can be learned from it for the modelling of the glacial AMOC.

7.1 Dependence of the weak AMOC mode on the background climate

7.1.1 Stabilising effect of the glacial ice sheets

A first indication of why the AMOC does not switch into the weak mode in the setup with glacial ice sheets is the AMOC strength itself. A weak AMOC with reduced heat transport and weaker thermal forcing was found to be inherently less stable than a strong and thermally dominated AMOC (e.g. *Tziperman*, 2000; *Arzel et al.*, 2012). In the LGM*xxx* series, the AMOC is stronger than in all simulations of the pi*xxx* series. Even the weakest AMOC in the LGM*xxx* series (18 Sv in LGM149) is still stronger than the strongest AMOC in the pi*xxx* series (16 Sv in piORB). The bifurcation could thus be linked to a critical AMOC strength. If the AMOC is weaker than this critical value, continuous deep-water formation in the North Atlantic cannot be sustained and the strong AMOC mode becomes unstable. According to the pi*xxx* series, this critical AMOC strength would be slightly weaker than 13 Sv. With a strength of approximately 18 Sv, the AMOC in LGM149 is still very far away from this critical point.

Comparing the NADW formation in the LGM*xxx* and pi*xxx* simulations can help explaining why the AMOC is so much stronger with glacial ice sheets. While continuous deep convection in the North Atlantic cannot be sustained in pi185 and pi149, there is still active and frequent deep convection in LGMref and LGM149 in the central and eastern North Atlantic (see Fig. 4.3 and Fig. 5.2). The density gain due to heat loss over the North Atlantic and Labrador Sea is much stronger in all LGM*xxx* simulations than in the respective pi*xxx* simulations (compare Fig. 7.1 a and Fig. 5.3 a). The heat loss is strong enough to outweigh the freshwater input and sea-ice melt also at low pCO_2. There is a net density gain in all LGM*xxx* simulations. In LGM149, the net density gain is still only slightly weaker than in piORB. In the Nordic Seas, the net density flux in the glacial setup becomes zero at 230 ppm, just like in the preindustrial setup (Fig. 7.1 b). It appears that the Nordic Seas are a tipping element in the pi*xxx* simulations but not in the LGM*xxx* simulations. The glacial ice sheets keep the density gain over the North Atlantic strong enough to sustain a strong AMOC also when the Nordic Seas do not contribute to NADW formation anymore. This is consistent with the results of *Ganopolski and Rahmstorf* (2001) who found that the shape of the AMOC hysteresis under freshwater forcing differed between modern and glacial climate conditions. Under modern conditions, the AMOC switched into an off-mode when a certain freshwater input was exceeded. Under glacial conditions, however, the AMOC weakened gradually without switching into the off-mode. The authors attributed this difference to the fact that the AMOC was less sensitive to a shut-down of deep-water formation in the Nordic Seas under glacial conditions.

The ice-sheets increase the density gain over the North Atlantic in two ways. First, the katabatic winds which come down from the Laurentide ice sheet carry very cold air to the open ocean in the Labrador Sea and central North Atlantic. The resulting large air-sea temperature differences enhance heat loss and deep convection. Second, the wind-stress changes induced by the glacial ice sheets cause a northward shift of the STG, the SPG contracts, and more warm and salty subtrop-

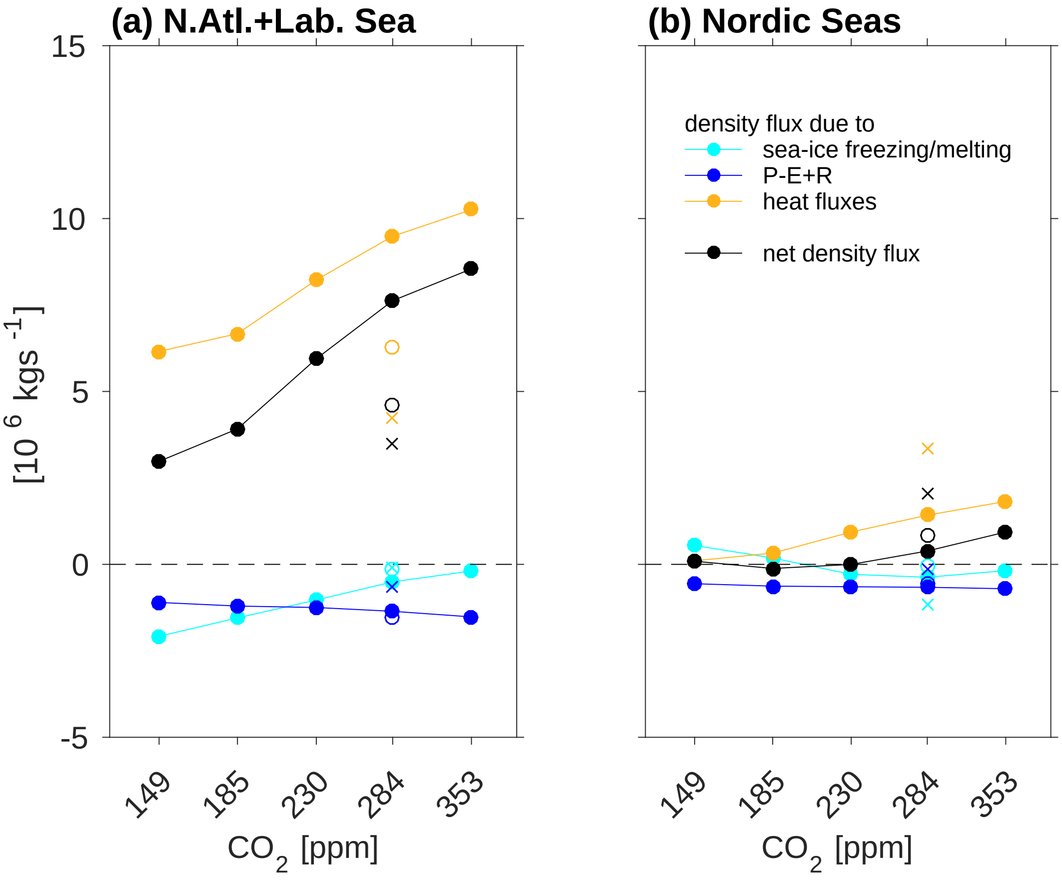

Figure 7.1: As Fig. 5.3 but for the LGM*xxx* simulations: Annual-mean density flux as a function of pCO_2, and its components. The fluxes are integrated over the OOC$_{max}$ region of **(a)** the North Atlantic including the Labrador Sea, and **(b)** the Nordic Seas. Positive values indicate a density gain, negative values indicate a density loss. The open circles indicate the LGM284_glac simulation. Note that the range of the y-axis is three times that of Fig. 5.3. For comparison, the flux components in piORB are inserted as crosses. The x-axis is scaled logarithmically.

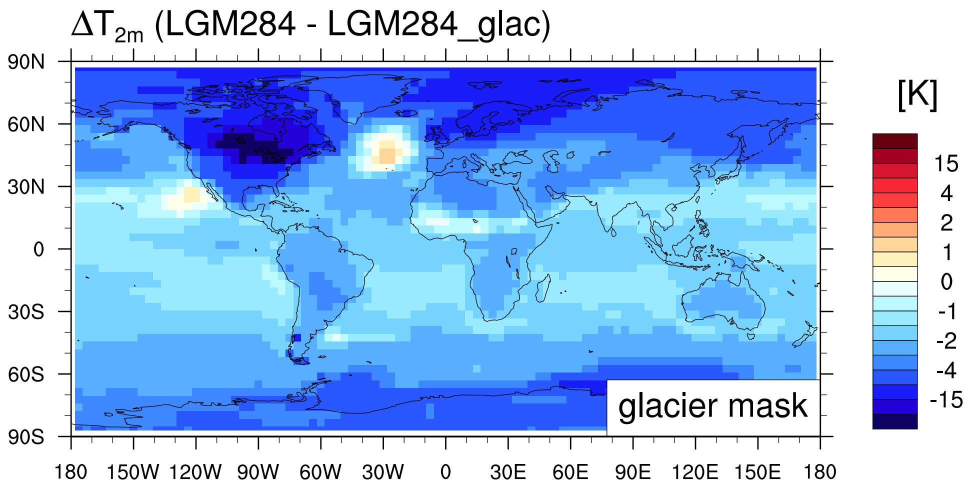

Figure 7.2: The difference in 2 m air temperature induced by the LGM glacier mask (LGM284 – LGM284_glac).

ical water reaches the deep convection sites in the Iceland basin and the Irminger Sea (as was described in Ch. 3.2).

A sensitivity experiment with preindustrial glacier mask and all other forcings identical to LGM284 (see LGM284_glac in Tab. 2.3) shows that the glacier mask can account for both of these effects. The LGM glacier mask is responsible for a large-scale cooling in the northern hemisphere and the high latitudes of the southern hemisphere (Fig. 7.2). The cooling of the northern hemisphere is a direct consequence of the ice-sheet albedo. The cooling of the southern hemisphere is a result of an increased northward heat transport in LGM284 with respect to LGM284_glac. At 25°S, the oceanic heat transport in LGM284 is about 0.25 PW stronger than in LGM284_glac. Additional cooling on both hemispheres is caused by a more extensive sea-ice cover, especially in the respective summer season. The tropical cooling in response to the glacier mask is stronger than the cooling in response to the entire ice sheet (compare Fig. 7.2 and Fig. 3.1 d). In the total ice-sheet effect, the effect of the lower sea level compensates for some of the tropical cooling in response to the glacier mask (Supp.Fig. B.1). Due to the stronger cooling over the North Atlantic, the deep-water formation in the Labrador Sea, Irminger Sea and Iceland basin is stronger in LGM284 than in LGM284_glac (compare Fig. 7.3 c and Fig. 4.3 a). As a result, the NADW cell in LGM284 is about 8 Sv stronger and 500 m deeper than in LGM284_glac (Fig. 7.3 b).

The LGM glacier mask also accounts for the shift in the STG-SPG system and the resulting enhanced northward salt transport. In LGM284_glac, the maximum SPG

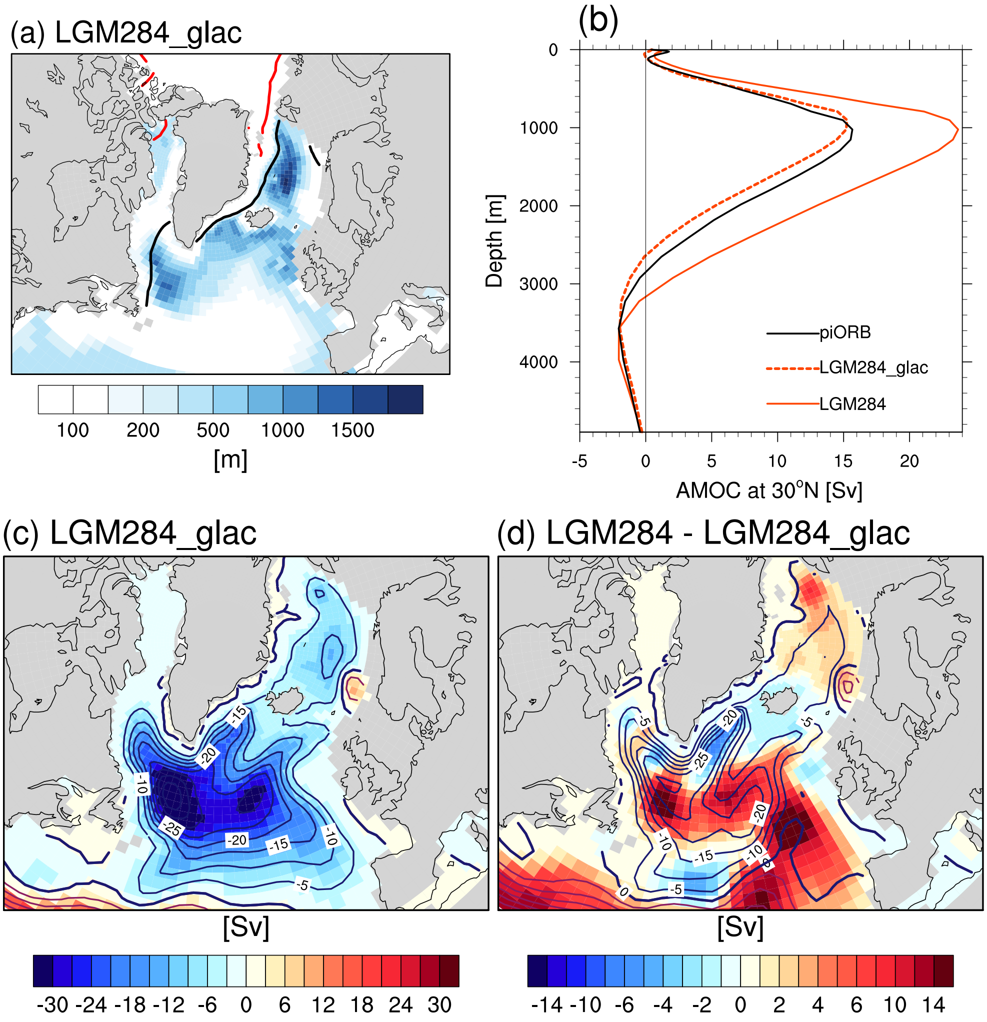

Figure 7.3: Effects of the LGM glacier mask: **(a)** Mixed layer depth and sea-ice edge in LGM284_glac. **(b)** Profile of the AMOC strength at 30°N in LGM284 and LGM284_glac. piORB is shown for comparison. **(c)** Barotropic stream function in LGM284_glac and **(d)** difference in the barotropic stream function between LGM284 and LGM284_glac (shading). The contours indicate the absolute barotropic stream function in LGM284.

transport is approximately 35 Sv at the centre of the gyre (Fig. 7.3 c). The SPG extends over the entire North Atlantic basin, blocking inflow of salty subtropical water to the deep-convection sites in the Iceland basin and Irminger Sea. The shape and extent of the SPG in LGM284_glac are similar to the SPG in piORB. This suggests that the ice-sheet topography only plays a minor role for the SPG circulation. The effect of the glacier mask is dominant, at least at high pCO_2. In LGM284, the SPG contracts and the transport is reduced by about 10 to 15 Sv with respect to LGM_glac (Fig. 7.3 d). The contraction of the SPG in LGM284 is very likely wind-driven. The wind-stress change induced by the LGM glacier mask (Supp. Fig. B.2 d) pushes the Gulf Stream northwards. The same wind-stress changes also favour the upwelling of salty subsurface water off the Bay of Biscay and the Irish Coast, as described in Ch. 3.2. A similar relationship between the northward salt transport, North Atlantic wind stress and the glacial overturning strength was described by *Muglia and Schmittner* (2015).

The results of the sensitivity experiment LGM284_glac confirm that the glacial overturning is more sensitive to the deep convection south of the Greenland-Scotland Ridge than to deep convection in the Nordic Seas. Deep convection in the Nordic Seas increases with respect to LGM284. But this increase is not enough to compensate for the reduced deep convection in the Labrador Sea and Irminger Basin. The simulation also confirms that the increased northward salt transport into the deep-convection sites of the North Atlantic and the stronger atmospheric cooling are the most important parts of the ice-sheet effect for the overturning strength. The enhanced northward salt transport counteracts the GHG effect and prevents the AMOC from switching into a weak mode. The SPG remains in its contracted form in all LGM*xxx* simulations (Supp. Fig. B.3), enabling an enhanced northward salt transport also at low pCO_2.

7.1.2 Conditions which favour abrupt AMOC transitions

Abrupt AMOC transitions have received a lot of attention in the attempt to identify the mechanism for DO-events. While the mechanism behind DO-events is beyond the scope of this thesis, these studies provide an ensemble of simulations against which pi206 can be compared in terms of the conditions under which self-sustained AMOC oscillations or stable weak AMOC modes can occur.

There is some evidence that low obliquity favours abrupt AMOC oscillations (e.g., *Friedrich et al.*, 2010; *Brown and Galbraith*, 2016). *Friedrich et al.* (2010) find internally generated oscillations in LOVECLIM in a setup with modern bathymetry and obliquity set to either 22.1° or 22.4°. They attributed the oscillations to stochastic excitations of Nordic Sea deep convection and sea-ice anomalies. Under low obliquity forcing, the sea-ice anomalies were more likely to persist long enough to affect deep convection and the overturning. *Brown and Galbraith* (2016) found that AMOC oscillations occurred at low obliquity in combination with preindustrial ice sheets and low GHG concentrations. No oscillations occurred for the same GHG concentrations and ice sheets with high obliquity. In pi206 and PV14, however, the oscillations occur with a LGM orbit where the obliquity is higher. In these cases, the ice-sheet or GHG forcing must be more important.

AMOC oscillations or abrupt state transitions have been found both in the presence of full LGM ice sheets (*Peltier and Vettoretti*, 2014; *Arzel et al.*, 2012; *Wang and Mysak*, 2006) and preindustrial ice sheets (e.g., *Friedrich et al.*, 2010; *Brown and Galbraith*, 2016). *Brown and Galbraith* (2016) found that full LGM ice sheets increased the overturning strength and prevented AMOC oscillations at low GHG concentrations. This agrees well with the ice-sheet effect in MPI-ESM and also with the dependence of the AMOC response to decreasing GHG concentrations on the prescribed ice sheets. Simulations with transient ice sheets indicate a positive relationship between ice-sheet volume and AMOC strength (*Zhang et al.*, 2014; *Zhu et al.*, 2014). Larger ice sheets induce a stronger overturning. There is, however, no consensus on whether a linear ice-sheet decrease induces a linear AMOC weakening (*Zhu et al.*, 2014) or an abrupt switch once a critical ice-sheet height is reached (*Zhang et al.*, 2014).

There seems to be a consensus that low GHG concentrations favour the existence of a weak AMOC mode and abrupt state transitions. *Brown and Galbraith* (2016) found millennial-scale AMOC oscillations at 180 ppm, a stable weak state for lower pCO_2 and a stable strong state for higher pCO_2. In simulations with transient pCO_2, *Zhang et al.* (2014) find an abrupt AMOC strengthening of about 10 Sv when the pCO_2 exceeds 200 ppm. *Wang and Mysak* (2006) find oscillations in the pCO_2 range of 190 to 220 ppm. Based on these previous studies, the pCO_2 range in which abrupt AMOC transitions or oscillations are likely to occur can be narrowed down to 180 to 220 ppm, which is in good agreement with the pCO_2 range in which neither the strong nor the weak AMOC mode are stable in the pi*xxx* series.

The existence of the weak AMOC mode in the pi*xxx* series agrees very well with the results of the HT-CTL series by *Oka et al.* (2012) in which their ocean model was forced with preindustrial surface wind stress. The two AMOC modes in the pi*xxx* experiments confirm that a similar threshold in atmospheric cooling controls the

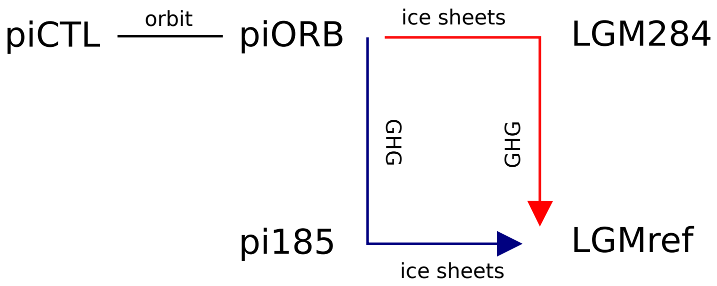

Figure 7.4: Schematic decomposition of the full glacial response into the effects of orbit, ice sheets and GHG concentrations. The decomposition in Ch. 3.2 follows the red arrow. If the AMOC response was linear, both ways of decomposing the total effect should give the same result.

AMOC state in MPI-ESM in the absence of glacial ice sheets. The key difference between the pi*xxx* and LGM*xxx* series is the enhanced northward salt transport induced by the ice sheets or - more precisely - the glacier mask, which keeps the AMOC in the strong mode. The stabilising effect of the ice sheets due to the enhanced salt transport may be very sensitive to the simulated wind-stress changes. The wind-stress changes can be very model dependent. Even the same ice-sheet reconstruction can result in a very different representation of the ice sheet in individual models because of differences in the implementation (*Chavaillaz et al.*, 2013). This could explain why weak AMOC modes have been found in the presence of both glacial and preindustrial ice sheets.

7.2 Implications and lessons learned for simulating the glacial AMOC

A key result of the decomposition of the total AMOC response into the contributions of orbit, ice sheets and GHG concentrations is that the glacial AMOC in MPI-ESM does not shoal with respect to the preindustrial AMOC because the ice-sheet effect and the GHG effect partially compensate for one another in the deep ocean (Ch. 3.2). This decomposition works under the assumption that the total response is the linear combination of the individual responses. If this assumption were true, the GHG effect would have to be identical with glacial and with preindustrial ice sheets, and the ice-sheet effect would have to be identical at 284 ppm and at 185 ppm

Table 7.1: Ice-sheet and GHG effect for the two decomposition pathways outlined in Fig. 7.4. The penultimate row lists the change of the NADW cell strength. The bottom row lists the change of the NADW cell depth. Positive values indicate a strengthening/deepening; negative values indicate a weakening/shoaling.

Ice-sheet effect		GHG effect	
at 284 pmm	at 185 ppm	21 ka ice sheets	0 ka ice sheets
LGM284–piORB	LGMref–pi185	LGMref–LGM284	pi185–piORB
+8 Sv	+13 Sv	-4 Sv	-9 Sv
+300 m	+350 m	-300 m	-350 m

(see Fig. 7.4). Because of the existence of the weak AMOC mode in the pi*xxx* simulations, the assumption of linearity needs to be treated with caution. The GHG effect on the NADW strength is much stronger with preindustrial ice sheets, and consequently, the ice-sheet effect is stronger at 185 ppm (Tab. 7.1 and Fig. 7.5).

Shoaling of the NADW cell occurs with both ice-sheet configurations. It is therefore mostly the overturning strength which is affected by the non-linear AMOC response. Combining the ice-sheet effect at 284 ppm (first column in Tab. 7.1) and the GHG effect with preindustrial ice sheets (fourth column in Tab. 7.1) would yield a glacial AMOC which is 1 Sv weaker than the preindustrial AMOC (the orbital effect is considered as negligible in this approximation). On the other hand, combining the ice-sheet effect at 185 ppm (second column in Tab. 7.1) and the GHG effect with glacial ice sheets (third column in Tab. 7.1) would yield a glacial AMOC which is 9 Sv stronger than the preindustrial AMOC. But in both cases, there would still be hardly any change in the NADW-cell depth. The NADW cell would only shoal or deepen by 50 m, respectively. This corroborates the conclusion that the lack of shoaling of the glacial AMOC is due to the partial compensation of the ice-sheet and GHG effect.

The complete ensemble of the LGM*xxx* and the pi*xxx* simulations provides two more estimates of the ice-sheet effect (Fig. 7.5). At 230 ppm, the ice sheets induce a strengthening of 9 Sv and a deepening of 350 m. At 149 ppm, the ice sheets induce a strengthening of 12 Sv and a deepening of 200 m. Hence, the sign of the ice-sheet effect is very consistent across the different pCO_2, but its magnitude depends on the background climate. A colder climate produces a stronger ice-sheet effect because the AMOC operates in the weak mode in the preindustrial setup. The same holds for the GHG effect. A GHG reduction results in a weakening and shoaling in all cases where the pCO_2 is 284 ppm and below, but the magnitude of the response depends on the prescribed ice sheets and the pCO_2 itself.

In summary, the response to the combined glacial forcings is the relatively small sum of two larger opposing effects. Small changes in either of the two effects can result in sign changes of the total response. This provides an attractive explanation for the AMOC spread in the PMIP2 and PMIP3 ensembles. The spread may be further increased because the ice-sheet effect is so different between different models. In the upcoming fourth PMIP phase, the modelling groups will have a choice between different ice-sheet reconstructions (*Kageyama et al.*, 2016, in review). Comparing the northward salt transport for different ice-sheet reconstructions may also increase the understanding of the simulated glacial AMOC. A better understanding of the glacial wind stress will help to improve the ice-sheet effect in the models. In order to improve the simulation of the GHG effect, the representation of AABW and shelf convection in the Southern Ocean needs to be improved.

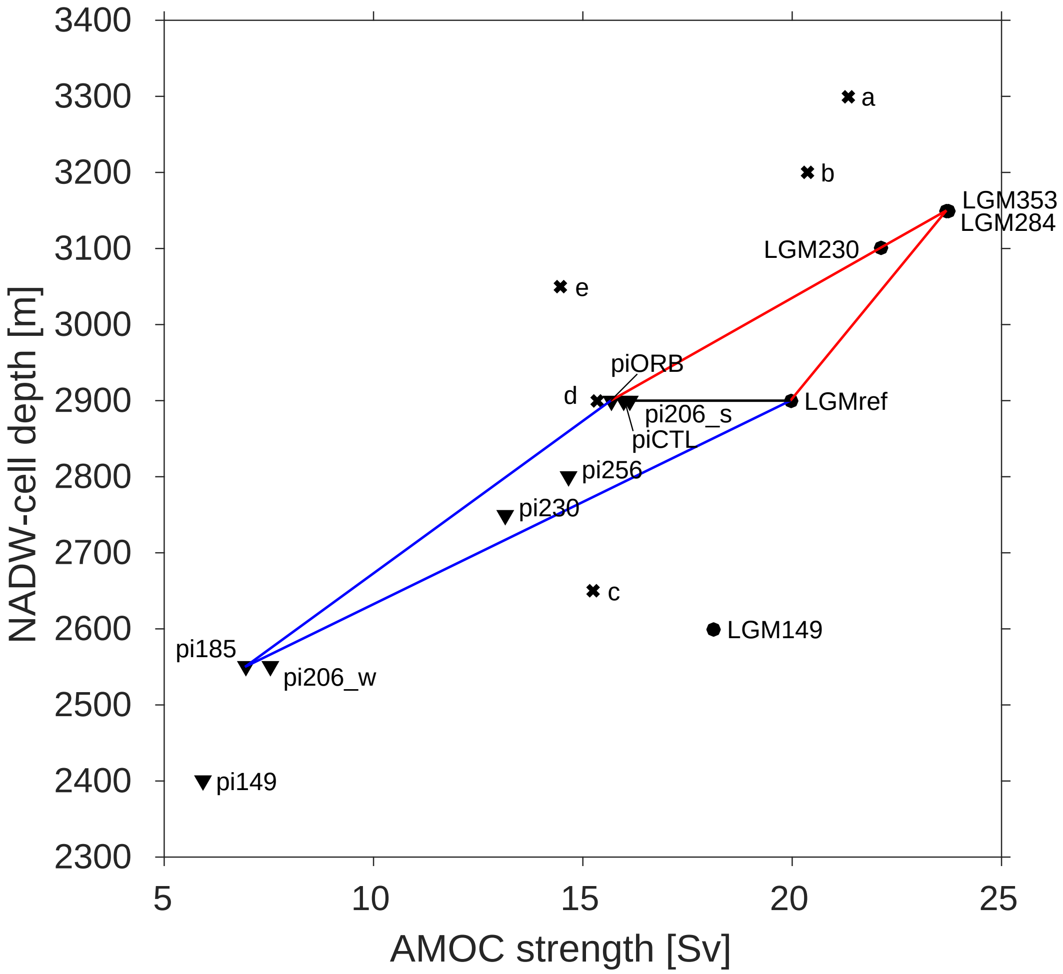

Figure 7.5: Scatter plot of NADW-cell depth against AMOC strength for all simulations. The LGM-*nnn* simulations are indicated by filled circles, the pi-*nnn* simulations are indicated by triangles. The sensitivity experiments are indicated by crosses and labelled with single letters, a:LGMref_brine, b:LGM149_brine, c:LGM284_glac, d:piORB_brine, e:pi185_brine. The black line connecting piCTL and LGMref indicates the total glacial AMOC response. The red and blue lines indicate the decomposition of the total response into the contributions from ice sheets and GHG concentrations in analogy to Fig. 7.4.

8 | Conclusions

The goal of this thesis was to analyse the sensitivity of the AMOC to different forcing combinations in the range of glacial to modern conditions and to identify the mechanisms which determine the AMOC response. To this end, I performed a preindustrial and an LGM reference simulation, a preindustrial simulation with glacial orbit, and two simulation series with different GHG concentrations and either preindustrial or glacial ice sheets. Within the respective simulation series, the GHG concentrations were decreased from modern to lower than glacial values with linearly decreasing radiative forcing. Based on this set of simulations, the questions posed in Ch. 1.4 can be answered as follows:

1. *How do the individual glacial forcings affect the AMOC and the deep Atlantic water masses?*

   The glacial orbital configuration has a negligible effect on the AMOC and on the properties of NADW and AABW due to its very small effect on the mean surface climate. The glacial ice sheets cause a strengthening and deepening of the NADW cell. The formation of NADW is enhanced through a shift in the subtropical-subpolar gyre system. The subpolar gyre contracts and the subtropical gyre shifts northward. This enhances the salt transport into the formation areas of NADW. As a consequence, NADW becomes more saline and replaces AABW in the deep North Atlantic. The glacial GHG concentrations cause a weakening and shoaling of the NADW cell. NADW freshens, possibly due to increased sea-ice melt in the deep-convection areas. With glacial GHG concentrations, the water in the Nordic Seas is not dense enough to contribute to the formation of NADW. Instead, NADW is formed primarily in the Irminger Sea and Iceland basin. AABW becomes more saline due to enhanced sea-ice formation in the Southern Ocean. The denser AABW replaces NADW in the deep North Atlantic.

   The effects of the glacial ice sheets and the glacial GHG concentrations partially compensate for one another in the deep Atlantic. Therefore, the simulated glacial NADW cell does not shoal with respect to the preindustrial NADW cell, which is inconsistent with reconstructions.

The respective sign of the ice-sheet effect and the GHG effect is robust over different background climates, but their respective magnitude depends on the forcing combination. This is due to the weak AMOC mode which occurs in the simulations with low GHG concentrations and preindustrial ice sheets. The ice-sheet effect is stronger at glacial GHG concentrations than at preindustrial GHG concentrations. And the GHG effect is stronger with preindustrial ice sheets than with glacial ice sheets. The partial compensation of the two effects in the deep Atlantic remains a robust feature; it occurs regardless of the forcing combination.

2. *How does the AMOC respond to different GHG concentrations in the presence of glacial ice sheets and in the presence of preindustrial ice sheets, and which mechanisms drive the response?*

   The AMOC response to different GHG concentrations with decreasing radiative forcing is non-linear. It depends on the absolute GHG concentrations and on the prescribed ice sheets.

   In the simulations with glacial ice sheets, the NADW cell weakens almost linearly with decreasing radiative forcing if the pCO_2 is lower than 284 ppm. The shoaling of the NADW cell only sets in if the pCO_2 is lower than 230 ppm. Below 230 ppm, the driving mechanism of AABW formation switches from heat loss to brine release. As a consequence, the salinity of AABW increases and AABW becomes dense enough to replace NADW in the deep North Atlantic. To simulate a shoaling of the NADW cell with respect to the preindustrial AMOC state, the pCO_2 needs to be lower than the glacial values of 185 ppm. At 149 ppm, the brine release in the Southern Ocean is strong enough to make AABW more salty than NADW, and the NADW cell becomes shallower than in the preindustrial control simulation. This state is consistent with the glacial cold mode, which was indicated by reconstructions of the AMOC based on εNd and Pa/Th.

   In the simulations with preindustrial ice sheets, two distinct AMOC modes occur. The first mode is characterised by a strong and deep NADW cell, while the second mode is characterised by a weak and shallow NADW cell. In the studied pCO_2 range, the strong AMOC mode is stable above a pCO_2 between

230 and 206 ppm. Below this first threshold, the strong mode is unstable. The weak AMOC mode is unstable above a pCO_2 between 206 and 185 ppm. Below this second threshold, the weak mode is stable. In between the two thresholds, both modes are unstable and the AMOC oscillates between the two unstable states on millennial timescales. Two conditions need to be fulfilled for the weak AMOC mode to be stable. First, AABW needs to be as salty as or saltier than NADW. Second, the water in the Nordic Seas must be too light to contribute to the formation of NADW. Instead, NADW is formed sporadically in the Irminger Sea and the Iceland basin.

The strong AMOC mode in the simulations with preindustrial ice sheets becomes unstable when the AMOC reaches a critical strength of approximately 13 Sv. In the simulations with glacial ice sheets, the AMOC is far away from this bifurcation point, the weakest AMOC being 18 Sv at 149 ppm. Therefore, the AMOC remains in the strong AMOC mode in all simulations with glacial ice sheets, even at very low GHG concentrations. The glacial ice sheets keep the AMOC strong by increasing the formation of NADW through an enhanced density gain at the surface of the North Atlantic. The cold winds which come down from the Laurentide ice sheet lead to a strong heat loss over the deep-convection sites of the North Atlantic. The formation of very dense water is favoured additionally by a strong salt transport into the deep-convection sites. As a result of the strong density gain over the North Atlantic, the AMOC strength in the simulations with glacial ice sheets is less sensitive to deep-water formation in the Nordic Seas. In the simulations with preindustrial ice sheets, the density gain over the North Atlantic is much smaller and deep-water formation in the Nordic Seas is a key tipping element in the transition from the strong to the weak AMOC mode.

3. *Does a similar cooling threshold as described by Oka et al. (2012) control the AMOC state in MPI-ESM?*

   The existence of the two AMOC modes in the simulations with the preindustrial ice sheets indicates that a similar cooling threshold can cause the transition from a strong AMOC mode to a weak AMOC mode in MPI-ESM. As described above, the mode transition takes place in two steps: First, the strong AMOC mode becomes unstable in the pCO_2 range of 230 ppm to 206 ppm. Second, the weak AMOC mode becomes stable in the pCO_2 range of 206 ppm to 185 ppm. The first pCO_2 threshold corresponds to a radiative forcing decrease of 50% to 75% with respect to the preindustrial GHG concentrations.

In their simulations with preindustrial wind-stress forcing, *Oka et al.* (2012) found that the AMOC switched into a weak mode when the glacial contribution to the heat-flux forcing was approximately 60%. Hence, the threshold determined by *Oka et al.* (2012) agrees quite well with the location of the first threshold in my simulations with the preindustrial ice sheets. In my simulations with the glacial ice sheets, the AMOC is much stronger than with preindustrial ice sheets and therefore far away from the first threshold. This agrees at least qualitatively with the finding that the location of the cooling threshold in Oka's simulations depended on the wind-stress forcing.

4. *Which processes drive abrupt AMOC transitions in MPI-ESM?*

In the simulation with preindustrial ice sheets and a pCO_2 of 206 ppm, the AMOC switches abruptly back and forth between the two unstable AMOC modes. These transitions can be explained by a feedback loop between the salt transport into the North Atlantic, deep convection in the Nordic Seas and the extent of the subpolar gyre.

During the weak AMOC phases, the salt transport into the deep-water formation sites in the North Atlantic is very weak and NADW formation occurs only sporadically. Salinity accumulates in the upper 1000 m of the tropical Atlantic, and the North Atlantic is capped by a strong halocline. This leads to the build-up of a strong salinity gradient between the tropical and subpolar Atlantic, which acts as a preconditioning for the renewed onset of continuous NADW formation in the North Atlantic. A strong peak of northward salt transport restarts the continuous formation of deep water in the North Atlantic and the Nordic Seas and triggers the transition from the weak to the strong AMOC phase. The Denmark Strait overflow strengthens and the density gradient across the subpolar gyre is reduced. As a consequence, the subpolar gyre contracts, which favours the northward salt transport additionally. During the strong AMOC phases, the tropical salinity reservoir decreases rapidly and the peak of northward salt transport last only for about 300 to 400 years. After the peak, deep convection in the Nordic Seas and the Denmark Strait overflow weaken. This leads to a rapid expansion of the subpolar gyre, which reduces the salt flux into the North Atlantic further and thus triggers the transition from the strong to the weak AMOC phase. The subpolar halocline re-establishes and the tropical salinity increases again.

The presented results highlight the processes which govern the glacial AMOC state: brine release and shelf convection in the Southern Ocean and the salt transport into the North Atlantic. Southern Ocean brine release is enhanced by low GHG concentrations, while the salt transport into the North Atlantic is enhanced by the glacial ice sheets. Thus, the glacial AMOC state is the result of two large opposing effects. The explicit simulation of small scale processes like brine release or shelf convection requires a very high-resolution ocean model. In relatively coarse-resolution climate models, these processes are often parameterised. The effect of low GHG concentrations on Southern Ocean brine release and shelf convection may depend on the parameterisation and thus differ from model to model. The northward salt transport depends strongly on the wind field over the North Atlantic. The glacial wind field in turn depends - among other factors - on the implementation of the glacial ice sheets in the respective models. As a consequence, the magnitude of the GHG effect and of the ice-sheet effect will be model dependent, and already small differences in the magnitude of either or both effects can result in a different sign of the total glacial AMOC response. This provides a good explanation for the inconsistent AMOC responses within the PMIP ensemble.

A | Freshwater budget of the North Atlantic

The northward salt transport in Fig. 6.6 is calculated from the freshwater budget of the Atlantic basin north of 30°N. The freshwater budget is defined as:

$$\frac{\partial}{\partial t} FC_{Atl} = FT_{Bering} + FT_{30N} + netP_{Atl}, \tag{A.1}$$

where FC_{Atl} is the freshwater content of the Atlantic north of 30°N, FT_{Bering} the sum of the solid and liquid freshwater transport through the Bering Strait, FT_{30N} the freshwater transport across 30°N and $netP_{Atl}$ the net precipitation (P-E+R) integrated over the Atlantic basin north of 30°N, including the Mediterranean Sea and the Arctic Ocean. The freshwater content and transports are calculated against a reference salinity of 35.07 g kg^{-1}, which is the spatio-temporal average of the salinity in the Atlantic north of 30°N in the pi206 simulation. The freshwater transport FT_{30N} is calculated as the residual from the change of the freshwater content FC_{Atl}, the freshwater transport through Bering Strait FT_{Bering} and the net precipitation $netP_{Atl}$. This way, FT_{30N} describes the sum of the diffusive and advective freshwater transport. The northward salt transport is then given by (-1)×FT_{30N}. The time series of the four components of the freshwater budget are shown in Fig. A.1.

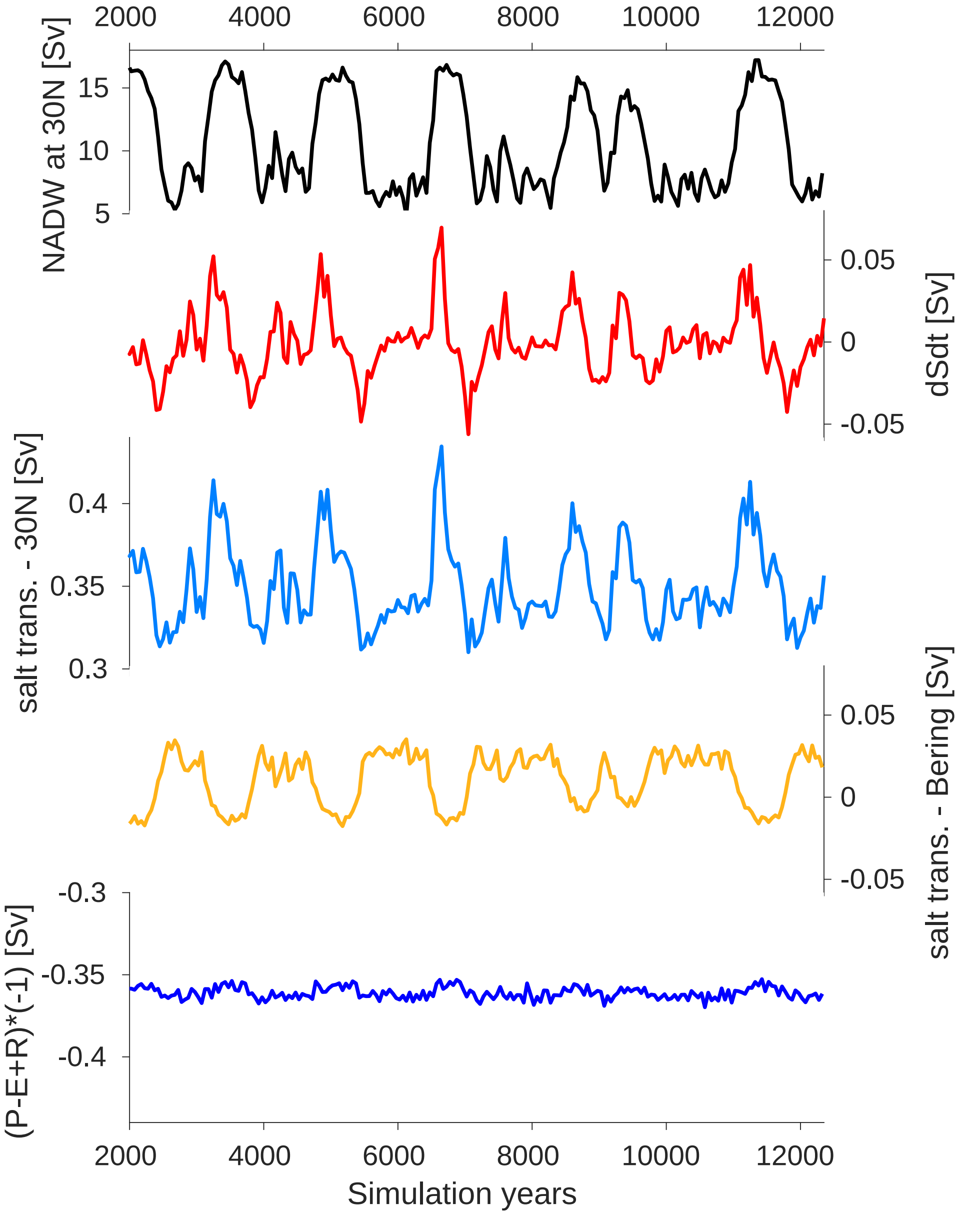

Figure A.1: NADW strength at 30°N (black) and the components of the freshwater budget of the Atlantic north of 30°N: time derivative of freshwater content (red), freshwater transport near 30°N (light blue), freshwater transport (solid + liquid) through Bering Strait (orange), net precipitation (P-E+R) integrated over the Atlantic basin north of 30°N including the Arctic Ocean (dark blue). All quantities are multiplied by (-1) to indicate the salt content and salt transport, respectively. Positive values imply an increase of the salt content and a northward salt transport, respectively.

B | Supplementary figures to Ch.7

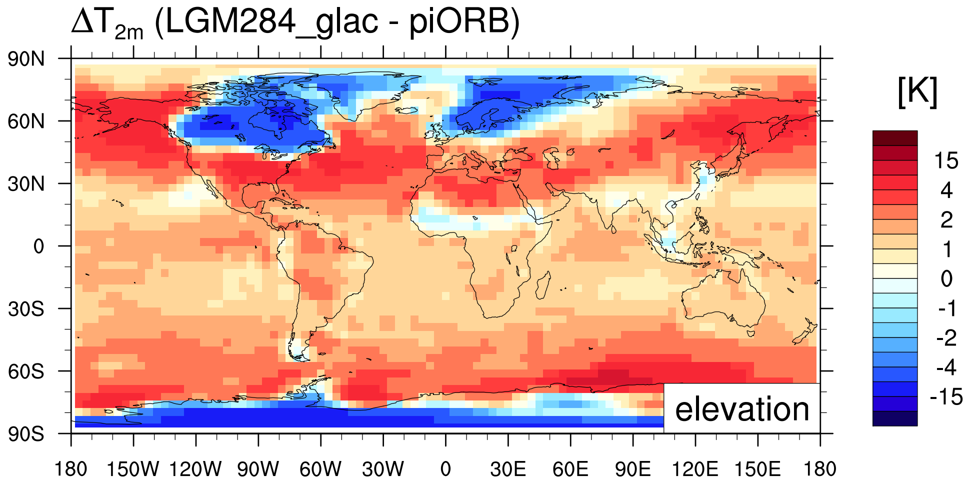

Figure B.1: The difference in 2 m air temperature induced by the LGM ice-sheet elevation (LGM284_glac – piORB).

(a) τ (piORB) (b) τ (LGMref)

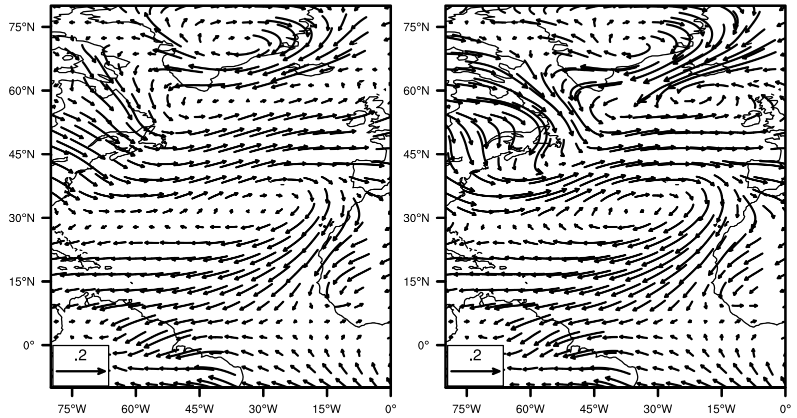

(c) dτ (LGM284 - piORB) (d) dτ (LGMref - LGM284)

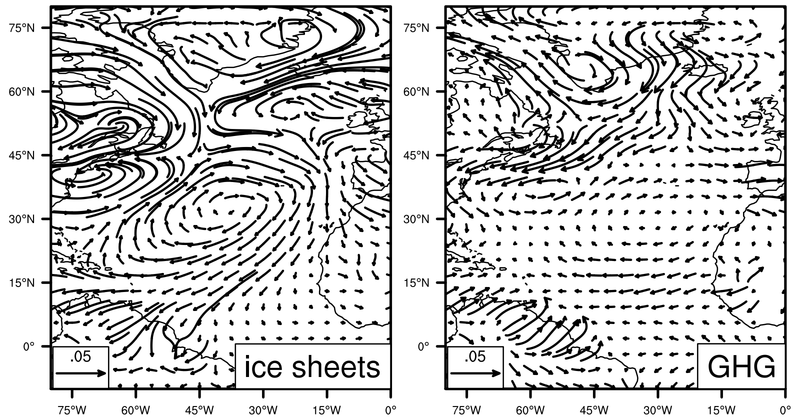

(e) dτ (LGM284 - LGM248_glac) (f) dτ (LGM284_glac - piORB)

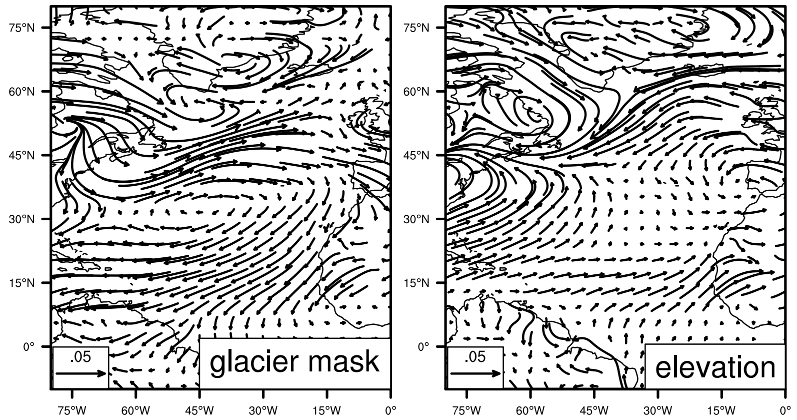

Figure B.2: Surface wind stress in **(a)** piORB and **(b)** LGM284, as well as changes in surface winds stress due to **(c)** the glacial ice sheets, **(d)** the glacial GHG concentrations and **(e)** the LGM glacier mask and **(f)** the elevation of the glacial ice sheets.

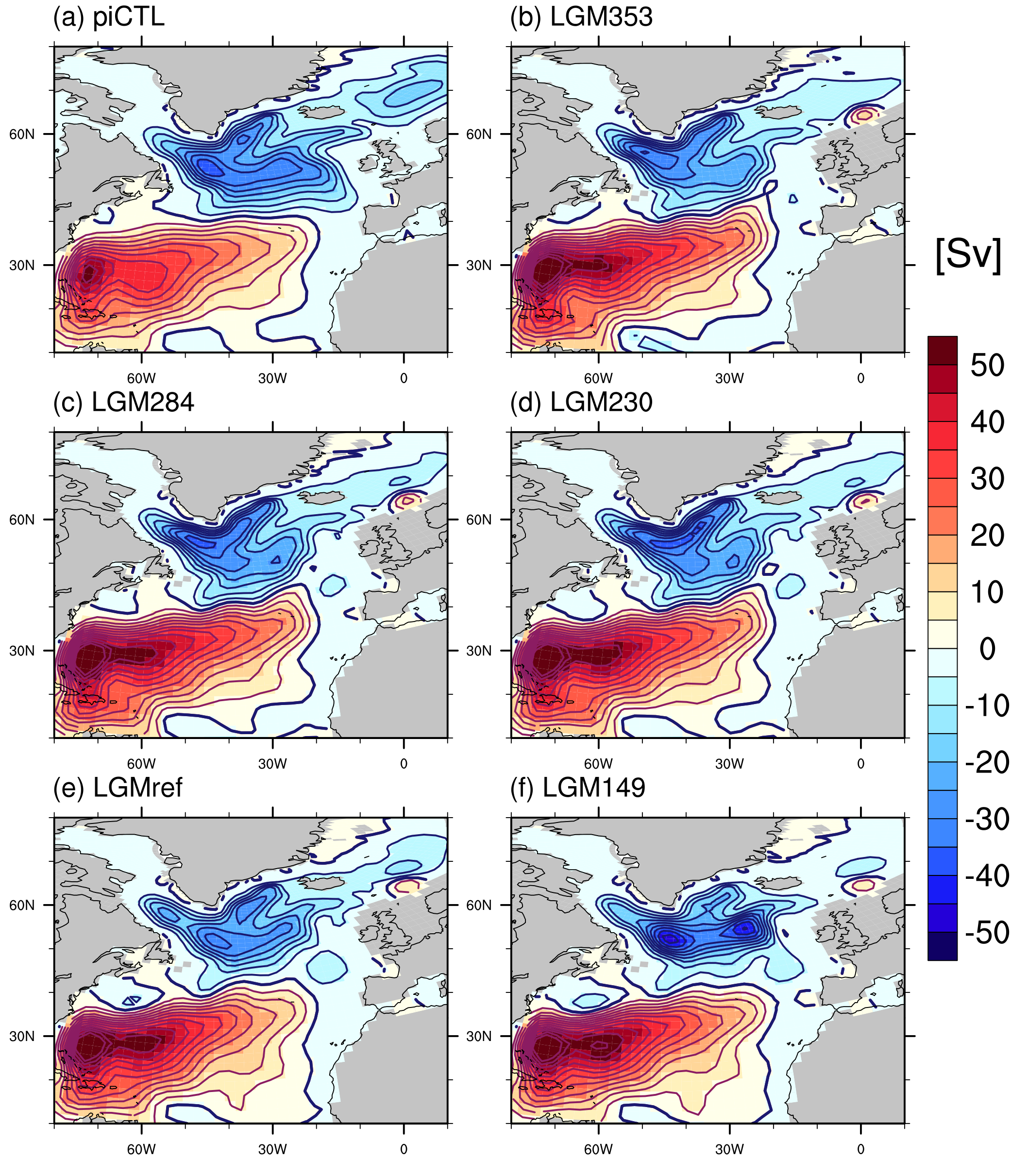

Figure B.3: Barotropic stream function in piCTL and the LGM*xxx* simulations. The contour interval is 5 Sv.

C | List of acronyms

AABW	Antarctic Bottom Water
AMOC	Atlantic Meridional Overturning Circulation
CMIP	Coupled Model Intercomparison Project
ΔRF	difference in radiative forcing
DO	Dansgaard-Oeschger
ECHAM	European Center HAMburg model
EMIC	Earth system Model of Intermediate Complexity
GHG	greenhouse gas
JSBACH	Jena Scheme of Atmosphere Biosphere Coupling in Hamburg
LGM	Last Glacial Maximum
LGM*xxx*	simulation series with glacial ice sheets, glacial orbit and different pCO_2 (see Tab. 2.2)
MARGO	Multiproxy Approach for the Reconstruction of the Glacial Ocean surface
MLD	mixed layer depth
MPI-ESM	Max Planck Institute Earth System Model
MPIOM	Max Planck Institute Ocean Model
NADW	North Atlantic Deep Water
εNd	ratio of neodymium isotopes (^{143}Nd/^{144}Nd)
OOC	open-ocean convection
OOC$_{min}$	Open-ocean convection area where the mixed layer depth in all considered simulations exceeds a certain depth

OOC_{max}	Open-ocean convection area where the mixed layer depth in any of the considered simulation exceeds a certain depth
Pa/Th	ratio of protactinium and thorium isotopes (^{231}Pa/^{230}Th)
pi*xxx*	simulation series with preindustrial ice sheets, glacial orbit and different pCO_2 (see Tab. 2.2)
PMIP	Paleoclimate Modelling Intercomparison Project
PV14	short for *Peltier and Vettoretti* (2014)
SPG	subpolar gyre
STG	subtropical gyre
SST	sea surface temperature
SSS	sea surface salinity

Bibliography

Abe-Ouchi, A., F. Saito, M. Kageyama, P. Braconnot, S. Harrison, K. Lambeck, B. Otto-Bliesner, W. Peltier, L. Tarasov, J.-Y. Peterschmitt, and K. Takahashi, Ice-sheet configuration in the CMIP5/PMIP3 Last Glacial Maximum experiments., *Geoscientific Model Development*, *8*(11), 3621–3637, doi:10.5194/gmd-8-3621-2015, 2015.

Adkins, J. F., The role of deep ocean circulation in setting glacial climates, *Paleoceanography*, *28*(3), 539–561, doi:10.1002/palo.20046, 2013.

Adkins, J. F., K. McIntyre, and D. P. Schrag, The Salinity, Temperature, and δ18O of the Glacial Deep Ocean, *Science*, *298*(5599), 1769–1773, doi:10.1126/science.1076252, 2002.

Annan, J., and J. Hargreaves, A new global reconstruction of temperature changes at the Last Glacial Maximum, *Climate of the Past*, *9*(1), 367–376, doi:10.5194/cp-9-367-2013, 2013.

Argus, D. F., W. Peltier, R. Drummond, and A. W. Moore, The Antarctica component of postglacial rebound model ICE-6G_C (VM5a) based on GPS positioning, exposure age dating of ice thicknesses, and relative sea level histories, *Geophysical Journal International*, *198*(1), 537–563, doi:10.1093/gji/ggu140, 2014.

Arzel, O., M. H. England, A. C. de Verdiere, and T. Huck, Abrupt millennial variability and interdecadal-interstadial oscillations in a global coupled model: sensitivity to the background climate state, *Climate Dynamics*, *39*(1-2), 259–275, doi:10.1007/s00382-011-1117-y, 2012.

Bakker, P., A. Schmittner, J. Lenaerts, A. Abe-Ouchi, D. Bi, M. Broeke, W.-L. Chan, A. Hu, R. Beadling, S. Marsland, S. Mernhild, O. Saenko, D. Swingedouw, A. Sullivan, and J. Yin, Fate of the atlantic meridional overturning circulation: Strong decline under continued warming and greenland melting, *Geophysical Research Letters*, *43*(23), doi:10.1002/2016GL070457, 2016.

Bartlein, P., S. Harrison, S. Brewer, S. Connor, B. Davis, K. Gajewski, J. Guiot, T. Harrison-Prentice, A. Henderson, O. Peyron, I. Prentice, M. Scholze, H. Seppä, B. Shuman, S. Sugita, R. Thompson, A. Viau, J. Williams, and H. Wu, Pollen-based continental climate reconstructions at 6 and 21 ka: a global synthesis, *Climate Dynamics*, *37*(3-4), 775–802, doi:10.1007/s00382-010-0904-1, 2011.

Böhm, E., J. Lippold, M. Gutjahr, M. Frank, P. Blaser, B. Antz, J. Fohlmeister, N. Frank, M. Andersen, and M. Deininger, Strong and deep Atlantic meridional overturning circulation during the last glacial cycle, *Nature*, *517*(7532), 73–76, doi:10.1038/nature14059, 2015.

Born, A., and T. F. Stocker, Two stable equilibria of the Atlantic Subpolar Gyre, *Journal of Physical Oceanography*, *44*(1), 246–264, doi:10.1175/JPO-D-13-073.1, 2014.

Born, A., T. F. Stocker, C. C. Raible, and A. Levermann, Is the Atlantic subpolar gyre bistable in comprehensive coupled climate models?, *Climate dynamics*, *40*(11-12), 2993–3007, doi:10.1007/s00382-012-1525-7, 2013.

Braconnot, P., and M. Kageyama, Shortwave forcing and feedbacks in Last Glacial Maximum and Mid-Holocene PMIP3 simulations, *Philosophical Transactions of the Royal Society A*, *373*(2054), 20140,424, doi:10.1098/rsta.2014.0424, 2015.

Braconnot, P., B. Otto-Bliesner, S. Harrison, S. Joussaume, J.-Y. Peterchmitt, A. Abe-Ouchi, M. Crucifix, E. Driesschaert, T. Fichefet, C. Hewitt, M. Kageyama, A. Kitoh, A. Laine, M.-F. Loutre, O. Marti, U. Merkel, G. Ramstein, P. Valdes, S. Weber, Y. Yu, and Y. Zhao, Results of PMIP2 coupled simulations of the Mid-Holocene and Last Glacial Maximum–Part 1: experiments and large-scale features, *Climate of the Past*, *3*(2), 261–277, doi:10.5194/cp-3-261-2007, 2007.

Braconnot, P., S. Harrison, B. Otto-Bliesner, A. Abe-Ouchi, J. Jungclaus, and J. Peterschmitt, The Paleoclimate Modeling Intercomparison Project contribution to CMIP5, *CLIVAR Exchanges No.56*, *16*(2), 15–19, 2011.

Brady, E. C., B. L. Otto-Bliesner, J. E. Kay, and N. Rosenbloom, Sensitivity to Glacial Forcing in the CCSM4, *Journal of Climate*, *26*(6), 1901–1925, doi:10.1175/JCLI-D-11-00416.1, 2013.

Broccoli, A., and S. Manabe, The influence of continental ice, atmospheric CO_2, and land albedo on the climate of the last glacial maximum, *Climate Dynamics*, *1*(2), 87–99, doi:10.1007/BF01054478, 1987.

Broecker, W. S., D. M. Peteet, and D. Rind, Does the ocean-atmosphere system have more than one stable mode of operation?, *Nature*, *315*(6014), 21–26, doi:10.1038/315021a0, 1985.

Brown, N., and E. D. Galbraith, Hosed vs. unhosed: interruptions of the Atlantic Meridional Overturning Circulation in a global coupled model, with and without freshwater forcing, *Climate of the Past*, *12*(8), 1663–1679, doi:10.5194/cp-12-1663-2016, 2016.

Burke, A., O. Marchal, L. I. Bradtmiller, J. F. McManus, and R. François, Application of an inverse method to interpret ^{231}Pa/^{230}Th observations from marine sediments, *Paleoceanography*, *26*(1), doi:10.1029/2010PA002022, 2011.

Cessi, P., A simple box model of stochastically forced thermohaline flow, *Journal of Physical Oceanography*, *24*(9), 1911–1920, doi:10.1175/1520-0485(1994)024<1911:ASBMOS>2.0.CO;2, 1994.

Chavaillaz, Y., F. Codron, and M. Kageyama, Southern westerlies in LGM and future (RCP4. 5) climates, *Climate of the Past*, *9*(2), 517–524, doi:10.5194/cp-9-517-2013, 2013.

Colin de Verdière, A., A simple model of millennial oscillations of the thermohaline circulation, *Journal of Physical Oceanography*, *37*(5), 1142–1155, doi:10.1175/JPO3056.1, 2007.

Copard, K., C. Colin, G. Henderson, J. Scholten, E. Douville, M.-A. Sicre, and N. Frank, Late holocene intermediate water variability in the northeastern atlantic as recorded by deep-sea corals, *Earth and Planetary Science Letters*, *313*, 34–44, doi:10.1016/j.epsl.2011.09.047, 2012.

Crucifix, M., P. Braconnot, S. Harrison, and B. Otto-Bliesner, Second phase of Paleoclimate Modelling Intercomparison Project, *EOS, Transactions American Geophysical Union*, *86*(28), 264–264, doi:10.1029/2005EO280003, 2005.

Curry, W. B., and D. W. Oppo, Glacial water mass geometry and the distribution of $\delta 13C$ of ΣCO_2 in the western Atlantic Ocean, *Paleoceanography*, *20*(1), doi:10.1029/2004PA001021, 2005.

Dansgaard, W., S. Johnsen, H. Clausen, D. Dahl-Jensen, N. Gundestrup, C. Hammer, and H. Oeschger, North Atlantic climatic oscillations revealed by deep Greenland ice cores, *Climate processes and climate sensitivity*, pp. 288–298, doi:10.1029/GM029p0288, 1984.

Dokken, T. M., K. H. Nisancioglu, C. Li, D. S. Battisti, and C. Kissel, Dansgaard-oeschger cycles: Interactions between ocean and sea ice intrinsic to the Nordic Seas, *Paleoceanography*, *28*(3), 491–502, doi:10.1002/palo.20042, 2013.

Duplessy, J., N. Shackleton, R. Fairbanks, L. Labeyrie, D. Oppo, and N. Kallel, Deepwater source variations during the last climatic cycle and their impact on the global deepwater circulation, *Paleoceanography*, *3*(3), 343–360, doi:10.1029/PA003i003p00343, 1988.

Felzer, B., T. Webb III, and R. J. Oglesby, The impact of ice sheets, CO_2, and orbital insolation on late Quaternary climates: sensitivity experiments with a general circulation model, *Quaternary Science Reviews*, *17*(6), 507–534, doi:10.1016/S0277-3791(98)00010-9, 1998.

Ferrari, R., M. F. Jansen, J. F. Adkins, A. Burke, A. L. Stewart, and A. F. Thompson, Antarctic sea ice control on ocean circulation in present and glacial climates, *Proceedings of the National Academy of Sciences*, *111*(24), 8753–8758, doi:10.1073/pnas.1323922111, 2014.

Frajka-Williams, E., S. Cunningham, H. Bryden, and B. King, Variability of Antarctic Bottom Water at 24.5 N in the Atlantic, *Journal of Geophysical Research: Oceans (1978–2012)*, *116*(C11), doi:10.1029/2011JC007168, 2011.

Friedrich, T., A. Timmermann, L. Menviel, O. Elison Timm, A. Mouchet, and D. Roche, The mechanism behind internally generated centennial-to-millennial scale climate variability in an earth system model of intermediate complexity, *Geoscientific Model Development*, *3*(2), 377–389, doi:10.5194/gmd-3-377-2010, 2010.

Ganopolski, A., and S. Rahmstorf, Rapid changes of glacial climate simulated in a coupled climate model, *Nature*, *409*(6817), 153–158, doi:10.1038/35051500, 2001.

Ganopolski, A., and S. Rahmstorf, Abrupt glacial climate changes due to stochastic resonance, *Physical Review Letters*, *88*(3), 038,501, doi:10.1103/PhysRevLett.88.038501, 2002.

Gebbie, G., How much did glacial North Atlantic water shoal?, *Paleoceanography*, *29*(3), 190–209, doi:10.1002/2013PA002557, 2014.

Giorgetta, M. A., J. Jungclaus, C. Reick, S. Legutke, J. Bader, M. Böttinger, V. Brovkin, T. Crueger, M. Esch, K. Fieg, K. Glushak, V. Gayler, H. Haak, H.-D. Hollweg, T. Ilyina, S. Kinne, L. Kornblueh, D. Matei, T. Mauritsen, U. Mikolajewicz, W. Mueller, D. Notz, F. Pithan, T. Raddatz, S. Rast, R. Redler, E. Roeckner, H. Schmidt, R. Schnur, J. Segschneider, K. Six, M. Stockhause, C. Timmreck, J. Wegner, H. Widmann, K. Wieners, M. Claussen, J. Marotzke, and B. Stevens, Climate and carbon cycle changes from 1850 to 2100 in MPI-ESM simulations for the Coupled Model Intercomparison Project phase 5, *Journal of Advances in Modeling Earth Systems*, *5*(3), 572–597, doi:10.1002/jame.20038, 2013.

Grootes, P., M. Stuiver, J. White, S. Johnsen, and J. Jouzel, Comparison of oxygen isotope records from the gisp2 and grip greenland ice cores, *Nature*, *366*(6455), 552–554, doi:10.1038/366552a0, 1993.

Hargreaves, J. C., J. D. Annan, R. Ohgaito, A. Paul, and A. Abe-Ouchi, Skill and reliability of climate model ensembles at the Last Glacial Maximum and mid-Holocene, *Climate of the Past*, *9*(2), 811–823, doi:10.5194/cp-9-811-2013, 2013.

Harrison, S., P. Bartlein, K. Izumi, G. Li, J. Annan, J. Hargreaves, P. Braconnot, and M. Kageyama, Evaluation of CMIP5 palaeo-simulations to improve climate projections, *Nature Climate Change*, *5*(8), 735–743, doi:10.1038/nclimate2649, 2015.

Hátún, H., A. B. Sandø, H. Drange, B. Hansen, and H. Valdimarsson, Influence of the Atlantic subpolar gyre on the thermohaline circulation, *Science*, *309*(5742), 1841–1844, doi:10.1126/science.1114777, 2005.

Heinrich, H., Origin and consequences of cyclic ice rafting in the northeast Atlantic Ocean during the past 130,000 years, *Quaternary Research*, *29*(2), 142–152, doi:10.1016/0033-5894(88)90057-9, 1988.

Hewitt, C., and J. Mitchell, Radiative forcing and response of a GCM to ice age boundary conditions: cloud feedback and climate sensitivity, *Climate Dynamics*, *13*(11), 821–834, doi:10.1007/s003820050199, 1997.

Jungclaus, J., N. Keenlyside, M. Botzet, H. Haak, J.-J. Luo, M. Latif, J. Marotzke, U. Mikolajewicz, and E. Roeckner, Ocean Circulation and Tropical Variability in the Coupled Model ECHAM5/MPI-OM, *Journal of Climate*, *19*(16), 3952–3972, doi:10.1175/JCLI3827.1, 2006.

Jungclaus, J., N. Fischer, H. Haak, K. Lohmann, J. Marotzke, D. Matei, U. Mikolajewicz, D. Notz, and J. Storch, Characteristics of the ocean simulations in the Max Planck Institute Ocean Model (MPIOM) the ocean component of the MPI-Earth system model, *Journal of Advances in Modeling Earth Systems*, *5*(2), 422–446, doi:10.1002/jame.20023, 2013.

Justino, F., A. Timmermann, U. Merkel, and E. P. Souza, Synoptic Reorganization of Atmospheric flow during the Last Glacial Maximum, *Journal of Climate*, *18*(15), 2826–2846, doi:10.1175/JCLI3403.1, 2005.

Kageyama, M., P. Braconnot, S. Harrison, M. Haywood, J. Jungclaus, B. Otto-Bliesner, J.-Y. Peterschmitt, A. Abe-Ouchi, S. Albani, P. Bartlein, C. Brierley, M. Crucifix, A. Dolan, L. Fernandez-Donado, H. Fischer, P. Hopcroft, R. Ivanovic, F. Lambert, D. Lunt, N. Mahowald, W. Peltier, S. Phipps, D. Roche, G. Schmidt, L. Tarasov, P. Valdes, Q. Zhang, , and T. Zhou, PMIP4-CMIP6: the contribution of the Paleoclimate Modelling Intercomparison Project to CMIP6, *Geoscience Model Development Discussions*, doi:10.5194/gmd-2016-106, 2016, in review.

Kim, S.-J., The effect of atmospheric CO_2 and ice sheet topography on LGM climate, *Climate Dynamics*, *22*(6-7), 639–651, doi:10.1007/s00382-004-0412-2, 2004.

Kleinen, T., H. Held, and G. Petschel-Held, The potential role of spectral properties in detecting thresholds in the Earth system: application to the thermohaline circulation, *Ocean Dynamics*, *53*(2), 53–63, doi:10.1007/s10236-002-0023-6, 2003.

Kleppin, H., M. Jochum, B. Otto-Bliesner, C. A. Shields, and S. Yeager, Stochastic atmospheric forcing as a cause of Greenland climate transitions, *Journal of Climate*, *28*(19), 7741–7763, doi:10.1175/JCLI-D-14-00728.1, 2015.

Klockmann, M., U. Mikolajewicz, and J. Marotzke, The effect of greenhouse gas concentrations and ice sheets on the glacial AMOC in a coupled climate model, *Climate of the Past*, *12*(9), 1829–1846, doi:10.5194/cp-12-1829-2016, 2016.

Knutti, R., and T. F. Stocker, Limited predictability of the future thermohaline circulation close to an instability threshold, *Journal of Climate*, *15*(2), 179–186, doi:10.1175/1520-0442(2002)015<0179:LPOTFT>2.0.CO;2, 2002.

Kurahashi-Nakamura, T., A. Paul, and M. Losch, Dynamical reconstruction of the global ocean state during the last glacial maximum, *Paleoceanography*, *32*, doi:10.1002/2016PA003001, 2017.

Lambeck, K., A. Purcell, J. Zhao, and N.-O. Svensson, The Scandinavian ice sheet: from MIS 4 to the end of the Last Glacial Maximum, *Boreas*, *39*(2), 410–435, doi:10.1111/j.1502-3885.2010.00140.x, 2010.

Levermann, A., and A. Born, Bistability of the Atlantic subpolar gyre in a coarse-resolution climate model, *Geophysical Research Letters*, *34*(24), doi:10.1029/2007GL031732, 2007.

Li, C., J.-S. von Storch, and J. Marotzke, Deep-ocean heat uptake and equilibrium climate response, *Climate Dynamics*, *40*(5-6), 1071–1086, doi:10.1007/s00382-012-1350-z, 2013.

Lippold, J., Y. Luo, R. Francois, S. E. Allen, J. Gherardi, S. Pichat, B. Hickey, and H. Schulz, Strength and geometry of the glacial Atlantic Meridional Overturning Circulation, *Nature Geoscience*, *5*(11), 813–816, doi:10.1038/ngeo1608, 2012.

Lippold, J., M. Gutjahr, P. Blaser, E. Christner, M. de Carvalho Ferreira, S. Mulitza, M. Christl, F. Wombacher, E. Böhm, B. Antz, O. Cartapanis, H. Vogel, and S. Jaccard, Deep water provenance and dynamics of the (de)glacial Atlantic meridional overturning circulation, *Earth and Planetary Science Letters*, *445*, 68–78, doi:10.1016/j.epsl.2016.04.013, 2016.

Lynch-Stieglitz, J., J. Adkins, W. Curry, T. Dokken, I. Hall, J. Herguera, J.-M. Hirschi, E. Ivanova, C. Kissel, O. Marchal, T. Marchitto, I. McCave, J. McManus, S. Mulitza, U. Ninnemann, F. Peeters, E. Yu, and R. Zahn, Atlantic meridional overturning circulation during the Last Glacial Maximum, *Science*, *316*(5821), 66–69, doi:10.1126/science.1137127, 2007.

Manabe, S., and R. Stouffer, Two stable equilibria of a coupled ocean-atmosphere model, *Journal of Climate*, *1*(9), 841–866, doi:10.1175/1520-0442(1988)001<0841:TSEOAC>2.0.CO;2, 1988.

Manabe, S., and R. J. Stouffer, Multiple-century response of a coupled ocean-atmosphere model to an increase of atmospheric carbon dioxide, *Journal of Climate*, *7*(1), 5–23, doi:10.1175/1520-0442(1994)007<0005:MCROAC>2.0.CO;2, 1994.

MARGO Project Members, Constraints on the magnitude and patterns of ocean cooling at the Last Glacial Maximum, *Nature Geoscience*, *2*(2), 127–132, doi:10.1038/ngeo411, 2009.

Marotzke, J., Climate science: A grip on ice-age ocean circulation, *Nature*, *485*(7397), 180–181, doi:10.1038/485180a, 2012.

Marsland, S. J., H. Haak, J. H. Jungclaus, M. Latif, and F. Röske, The Max-Planck-Institute global ocean/sea ice model with orthogonal curvilinear coordinates, *Ocean Modelling*, *5*(2), 91–127, doi:10.1016/S1463-5003(02)00015-X, 2003.

McCarthy, G., D. Smeed, W. Johns, E. Frajka-Williams, B. Moat, D. Rayner, M. Baringer, C. Meinen, J. Collins, and H. Bryden, Measuring the Atlantic Meridional Overturning Circulation at 26° N, *Progress in Oceanography*, *130*, 91–111, doi:10.1016/j.pocean.2014.10.006, 2015.

McDougall, T. J., and P. M. Barker, Getting started with TEOS-10 and the Gibbs Seawater (GSW) oceanographic toolbox, *SCOR/IAPSO WG*, *127*, 1–28, 2011.

McManus, J., R. Francois, J.-M. Gherardi, L. Keigwin, and S. Brown-Leger, Collapse and rapid resumption of Atlantic meridional circulation linked to deglacial climate changes, *Nature*, *428*(6985), 834–837, doi:10.1038/nature02494, 2004.

Mikolajewicz, U., Modeling Mediterranean Ocean climate of the Last Glacial Maximum, *Climate of the Past*, *7*(1), 161–180, doi:10.5194/cp-7-161-2011, 2011.

Mikolajewicz, U., and E. Maier-Reimer, Mixed boundary conditions in ocean general circulation models and their influence on the stability of the model's conveyor belt, *Journal of Geophysical Research: Oceans (1978–2012)*, *99*(C11), 22,633–22,644, doi:10.1029/94JC01989, 1994.

Miller, M., J. Adkins, D. Menemenlis, and M. Schodlok, The role of ocean cooling in setting glacial southern source bottom water salinity, *Paleoceanography*, *27*(3), doi:10.1029/2012PA002297, 2012.

Montoya, M., A. Born, and A. Levermann, Reversed North Atlantic gyre dynamics in present and glacial climates, *Climate Dynamics*, *36*(5-6), 1107–1118, doi:10.1007/s00382-009-0729-y, 2011.

Moreno-Chamarro, E., D. Zanchettin, K. Lohmann, and J. H. Jungclaus, An abrupt weakening of the subpolar gyre as trigger of Little Ice Age-type episodes, *Climate Dynamics*, pp. 1–18, doi:10.1007/s00382-016-3106-7, 2016.

Msadek, R., W. E. Johns, S. G. Yeager, G. Danabasoglu, T. L. Delworth, and A. Rosati, The Atlantic meridional heat transport at 26.5 N and its relationship with the

MOC in the RAPID array and the GFDL and NCAR coupled models, *Journal of Climate*, *26*(12), 4335–4356, doi:10.1175/JCLI-D-12-00081.1, 2013.

Muglia, J., and A. Schmittner, Glacial Atlantic overturning increased by wind stress in climate models, *Geophysical Research Letters*, *42*, doi:10.1002/2015GL064583, 2015.

Myhre, G., E. J. Highwood, K. P. Shine, and F. Stordal, New estimates of radiative forcing due to well mixed greenhouse gases, *Geophysical Research Letters*, *25*(14), 2715–2718, doi:10.1029/98GL01908, 1998.

Notz, D., F. A. Haumann, H. Haak, J. H. Jungclaus, and J. Marotzke, Arctic sea-ice evolution as modeled by Max Planck Institute for Meteorology's Earth system model, *Journal of Advances in Modeling Earth Systems*, *5*(2), 173–194, doi:10.1002/jame.20016, 2013.

Oka, A., H. Hasumi, and A. Abe-Ouchi, The thermal threshold of the Atlantic meridional overturning circulation and its control by wind stress forcing during glacial climate, *Geophysical Research Letters*, *39*(9), doi:10.1029/2012GL051421, 2012.

Otto-Bliesner, B., C. Hewitt, T. Marchitto, E. Brady, A. Abe-Ouchi, M. Crucifix, S. Murakami, and S. Weber, Last Glacial Maximum ocean thermohaline circulation: PMIP2 model intercomparisons and data constraints, *Geophysical Research Letters*, *34*(12), doi:10.1029/2007GL029475, 2007.

Otto-Bliesner, B., R. Schneider, E. Brady, M. Kucera, A. Abe-Ouchi, E. Bard, P. Braconnot, M. Crucifix, C. Hewitt, M. Kageyama, O. Marti, A. Paul, A. Rosell-Mele, C. Waelbroeck, S. Weber, M. Weinelt, and Y. Yu, A comparison of PMIP2 model simulations and the MARGO proxy reconstruction for tropical sea surface temperatures at last glacial maximum, *Climate Dynamics*, *32*(6), 799–815, doi:10.1007/s00382-008-0509-0, 2009.

Otto-Bliesner, B. L., E. C. Brady, G. Clauzet, R. Tomas, S. Levis, and Z. Kothavala, Last Glacial Maximum and Holocene climate in CCSM3, *Journal of Climate*, *19*(11), 2526–2544, doi:10.1175/JCLI3748.1, 2006.

Pausata, F., C. Li, J. Wettstein, M. Kageyama, and K. Nisancioglu, The key role of topography in altering North Atlantic atmospheric circulation during the last glacial period, *Climate of the Past*, *7*(4), 1089–1101, doi:10.5194/cp-7-1089-2011, 2011.

Peltier, W., Global glacial isostasy and the surface of the ice-age Earth: the ICE-5G (VM2) model and GRACE, *Annual Review of Earth and Planetary Sciences*, *32*, 111–149, doi:10.1146/annurev.earth.32.082503.144359, 2004.

Peltier, W., D. Argus, and R. Drummond, Space geodesy constrains ice age terminal deglaciation: The global ICE-6G_C (VM5a) model, *Journal of Geophysical Research: Solid Earth*, *120*(1), 450–487, doi:10.1002/2014JB011176, 2015.

Peltier, W. R., and G. Vettoretti, Dansgaard-Oeschger oscillations predicted in a comprehensive model of glacial climate: A kicked salt oscillator in the Atlantic, *Geophysical Research Letters*, *41*(20), 7306–7313, doi:10.1002/2014GL061413, 2014.

Rahmstorf, S., M. Crucifix, A. Ganopolski, H. Goosse, I. Kamenkovich, R. Knutti, G. Lohmann, R. Marsh, L. A. Mysak, Z. Wang, and A. J. Weaver, Thermohaline circulation hysteresis: A model intercomparison, *Geophysical Research Letters*, *32*(23), doi:10.1029/2005GL02365, 2005.

Reick, C., T. Raddatz, V. Brovkin, and V. Gayler, Representation of natural and anthropogenic land cover change in MPI-ESM, *Journal of Advances in Modeling Earth Systems*, *5*(3), 459–482, doi:10.1002/jame.20022, 2013.

Rugenstein, M. A., J. Sedláček, and R. Knutti, Nonlinearities in patterns of long-term ocean warming, *Geophysical Research Letters*, *43*(7), 3380–3388, doi:10.1002/2016GL068041, 2016.

Schmidt, M. W., M. J. Vautravers, and H. J. Spero, Rapid subtropical North Atlantic salinity oscillations across Dansgaard–Oeschger cycles, *Nature*, *443*(7111), 561–564, doi:10.1038/nature05121, 2006.

Schmittner, A., N. M. Urban, J. D. Shakun, N. M. Mahowald, P. U. Clark, P. J. Bartlein, A. C. Mix, and A. Rosell-Melé, Climate sensitivity estimated from temperature reconstructions of the Last Glacial Maximum, *Science*, *334*(6061), 1385–1388, doi:10.1126/science.1203513, 2011.

Shakun, J. D., P. U. Clark, F. He, S. A. Marcott, A. C. Mix, Z. Liu, B. Otto-Bliesner, A. Schmittner, and E. Bard, Global warming preceded by increasing carbon dioxide concentrations during the last deglaciation, *Nature*, *484*(7392), 49–54, doi:10.1038/nature10915, 2012.

Shin, S.-I., Z. Liu, B. Otto-Bliesner, E. Brady, J. Kutzbach, and S. Harrison, A simulation of the Last Glacial Maximum climate using the NCAR-CCSM, *Climate Dynamics*, *20*(2-3), 127–151, doi:10.1007/s00382-002-0260-x, 2003.

Stevens, B., M. Giorgetta, M. Esch, T. Mauritsen, T. Crueger, S. Rast, M. Salzmann, H. Schmidt, J. Bader, K. Block, R. Brokopf, I. Fast, S. Kinne, L. Kornblueh, U. Lohmann, R. Pincus, T. Reichler, and E. Roeckner, Atmospheric component of the MPI-M Earth System Model: ECHAM6, *Journal of Advances in Modeling Earth Systems*, *5*(2), 146–172, doi:10.1002/jame.20015, 2013.

Stommel, H., Thermohaline convection with two stable regimes of flow, *Tellus*, *13*(2), 224–230, doi:10.3402/tellusa.v13i2.9491, 1961.

Stössel, A., D. Notz, F. A. Haumann, H. Haak, J. Jungclaus, and U. Mikolajewicz, Controlling high-latitude Southern Ocean convection in climate models, *Ocean Modelling*, *86*, 58–75, doi:10.1016/j.ocemod.2014.11.008, 2015.

Stouffer, R., and S. Manabe, Equilibrium response of thermohaline circulation to large changes in atmospheric CO_2 concentration, *Climate Dynamics*, *20*(7-8), 759–773, doi:10.1007/s00382-002-0302-4, 2003.

Tarasov, L., A. S. Dyke, R. M. Neal, and W. Peltier, A data-calibrated distribution of deglacial chronologies for the North American ice complex from glaciological modeling, *Earth and Planetary Science Letters*, *315*, 30–40, doi:10.1016/j.epsl.2011.09.010, 2012.

Thornalley, D. J., H. Elderfield, and I. N. McCave, Holocene oscillations in temperature and salinity of the surface subpolar North Atlantic, *Nature*, *457*(7230), 711–714, doi:10.1038/nature07717, 2009.

Tziperman, E., Proximity of the present-day thermohaline circulation to an instability threshold, *Journal of Physical Oceanography*, *30*(1), 90–104, doi:10.1175/1520-0485(2000)030<0090:POTPDT>2.0.CO;2, 2000.

Valcke, S., The OASIS3 coupler: a European climate modelling community software, *Geoscientific Model Development*, *6*(2), 373–388, doi:10.5194/gmd-6-373-2013, 2013.

Vellinga, M., and R. A. Wood, Global climatic impacts of a collapse of the atlantic thermohaline circulation, *Climatic Change*, *54*(3), 251–267, doi:10.1023/A:1016168827653, 2002.

Voss, R., and U. Mikolajewicz, The climate of 6000 years BP in near-equilibrium simulations with a coupled AOGCM, *Geophysical Research Letters*, *28*(11), 2213–2216, doi:10.1029/2000GL012498, 2001a.

Voss, R., and U. Mikolajewicz, Long-term climate changes due to increased CO_2 concentration in the coupled atmosphere-ocean general circulation model ECHAM3/LSG, *Climate Dynamics*, *17*(1), 45–60, doi:10.1007/PL00007925, 2001b.

Wang, Z., and L. A. Mysak, lacial abrupt climate changes and Dansgaard-Oeschger oscillations in a coupled climate model, *Paleoceanography*, *21*(2), doi:10.1029/2005PA001238, 2006.

Wang, Z., L. A. Mysak, and J. F. McManus, Response of the thermohaline circulation to cold climates, *Paleoceanography*, *17*(1), doi:10.1029/2000PA000587, 2002.

Weaver, A. J., J. Sedláček, M. Eby, K. Alexander, E. Crespin, T. Fichefet, G. Philippon-Berthier, F. Joos, M. Kawamiya, K. Matsumoto, M. Steinacher, K. Tachiiri, K. Tokos, M. Yoshimori, and K. Zickfeld, Stability of the atlantic meridional overturning circulation: A model intercomparison, *Geophysical Research Letters*, *39*(20), doi:10.1029/2012GL053763, 2012.

Weber, S., S. Drijfhout, A. Abe-Ouchi, M. Crucifix, M. Eby, A. Ganopolski, S. Murakami, B. Otto-Bliesner, and W. Peltier, The modern and glacial overturning circulation in the Atlantic ocean in PMIP coupled model simulations, *Climate of the Past*, *3*(1), 51–64, doi:10.5194/cp-3-51-2007, 2007.

Welander, P., Thermohaline effects in the ocean circulation and related simple models, in *Large-scale transport processes in oceans and atmosphere*, pp. 163–200, Springer, doi:10.1007/978-94-009-4768-9_4, 1986.

Winguth, A., D. Archer, J.-C. Duplessy, E. Maier-Reimer, and U. Mikolajewicz, Sensitivity of paleonutrient tracer distributions and deep-sea circulation to glacial boundary conditions, *Paleoceanography*, *14*(3), 304–323, doi:10.1029/1999PA900002, 1999.

Yu, E.-F., R. Francois, and M. P. Bacon, Similar rates of modern and last-glacial ocean thermohaline circulation inferred from radiochemical data, *Nature*, *379*(6567), 689, doi:10.1038/379689a0, 1996.

Zhang, R., T. L. Delworth, A. Rosati, W. G. Anderson, K. W. Dixon, H.-C. Lee, and F. Zeng, Sensitivity of the north atlantic ocean circulation to an abrupt change in the nordic sea overflow in a high resolution global coupled climate model, *Journal of Geophysical Research: Oceans*, *116*(C12), doi:10.1029/2011JC007240, 2011.

Zhang, X., G. Lohmann, G. Knorr, and C. Purcell, Abrupt glacial climate shifts controlled by ice sheet changes, *Nature*, *512*, 290–294, doi:10.1038/nature13592, 2014.

Zhu, J., Z. Liu, X. Zhang, I. Eisenman, and W. Liu, Linear weakening of the AMOC in response to receding glacial ice sheets in CCSM3, *Geophysical Research Letters*, *41*(17), 6252–6258, doi:10.1002/2014GL060891, 2014.

Zhu, J., Z. Liu, J. Zhang, and W. Liu, Amoc response to global warming: dependence on the background climate and response timescale, *Climate Dynamics*, *44*(11-12), 3449–3468, doi:10.1007/s00382-014-2165-x, 2015.

Ziemen, F., C. Rodehacke, and U. Mikolajewicz, Coupled ice sheet–climate modeling under glacial and pre-industrial boundary conditions, *Climate of the Past*, *10*, 1817–1836, doi:10.5194/cp-10-1817-2014, 2014.

Acknowledgements

Technical

My research was supported by the International Max Planck Research School on Earth System Modelling. The simulations for this thesis were performed on the supercomputers Blizzard and Mistral at the German Climate Computing Centre (DKRZ). Thanks to Helmuth Haak and Kalle Wieners for helping me to get started with MPI-ESM. I used Matlab, NCL and CDO for most of the analysis of the model output. Thanks to Laura Niederdrenk for providing me with a FORTRAN script to calculate the sea-ice divergence, which went into the calculation of the surface density fluxes. For the analysis of the water-mass properties in Fig.4.4, Fig.4.6 and Fig.5.4 I used the Matlab toolbox for the TEOS10 equation of state (*McDougall and Barker*, 2011, www.teos-10.org/software.htm). All figures in Ch.2 to 7 were produced with NCL or Matlab. The MARGO SST reconstructions used in Fig.3.2 were published by the *MARGO Project Members* (2009) and are available for download at https://doi.pangaea.de/10.1594/PANGAEA.733406. The temperature reconstructions over land were published by *Bartlein et al.* (2011). They are available in the online supporting material of the original publication (doi:10.1007/s00382-010-0904-1). Additional land points were taken from a compilation by *Shakun et al.* (2012). I obtained the data from the online supporting material of *Schmittner et al.* (2011), which can be downloaded at http://people.oregonstate.edu/~schmita2/data/schmittner11sci/LGM_deltaT_synthesis_Shakun_etal_2011.xlsx.

Personal

I want to thank Uwe Mikolajewicz for his supervision, support, continuous interest and the very thorough scrutiny of my results. I have learned a great deal more about both the virtual ocean in MPIOM and about the real ocean over the last years. I also want to thank Jochem Marotzke for his support and for introducing me to the art of scientific writing. And thank you to Johanna Baehr for becoming my second supervisor in the last year of my PhD. Our discussions about the progress and structure of my thesis were very helpful to me. I would also like to thank Hartmut Graßl, the chair of my advisory panel, for the very effective and precise panel meetings.

Many thanks go to all present and former members of the Ocean Physics group. I enjoyed being part of this group (and will continue to enjoy it for a while longer). I want to especially thank Flo for many discussions (scientific and not), Kartoffelpuffer and survival-chocolate. And Laura for countless coffee breaks, teaching me the secrets of NCL and knitting patterns and for always having an open door for me!

Laura also introduced me to the world-renowned experts on climate change Rauser, Sonntag, Juliane, Vera and Freja, with whom I participated in so many performances of the *Weltklimakonferenz* while being in the middle of my PhD (some people say, I have been in the middle of my PhD for quite some time). Thank you also to the Rimini Protokoll for making this possible and to all other fellow participants. I enjoyed this experience a lot!

Many thanks go to Antje, Connie and Wiebke of the IMPRS office for their support in all kinds of matters. And to all fellow IMPRS students, I enjoyed being part of this group! I want to especially mention Hanna, my great office mate. I am happy that we will continue to share our office for a while longer! And Raphaela, who started her PhD at the same day as me. You are a great travel companion, I hope we will travel to more places together! And Chris, who shared many responsibilities with me. It was an honour to be IMPRS-PhD representative and a member of the Fachpromotionsausschuss with you!

Before finishing my thanks to people at the MPI-M, I want to especially thank Christine Nam, Florian Ziemen and Sebstian Sonntag for reading and checking large parts of this thesis. Outside of MPI-M, but still in the world of science, I want to thank Roberto Sabia and Diego Fernandez from the European Space Agency. Learning about water-mass formation with you proved very helpful over the last years! And I would also like to thank Detlef Stammer from the University of Hamburg and Niklas Schneider from the University of Hawaii for supporting my application to the IMPRS-ESM!

Then I would like to mention Meike, Franzi and Hannah, with whom I did my Bachelor and Master at the University of Hamburg! And Janina and Maria, who did not study with me, but whom I have known for a very long time and they need to be in here, too! It is great to share a city and a life with all of you! It goes without saying that the same is true for my family. It is great to have you so close! And of course it is most true for Luca! Thanks for being there, for cheering me up, for encouraging me and for getting up every morning to have coffee with me.

Publications derived from this thesis

Klockmann, M., Mikolajewicz, U. and Marotzke, J.: *The effect of greenhouse gas concentrations and ice sheets on the glacial AMOC in a coupled climate model*, Climate of the Past, 12, 1829-1846, doi:10.5194/cp-12-1829-2016, 2016

Eidesstattliche Erklärung / *Declaration of oath*

Hiermit erkläre ich an Eides statt, dass ich die vorliegende Dissertationsschrift selbst verfasst und keine anderen als die angegeben Quellen und Hilfsmittel benutzt habe.

I hereby declare, on oath, that I have written the present dissertation myself and that I have not used any other than the acknowledged resources and aids.

Hamburg, 02.05.2017

Marlene Klockmann